

X-ray Absorption Fine Structure Debye-Waller Factors.

by

Anna V. Poiarkova

A dissertation submitted in partial fulfillment
of the requirements for the degree of

Doctor of Philosophy

University of Washington

1999

Approved by _____
(Chairperson of Supervisory Committee)

Program Authorized
to Offer Degree _____

Date _____

In presenting this dissertation in partial fulfillment of the requirements for the Doctoral degree at the University of Washington, I agree that the Library shall make its copies freely available for inspection. I further agree that extensive copying of this dissertation is allowable only for scholarly purposes, consistent with "fair use" as prescribed in the U.S. Copyright Law. Requests for copying or reproduction of this dissertation may be referred to University Microfilms, 1490 Eisenhower Place, P.O. Box 975, Ann Arbor, MI 48106, to whom the author has granted "the right to reproduce and sell (a) copies of the manuscript in microform and/or (b) printed copies of the manuscript made from microform."

Signature_____

Date_____

University of Washington

Abstract

X-ray Absorption Fine Structure Debye-Waller Factors.

by Anna V. Poiarkova

Chairperson of Supervisory Committee: Professor John J. Rehr

Department of Physics

For accurate x-ray absorption fine structure (XAFS) spectra calculations, especially in complex and disordered systems, it is crucial to have an efficient and reliable method for obtaining multiple-scattering XAFS Debye-Waller factors. Traditional phenomenological models such as the correlated Debye and Einstein models, often fail to provide sufficient accuracy in the mean square half-path length fluctuation, σ^2 . To overcome limitations of such isotropic models we introduce two alternative methods for the Debye-Waller factor calculations: the equation-of-motion method and the recursion method. These are generalized for a multiple-scattering case from their original single-scattering formulation.

The equation-of-motion method is an efficient local method for calculation of the mean fluctuations σ_j^2 in XAFS Debye-Waller factors for a general scattering path j . Given a few local force constants, the method yields σ_j^2 via the projected densities of modes or via the displacement-displacement correlation function in real time, over a few vibration cycles. Sample applications of the method are presented for crystalline Cu and Ge, and for several organometallic molecules. XAFS Debye-Waller factors in anion of tetrachloroferrate (II) were calculated via the equation-of-motion method using dynamical matrix obtained from *ab initio* computation via density

functional theory by means of the DGauss program. These *ab initio* Debye-Waller factors were then used in XAFS calculations in tetramethylammonium tetrachloroferate (II). Debye-Waller factors were also calculated for single- and multiple scattering paths in a molecule of oxidized *Pyrococcus furious* rubredoxin and a molecule of zinc tetraimidazole based on force constants fitted to experimental vibrational spectra.

Also, efficient local recursion method is presented for σ_j^2 calculations. Instead of computing entire projected densities of modes, the calculations are based on a double δ -function representation. Sample application of the method is presented for Cu crystal. Both methods have been implemented as FORTRAN 77 FEFF compatible computer programs SIGEM and SIGRM. Discussion on calculation of anharmonic and spherical wave corrections is presented.

TABLE OF CONTENTS

List of Figures	iv
List of Tables	ix
Chapter 1: Introduction	1
1.1 Overview of the problem	1
1.2 Goals	4
1.3 Dissertation overview	5
1.4 Multiple scattering XAFS Debye-Waller factors	6
1.4.1 Formalism	6
1.4.2 Correlated Debye model	9
1.4.3 Correlated Einstein model	10
Chapter 2: Equation-of-motion method	12
2.1 Formalism	12
2.2 Multiple scattering σ_j^2	15
2.3 Force field models	16
2.4 How to find the right FF model	18
2.4.1 Fit to experiment	20
2.4.2 <i>Ab initio</i> calculations	22
2.4.3 FF parameterization and semiempirical methods	24
2.5 Applications	28
2.5.1 Cu	28

2.5.2	Ge	34
2.5.3	Zn-tetraimidazole	36
2.5.4	Semiempirical dynamical matrix calculation	45
Chapter 3:	Recursion method	48
3.1	Formalism	48
3.2	Calculations and results in Cu	50
Chapter 4:	XANES and XAFS calculations in organometallic systems	53
4.1	<i>Ab initio</i> calculation of the DW factors in tetrachloroferrate (II) . . .	53
4.1.1	Force constant matrix for an XY_4 molecule	53
4.1.2	Geometry optimization, VDOS and σ^2	56
4.2	XANES and XAFS analysis of tetramethylammonium tetrachloroferrate (II)	62
4.3	XANES and XAFS analysis of <i>Pyrococcus Furious</i> Rubredoxin . . .	67
Chapter 5:	Anharmonic and spherical wave corrections	75
5.1	Cumulant expansion	75
5.2	Spherical wave corrections	77
Chapter 6:	Conclusions	79
	Bibliography	83
Appendix A:	Computer programs sigem and sigrm	92
A.1	Program structure	92
A.2	Input file <code>spring.inp</code>	94
A.3	Output files	98

A.4	Local variables, their dimensions, and descriptions	99
A.5	Example input and output files	100
Appendix B:	Table of selected parameters used in the UFF model	105

LIST OF FIGURES

1.1	Schematic overview of the problem.	3
1.2	Projected VDOS $\rho_R(\omega)$ for the first shell of Cu calculated using the EM method with $N = 459$ and $k_1 = 27.9$ N/m (solid), in comparison with the CD (long dashes) and CE (short dashes) models.	11
2.1	Example of the displacement-displacement autocorrelation function with a cutoff term, $F(\tau) \equiv \langle Q_1(\tau) Q_1(0)\rangle e^{-\varepsilon\tau^2}$, for the first shell in Cu at 300 K vs a dimensionless time parameter $\tau = t/t_0$. Fourier transform of this function defines projected VDOS (see Eq. 2.6). . .	14
2.2	Mean square amplitudes σ_j^2 for a 459-atom cluster of Cu vs temperature as calculated from a single force constant ($k_1 = 27.9$ N/m) model for the first shell (EM SS) and for the 111 triangular MS path (EM 111). The CD model ($\theta_D = 315$ K) calculations for the first shell (CD SS) and the 111 triangular MS path (CD 111) and the CE model for the first shell (CE SS) are given for comparison. Points represent experimental values of σ^2 [1,2].	29
2.3	a) Projected VDOS $\rho_j(\omega)$ for the first shell (solid) and for the 111 triangular MS path (dashes) for Cu calculated via the EM method. b) Total VDOS $\rho(\omega)$ and projected VDOS $\rho_R(\omega)$ for the first shell and sixth shells of Cu calculated via the EM method.	30

2.4	Radial dependence of the correlation function C_R calculated for Cu at different temperatures using FEFF code and CD model with $\theta_D = 315$ K. Points correspond to different coordination shells.	31
2.5	Magnitude of the phase corrected Fourier transform $\tilde{\chi}(R) = \text{FT}[k\chi(k)]$ for Cu at $T = 150$ K as extracted from experiment using the phase corrected FEFFIT code (solid line), and fitted using theoretical results with the DW factors calculated via the CD (long dashes) and single force constant EM (short dashes) models.	33
2.6	VDOS for a 633-atom cluster of Ge as calculated via the EM method: a) for the first shell, b) for 121 triangular MS path c) total experimental spectrum determined from neutron scattering [3] in comparison with theoretical total VDOS $\rho(\omega)$	35
2.7	XAFS MS σ^2 for 147-atom cluster of Ge as calculated with the EM and CD models at $T = 300$ K vs MS path index (see text). Two experimental values [2], corresponding to the first and second shell SS, are given for comparison.	36
2.8	Magnitude of the phase corrected Fourier transform $\tilde{\chi}(R) = \text{FT}[k\chi(k)]$ for Ge at $T = 300$ K as extracted from experiment using the phase-corrected FEFFIT code (solid line) and fitted using theoretical results with the DW factors calculated via the CD (long dashes) and EM (short dashes) models.	37
2.9	Structure of the 37-atom zinc tetraimidazole macromolecule based on the coordinates given by LPT [4].	38
2.10	Reduced structural models used to approximate the VFF of zinc tetraimidazole with a) two and b) four effective force constants, as well as c) the 23-parameter VFF.	42

2.11	Low frequency part of the first shell projected VDOS $\rho_R(\omega)$ for the 23-parameter model of Zn-tetraimidazole ($N = 21$). The lines at 296, 277, 274, 228, 206, 205, 204, 184 and 174 cm^{-1} indicate low frequency tetrahedral modes obtained by LPT [4] for the entire 37-atom macromolecule.	44
3.1	MS XAFS σ_j^2 for Cu at 295 K as calculated with a single force constant ($k = 27.9 \text{ N/m}$) with RM, RM corrected with the 9/8 factor (RMc), EM and CE methods vs MS path index. Two experimental values [2] corresponding to the first and second shell SS are given for comparison.	52
4.1	Projected VDOS for three distinct triangular MS (a) and SS (b) paths in FeCl_4^- . The lines at 45.68, 78.23, 100.64, 109.89, 116.57, 245.34, 248.39, 281.77, and 284.02 cm^{-1} indicate the infrared vibrational modes calculated by DGauss.	59
4.2	Projected VDOS for two SS paths, $\text{Fe}_1 \rightarrow \text{Cl}_4$ and $\text{Fe}_1 \rightarrow \text{Cl}_5$, and two MS paths, $\text{Fe}_1 \rightarrow \text{Cl}_2 \rightarrow \text{Cl}_3$ and $\text{Fe}_1 \rightarrow \text{Cl}_2 \rightarrow \text{Cl}_4$, calculated using the EM method and the 10-parameter VFF model.	61
4.3	Structure of the 39-atom molecule of tetramethylammonium TCF (II), $[\text{N}(\text{CH}_3)_4]_2[\text{FeCl}_4]$, based on the coordinates given by Lauher and Ibers [5].	63
4.4	K-edge XANES spectra $\mu(E)$ and the corresponding backgrounds $\mu_0(E)$ for tetramethylammonium TCF (II) calculated with FEFF8X (solid) in comparison with experimental data (dashes).	65
4.5	K-edge XAFS $\chi(k)$ for tetramethylammonium TCF (II) calculated with FEFF8X (solid) in comparison with experimental data (dashes).	65

4.6	s-DOS for the central Fe ⁺² atom in tetramethylammonium TCF (II) as calculated with FEFF8X (solid line) in comparison with s-DOS calculated by UniChem (dashes).	66
4.7	p-DOS for the central Fe ⁺² atom (solid line) and $\chi(k)$ (long dashes) for tetramethylammonium TCF (II) as calculated with FEFF8X in comparison with p-DOS calculated by UniChem (short dashes).	66
4.8	d-DOS for the central Fe ⁺² atom in tetramethylammonium TCF (II) as calculated with FEFF8X (solid line) in comparison with d-DOS calculated by UniChem (dashes).	67
4.9	Magnitude of the phase corrected Fourier transform $\tilde{\chi}(R) = \text{FT}[k^2\chi(k)]$ for the first shell in tetramethylammonium TCF (II) at T = 300 K as extracted from the experiment (solid line), and as fitted using FEFF8X theoretical results with DW factors calculated via the EM method (dashes).	68
4.10	Atomic structure of a molecule of oxidized <i>Pyrococcus Furious</i> Rubredoxin.	69
4.11	Fe K-edge XANES spectra for oxidized (Fe ⁺³) rubredoxin calculated with FEFF8X in comparison with experimental data.	70
4.12	Fe K-edge XANES spectra for reduced (Fe ⁺²) rubredoxin calculated with FEFF8X in comparison with experimental data.	70
4.13	Comparison of XANES spectra $\mu(E)$ calculated with FEFF8X and experimental data for both forms of rubredoxin.	71
4.14	p-DOS for the central Fe atom and χ in both forms of rubredoxin.	71

4.15	Magnitude of the phase corrected Fourier transform $\tilde{\chi}(R) = \text{FT}[k^2\chi(k)]$ for oxidized rubredoxin at $T = 10$ K as extracted from the experiment (solid line), and fitted using FEFF8X theoretical results with DW factors calculated via the EM method (dashes).	74
A.1	A sample <code>feff.inp</code> file for use in a FEFF 8X run with EM option for DW factor calculation.	93
A.2	Implementation scheme.	94
A.3	A sample <code>spring.inp</code> file for 13-atom model of zinc tetraimidazole. The corresponding <code>feff.inp</code> is shown in Fig. A.1.	95
A.4	Sample <code>spring.inp</code> file for Cu crystal.	101
A.5	Sample output files for Cu crystal at 300 K: a) <code>s2_rm1.dat</code> , b) <code>s2_rm2.dat</code> , and c) <code>s2_em.dat</code>	102
A.6	Sample <code>spring.inp</code> file for Ge crystal.	103
A.7	Sample output files for Ge crystal at 300 K: a) <code>s2_rm1.dat</code> , b) <code>s2_rm2.dat</code> , and c) <code>s2_em.dat</code>	104

LIST OF TABLES

2.1	Values of the parameters in Badger's model for diatomic molecules. Here C_{ij} is in such units that k_R is in N/m.	26
2.2	Values of first shell SS σ_1^2 and MS σ_3^2 for 111 triangular MS path as calculated using EM method in comparison with CD model ($\theta_D = 315$ K) and experimental values [6].	32
2.3	Force constants used in our VFF models 1–2 for σ_j^2 calculation in zinc tetraimidazole. Here \tilde{N} and \tilde{C} are pseudo-atoms (see text). All angle bends are scaled by corresponding near-neighbor distances.	39
2.4	Force constants used in the VFF 3 for σ_j^2 calculation in zinc tetraimidazole. All angle bends are scaled by corresponding near-neighbor distances.	40
2.5	Values of MS σ_j^2 at 20 K calculated for four central MS paths of the type $\text{Zn} \xrightarrow{k^{(1)}} \text{N}^{(1)} \xrightarrow{\theta} \text{N}^{(2)} \xrightarrow{k^{(2)}} \text{Zn}$ in zinc tetraimidazole depending on the number of the force constants (ν) used in the VFF model. Here j is the MS path index, R_j its effective length, φ_j the scattering angle $\text{N}^{(1)} - \text{Zn} - \text{N}^{(2)}$ in degrees, $k^{(i)}$ the force constant for the bond $\text{Zn} - \text{N}^{(i)}$ and θ is the bending force constant for the corresponding φ_j . All force constants are given in N/m.	43
2.6	Values of SS σ_1^2 at 20 K for the weak Zn–N bond in zinc tetraimidazole depending on the number of the force constants (ν) used in the VFF model. Here $\epsilon_{exp} = 100(\sigma_1^2 - \sigma_{exp}^2)/\sigma_{exp}^2$ and $\epsilon = 100(\sigma_1^2 - \sigma_{LPT}^2)/\sigma_{LPT}^2$ with $\sigma_{exp}^2 = (2.5 \pm 0.2) \times 10^{-3} \text{ \AA}^2$ and $\sigma_{LPT}^2 = 2.62 \times 10^{-3} \text{ \AA}^2$	43

2.7	Values of selected bonds and angles in zinc tetraimidazole obtained from AM1 geometry optimization in comparison with experimental values given by Loeffen <i>et al.</i> [4]. All bonds are in units of Å, angles are in degrees.	46
2.8	Values of MS σ_j^2 (10^{-3} Å ²) at 20 K and 300 K calculated for several MS paths in zinc tetraimidazole based on AM1 dynamical matrix in comparison with values obtained by Loeffen <i>et al.</i> [4].	47
3.1	Values of MS $\sigma_j^2 \times 10^{-3}$ Å ² at 295 K for a 225-atom cluster of Cu as calculated with a single force constant ($k = 27.9$ N/m) model using RM (σ_{RM}^2) and CE (σ_{CE}^2) approximation vs MS path index j . Two experimental values [2] corresponding to the first and second shell SS are given for comparison. Also, given are Einstein frequencies ω_E , effective frequencies $\omega_{1,2}$ (all in THz), and the corresponding weight factors $w_{1,2}$ (dimensionless).	51
4.1	Matrix B for an XY_4 molecule.	55
4.2	Definitions and values of the internal coordinates S_t used in the study: the bond lengths (Å) and the bond angles (deg). The values are given for the LDA and GGA optimized structures.	57
4.3	Bond distances and angles in FeCl_4^{2-} anion found in different studies and different compounds (see [5] for references).	58
4.4	Matrix elements of Φ_{int} in units of ($10^2 \times \text{mdyn}\text{Å} / [S_{t_1}] / [S_{t_2}]$) where $[S_{t_i}]$ is in Å for bonds and in rad for angles.	60

4.5	SS and MS σ_j^2 for selected paths calculated via the EM method at two temperatures using the entire force constant matrix Φ in comparison with calculations based on the 10-parameter VFF model. Here scattering path indices j are equal to the corresponding internal coordinate indices t	62
4.6	Force constants used for σ_j^2 calculation in oxidized rubredoxin. Bond stretching force constants are in units of mdyn/Å and bond bending are in mdynÅ/rad ²	72
4.7	SS and MS σ_j^2 for selected paths calculated via the EM method at two temperatures 10 and 300 K.	73
5.1	Third cumulants for the first nearest neighbor in Cu calculated using thermal expansion coefficient α [7] for different temperatures T	77
B.1	Values of selected UFF model parameters for different atoms.	105

ACKNOWLEDGMENTS

There are many people whom I would like to thank for their assistance in conducting this research and for helping me to go cheerfully through the 4 1/2 roller-coaster years of graduate school. Unfortunately, I am not able to thank individually every one of them here but I sincerely do so in my heart. I am especially indebted to my thesis advisor John J. Rehr for being a great mentor, for his strong guidance and support, his valuable lessons, and for giving me an opportunity to work on such an interesting project. I am also very grateful to Edward A. Stern for his guidance, help, and encouragement, to Lowell S. Brown for being a great teacher and his very helpful criticism of the early draft of this dissertation, to Keith Hodgson, Britt Hedman and Graham George (SSRL) for providing much needed experimental data and the research grant (NIH RR 01209), to Alexei Ankoudinov for his invaluable assistance and for setting a remarkable example in work and research. I would like to express my gratitude to Hannes Jonsson, Dani Haskel, Bruce Ravel, Luke Campbell, and Matt Newville for very valuable discussions and assistance, and to Greg Schenter and David A. Dixon for their enormous help with the DGauss calculations. And most of all, I would like to thank my dearest husband Randall, my parents, and all other members of my deeply beloved family for their endless support, care, understanding, and all precious things they have taught me in life.

Chapter 1

INTRODUCTION

Make everything as simple as possible, but not simpler.

Albert Einstein, (1879–1955)

1.1 Overview of the problem

In the context of temperature dependence of XAFS spectra, the theory of the single-scattering (SS) XAFS Debye-Waller (DW) factors and their relation to the molecular force field (FF) was first introduced by Beni and Platzman [8] in 1976. Today, more than 20 years later, XAFS DW theory is still lacking general *ab initio* formulation and application of the XAFS analysis to study vibrational properties of solids has been hardly explored [9]. In recent years XAFS analysis has become an important and widely used technique for determining local microscopic structure of complex and disordered materials. The structural information it provides includes average near-neighbor distances R , their mean square fluctuations σ_R^2 , and coordination numbers N_R . The quantities σ_R^2 which appear in the XAFS DW factor are crucial to the success of the modern theory of XAFS and its applications. The DW factor accounts for thermal and structural disorder and generally governs the “melting” of the XAFS oscillations with respect to increasing temperature and their decay with respect to increasing photoelectron energy. In practice, the DW factors of the many multiple-scattering (MS) terms in the XAFS signal can significantly complicate the analysis [10–12]. In an attempt to overcome these difficulties we developed two general methods for calculating the DW factors in terms of a few local force constants in

arbitrary aperiodic systems: the equation-of-motion (EM) method [13, 14] and the recursion method (RM) [15]. These methods also provide a basis for fitting parameters of molecular FF models directly to XAFS spectra.

Before presenting detailed mathematical formalism, it is useful to give a qualitative description of the origin of the XAFS DW factors first. Absorption of an x-ray photon by an atom induces excitation of a single deep core electron which then undergoes a series of scattering from the surrounding atoms before returning to the absorbing center. The course of scattering can involve either a single scattering site, i.e. the SS process, or several sites, the MS process. Due to thermal vibrations, \vec{u}_i , of the scattering and absorbing atoms, their positions become smeared out around the equilibrium sites. Mean square fluctuations, σ_j^2 , in the lengths of the photoelectron's scattering paths quantitatively account for this effect on the XAFS amplitude via an exponential factor, the DW factor.

The diagram in Fig. 1.1 summarizes the problem of the XAFS DW factor calculation presented in the following sections (for description of the symbols used in the diagram see Sec. 1.4.1). As mentioned above XAFS, $\chi(k)$, provides valuable structural information. Because of the relation between σ_j^2 and the projected vibrational density of states (VDOS) $\rho_j(\omega)$, the fluctuations σ_j^2 can be used to obtain information on interatomic interactions in the form of the local force constants, k_i . This dependence opens a possibility to fit the FF parameters directly to the experimental XAFS spectrum. This is the, so called, inverse problem. On the other hand, it is valuable to first solve the direct problem of calculating values of σ^2 based on a given dynamical model. A derivation of the formula expressing σ_j^2 via $\rho_j(\omega)$ and the projected reduced mass μ_j , as well as definitions of these new quantities, will be given in the next chapter. This dissertation is aimed at solving the direct problem but also outlines a solution for the inverse one.

Similarly to the XAFS DW factors, there are also DW factors which appear in the x-ray diffraction (XRD) and Mössbauer effect. Here the thermal vibrational

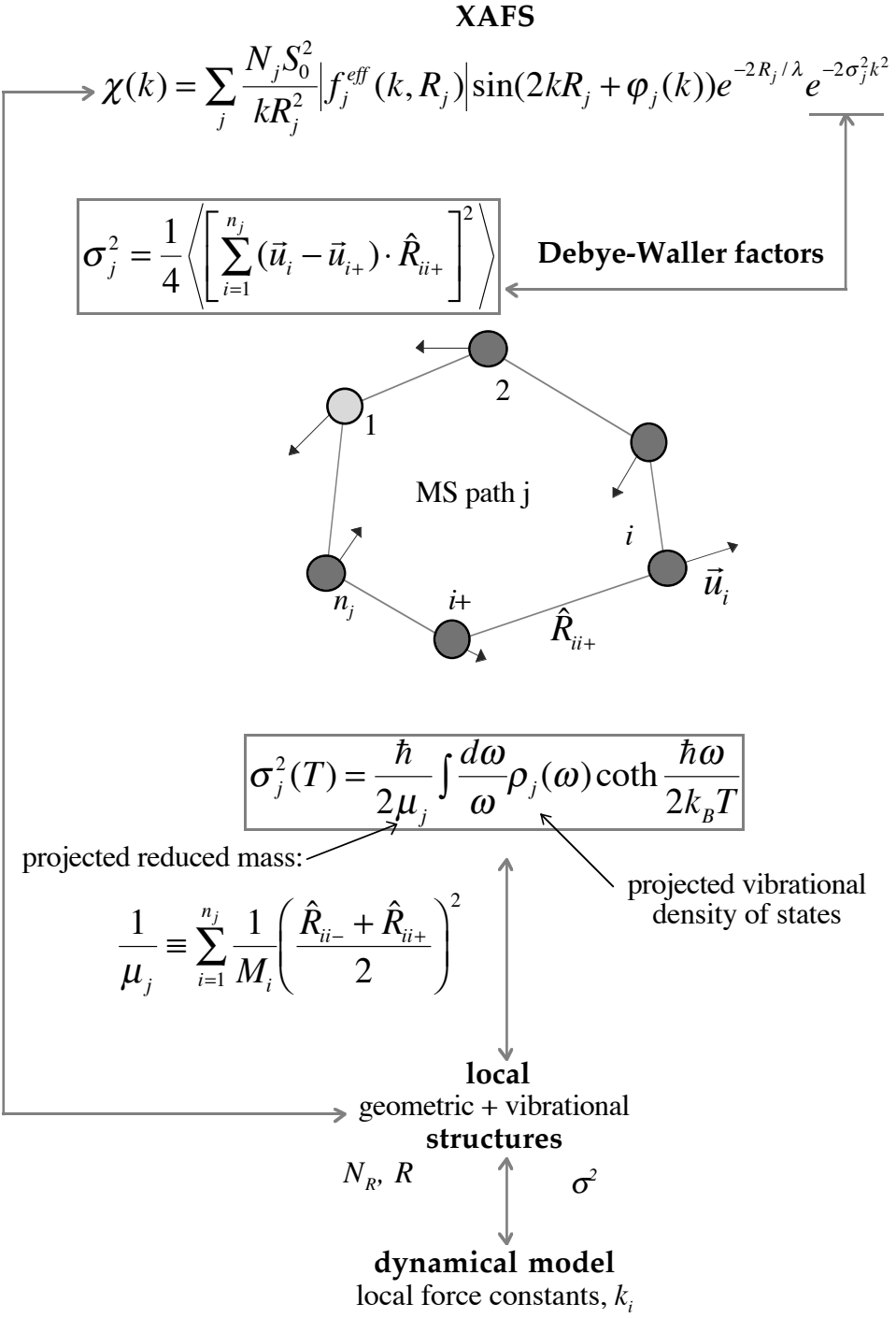


Figure 1.1: Schematic overview of the problem.

parameter analogous to σ_j^2 is the mean square vibration of an atom i in direction \hat{k} and is equal to $u_{i,k}^2 = \langle [\vec{u}_i \cdot \hat{k}]^2 \rangle$. It can be calculated using the same frequency domain formula as we derived for σ_j^2 but with projected VDOS replaced by total VDOS and μ_j with mass of the atom at the site i , M_i .

1.2 Goals

The primary goal of the conducted research and the dissertation was to develop, implement, and test general prescriptions for MS XAFS DW factor calculations. In order to achieve this goal the following work has been done:

- Generalization of the original SS EM method for MS case.
- Computer implementation of the EM method.
- Research and analysis of different FF models.
- Testing of the EM method and analysis of the calculated vibrational spectra for both crystalline and disordered materials using different FF models.
- Search for an *ab initio* code which would allow the calculation the FF parameters from first principles (DGAUSS is one answer for biological molecules).
- *Ab initio* calculation of the FF in biological systems.
- XANES and XAFS analysis in organometallic compounds.
- Generalization of the original SS RM for a MS case.
- Computer implementation and testing of the RM.
- Calculation of anharmonic corrections.

These goals have been successfully achieved, and the results are presented in the following chapters.

1.3 Dissertation overview

In the Introduction (Chap. 1) we provide a short summary of the formalism underlying the MS XAFS DW factor theory as well as a brief review of two popular isotropic models, the correlated Einstein (CE) and correlated Debye (CD) models, used for its calculation. Chapters 2 and 3 describe two alternative approaches to σ^2 calculations, the EM method and the RM, and their applications. The formalism in these chapters is self-contained, although additional background on different FF models might be useful.

Chapter 4 offers a prescription for *ab initio* MS DW factor calculations in organic systems on example of tetrachloroferrate (II). The results of this example *ab initio* calculation are then used in the XAFS analysis of tetramethylammonium tetrachloroferrate (II). Chapter 5 reviews some of the higher order corrections to XAFS DW factors. Descriptions of the EM (SIGEM) and RM (SIGRM) FORTRAN 77 computer programs which were developed and used in the present study are given in the Appendix. And, finally, the conclusions of the conducted research are presented in Chap. 6.

One might find helpful a list of abbreviations used in the dissertation:

- XAFS – x-ray absorption fine structure
- EXAFS – extended XAFS
- XANES – x-ray absorption near edge structure
- MS – multiple scattering
- SS – single scattering

- DW – Debye-Waller
- CD – correlated Debye
- CE – correlated Einstein
- EM – equation-of-motion
- RM – recursion method
- VDOS – vibrational density of states ($\rho(\omega)$)
- FF – force field
- VFF – valence force field
- UFF – Universal force field
- MM – molecular mechanics

1.4 Multiple scattering XAFS Debye-Waller factors

1.4.1 Formalism

In this work the DW factor $\exp(-W_j(k))$ for a given scattering path of total length $2r_j$ is defined by the thermal and configurational average of the oscillatory part of the XAFS signal

$$\langle e^{i2kr_j} \rangle = e^{i2kR_j} e^{-W_j(k)}, \quad (1.1)$$

where the index j corresponds to the j th scattering path. Curved wave effects on the DW factors are usually negligible and will be ignored here [16]. We also neglect anharmonic corrections. In the weak disorder limit (or harmonic approximation), this

DW factor is a Gaussian, $W_j(k) = 2k^2\sigma_j^2$, where $\sigma_j^2 = \langle (r_j - R_j)^2 \rangle$ is the mean square variation in the effective or half-path length $R_j = \langle r_j \rangle$ appearing in the standard XAFS equation,

$$\chi(k) = \sum_j \frac{N_j S_0^2}{k R_j^2} |f_j^{\text{eff}}(k, R_j)| \sin(2kR_j + \phi_j(k)) e^{-2R_j/\lambda} e^{-2\sigma_j^2 k^2}. \quad (1.2)$$

Here the sum runs over all unique scattering paths j (i.e. both single scattering (SS) and MS paths) of degeneracy N_j , $f_j^{\text{eff}}(k, R_j)$ is the effective curved-wave backscattering amplitude, S_0^2 is a many-body amplitude reduction factor, $\phi_j(k)$ is the net phase shift, $k = [2(E - E_F)]^{1/2}$ is the wave number measured from threshold E_F , and λ is the photoelectron mean free path.

To better understand the nature of MS DW factors it is useful to examine their origin. The XAFS spectrum χ is defined as the normalized, oscillatory part of the x-ray absorption coefficient μ , i.e., $\chi = (\mu - \mu_0)/\mu_0$, where μ_0 is the smooth atomic-background absorption. According to XAFS theory χ can be expressed as a thermal average [10]

$$\chi(k) = \text{Im} \left\langle \sum_j \frac{N_j S_0^2 f_j^{\text{eff}}(k, r_j)}{k r_j^2} e^{i(2kr_j + 2\delta_c) - 2r_j/\lambda} \right\rangle, \quad (1.3)$$

where δ_c is central atom phase shift and r_j is a dynamical variable equal to the instantaneous effective length of a scattering path j . The radial dependence of f_j^{eff} goes as $1/r_j$ and constitutes only a small correction to the amplitude [12]. Assuming small disorder and, since $1/r_j$ and $\exp(-2r_j/\lambda)/r_j^2$ vary more slowly with distance than $\exp(i2kr_j)$, neglecting curved wave effects from the r_j dependence of f_j^{eff} , $\exp(-2r_j/\lambda)$, and $1/r_j^2$ ¹ we have

¹ Radial dependence of $\exp(-2r_j/\lambda)/r_j^2$ leads to an additional phase shift equal to $-4k\sigma_j^2/R_j(1 + R_j/\lambda)$ which is linear in k and is significant only for systems with large disorder [12, 17].

$$\chi(k) = \text{Im} \sum_j \frac{N_j S_0^2 f_j^{\text{eff}}(k, R_j)}{k R_j^2} e^{i2\delta_c - 2R_j/\lambda} \langle e^{i2kr_j} \rangle, \quad (1.4)$$

where the thermal average is given by

$$\langle e^{i2kr_j} \rangle = \frac{\text{Tr} e^{-\beta H} e^{i2kr_j}}{\text{Tr} e^{-\beta H}}. \quad (1.5)$$

Here H is the lattice Hamiltonian and $\beta = 1/k_B T$. Now let \vec{u}_i be the displacement from equilibrium of the ion at site i , so that neglecting terms of order u_i^2 , the effective path length for a scattering path j with n_j scattering legs is

$$r_j \simeq R_j + \frac{1}{2} \sum_{i=1}^{n_j} (\vec{u}_i - \vec{u}_{i+}) \cdot \hat{R}_{ii+}. \quad (1.6)$$

Here $i+ \equiv i+1$, $i = n_j + 1$ corresponds to site $i = 1$, $R_j \equiv (1/2) \sum_i R_{ii+}$ is, as before, the effective equilibrium path length, R_{ii+} is the equilibrium interatomic distance between atoms i and $i+$, and \hat{R}_{ii+} is the corresponding directing unit vector. From the Born-Oppenheimer approximation, the ion motion can be regarded as stationary during a transition. Hence, the thermal averages are to be carried out in the *ground state* prior to x-ray absorption, rather than in relaxed final states. Now, for any harmonic Hamiltonian or gaussian disorder one has the exact result [18]

$$\left\langle e^{i2k \sum_i (\vec{u}_i - \vec{u}_{i+}) \cdot \hat{R}_{ii+}} \right\rangle = e^{-2k^2 \sigma_j^2}, \quad (1.7)$$

where σ_j^2 denotes the mean square fluctuation in the effective path length R_j

$$\sigma_j^2 = \frac{1}{4} \left\langle \left[\sum_{i=1}^{n_j} (\vec{u}_i - \vec{u}_{i+}) \cdot \hat{R}_{ii+} \right]^2 \right\rangle. \quad (1.8)$$

For example, in the SS case of two atoms at sites $\vec{0}$ and \vec{R} ,

$$\sigma_R^2 = \left\langle [(\vec{u}_R - \vec{u}_0) \cdot \hat{R}]^2 \right\rangle = \left\langle (\vec{u}_R \cdot \hat{R})^2 \right\rangle + \left\langle (\vec{u}_0 \cdot \hat{R})^2 \right\rangle - 2 \left\langle (\vec{u}_R \cdot \hat{R})(\vec{u}_0 \cdot \hat{R}) \right\rangle. \quad (1.9)$$

Thus, if one neglects the variation of all terms but the rapidly varying oscillatory function in Eq. (1.3) and assumes small harmonic displacements, $\sigma_j/R_j \ll 1$, Eq. (1.2) is recovered.

Equation (1.8) shows that σ_j^2 is not merely a sum of mean square displacements $\langle u_i^2 \rangle$ at scattering sites but also includes the displacement-displacement correlation terms $\langle u_{i\alpha} u_{k\beta} \rangle$, where α and β denote Cartesian indices x , y and z . These correlations decay algebraically with distance and are such that only modes contributing to motion along a bond path are important. Therefore, in contrast to the mean square displacement $\langle u_{i\alpha}^2 \rangle$ which appears in the x-ray diffraction DW factor, σ_j^2 depends on fluctuations in pair distances and, thus provides a direct measure of the displacement-displacement correlation function. As will be shown below σ_j^2 is also related to a certain projected local vibrational density of states (VDOS) and, therefore is determined by the local vibrational structure.

We will discuss our results in comparison with two isotropic models commonly used for calculations of the XAFS DW factors, namely the CD and CE models [19]. Such an isotropic approach may not be able to provide an adequate description of vibrational properties for heterogeneous structures and, hence can lead to poor agreement with experimental data. Therefore, it is important to have a more general microscopic approach to the DW factor calculations which could be effectively applied to SS as well as MS terms.

In the following two subsections we will briefly review the standard CD and CE models often adopted for approximating XAFS DW factors and which are used for comparison with EM method in Chap. 2–3.

1.4.2 *Correlated Debye model*

The CD model is essentially a spherical approximation to σ_R^2 in terms of the eigenmodes (Eq. (2.9)) and leads to a projected VDOS for an atomic bond $(\vec{0}, \vec{R})$ of the form [19]

$$\rho_R(\omega) = \frac{3\omega^2}{w_D^3} \left[1 - \frac{\sin(\omega R/c)}{\omega R/c} \right]. \quad (1.10)$$

Here $\omega_D = k_B\theta_D/\hbar$ is the Debye frequency, θ_D is the Debye temperature, $c = \omega_D/k_D$ is the Debye approximation for the speed of sound, $k_D = (6\pi^2 N/V)^{1/3}$, and N/V is the atomic density number in the crystal. The second term in the brackets accounts for correlations and depends on bond length. In the CD approximation the displacement-displacement correlation function, which appears in Eq. (1.8), can be written as [11]

$$\langle u_{i\alpha} u_{j\beta} \rangle = \frac{3k_B T}{\omega_D^2 \sqrt{M_i M_j}} \int_0^1 dw y \frac{\sin(wx)}{x} \coth \frac{wy}{2}, \quad (1.11)$$

where $x = k_D R_{ij}$, $y = \theta_D/T$, and w is a dimensionless frequency variable. This integral is implemented in the FEFF [20] code using a Simpson-Romberg algorithm.

1.4.3 Correlated Einstein model

The CE model approximates the vibrational spectrum with a single delta-function centered at the effective vibrational frequency $\omega_E(R_j)$, which in general, depends on the path of interest,

$$\rho_j(\omega) = \delta(\omega - \omega_E(R_j)). \quad (1.12)$$

The Einstein frequency $\omega_E(R_j)$ for the XAFS DW factor for scattering path j can be interpreted in terms of the local potential energy in the deformed lattice state $|Q_j(0)\rangle$, i.e. $\omega_E^2(R_j) = \langle Q_j(0)|D|Q_j(0)\rangle$. In the SS case, for example, $\omega_E(R)$ is related to the local effective bond-stretching force constant $k_R = \mu_R \omega_E^2(R)$. This value of $\omega_E(R)$ is equivalent to the “natural” vibrational frequency of the bond $(\vec{0}, \vec{R})$ together with all attached neighboring bonds, but regarding all other masses as fixed [7,21]. Similarly, for a MS path j the potential energy $(1/2)k_j\sigma_j^2$ of a stretched path j with path length fluctuation $2\sigma_j$ is equal to that of a single spring model with reduced mass μ_j (see Eq. (2.11)) and spring constant $k_j \equiv \mu_j \omega_E^2(R_j)$. The CE model is particularly

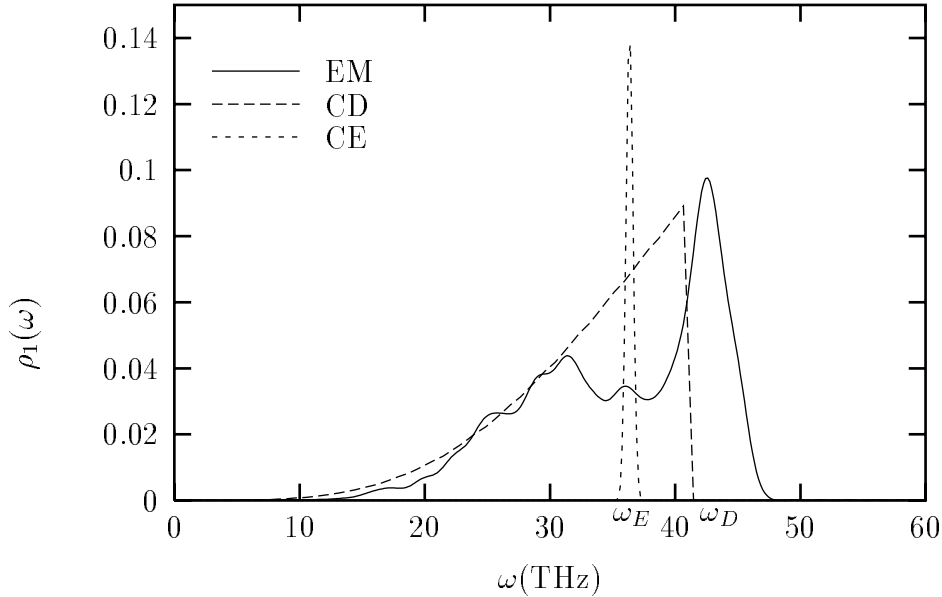


Figure 1.2: Projected VDOS $\rho_R(\omega)$ for the first shell of Cu calculated using the EM method with $N = 459$ and $k_1 = 27.9$ N/m (solid), in comparison with the CD (long dashes) and CE (short dashes) models.

appropriate for materials with $\rho_j(\omega)$ sharply peaked around a single frequency, but otherwise has most of the advantages and disadvantages of the CD model.

In general, depending on the form of the vibrational spectra, one or the other of these phenomenological models may provide a better approximation, but neither is usually adequate for heterogeneous systems. Plots of projected VDOS $\rho_R(\omega)$ for the first shell of Cu calculated using our non-isotropic EM method with a single central force constant ($k_1 = 27.9$ N/m, see Sec. 2.5.1 for details), the CD ($\theta_D = 315$ K [22]) and CE ($\theta_E \equiv \hbar\omega_E/k_B \simeq 3/4\theta_D \simeq 236$ K) models are presented in Fig. 1.2.

Chapter 2

EQUATION-OF-MOTION METHOD

Although the EM method was first introduced over 20 years ago, it has never been applied to calculations of the MS XAFS DW factors up until now. In fact, up to this time the MS formalism has never been developed. The importance of having a general non-isotropic approach for calculations of this kind has been already outlined in Chap. 1. Here we present a general formalism of the EM method in relation to the SS and MS XAFS DW factor calculations together with the results of its sample applications to crystalline Cu and Ge, and the organic molecule of zinc tetraimidazole (Sec. 2.5).

The EM method is a finite temperature method first introduced by Beeman, Alben and Rehr [23–25] for calculation of total VDOS and related quantities. This technique builds in Bose-Einstein statistics and allows one to calculate $\sigma_j^2(T)$ either in real time or in the frequency domain. The EM method is a significant improvement over conventional isotropic models such as the CD and CE models. It is very efficient for large systems since diagonalization of huge matrices is not required and the computational time scales linearly with the size of a cluster.

2.1 Formalism

The EM method is based on solving $3N$ coupled Newton's equations of motion with initial conditions depending uniquely on a given scattering path, where N is the number of atoms in the cluster. Regarding the total potential energy V of the crystal lattice as a function of the atomic displacements \vec{u}_i from their equilibrium positions,

and making use of a harmonic approximation, one obtains the equations of motion [18],

$$\frac{d^2 Q_{i\alpha}(t)}{dt^2} = - \sum_{k\beta} D_{i\alpha,k\beta} Q_{k\beta}. \quad (2.1)$$

Here $\vec{Q}_i = \vec{u}_i \sqrt{M_i}$, M_i is the mass of the atom at site i , and $D_{i\alpha,k\beta} = \Phi_{i\alpha,k\beta} / \sqrt{M_i M_k}$ is the dynamical matrix of order $3N \times 3N$ where $\Phi_{i\alpha,k\beta}$ are the second derivatives of the potential energy with respect to the atomic displacements $u_{i\alpha}$ and $u_{k\beta}$ taken at the equilibrium configuration. Upon substituting the canonical displacement vectors \vec{Q}_i expanded in normal coordinates q_λ ,

$$\vec{Q}_i = \sum_{\lambda} \vec{e}_i(\lambda) q_\lambda \quad (2.2)$$

into the definition of the mean square fluctuation in the effective path length R_j , these equations of motion lead to a standard eigenvalue problem for the normal modes,

$$\omega_\lambda^2 \epsilon_{i\alpha}(\lambda) = \sum_{k\beta} D_{i\alpha,k\beta} \epsilon_{k\beta}(\lambda). \quad (2.3)$$

Then evaluating the thermal average using Bose-Einstein statistics,

$$\omega_\lambda^2 \langle q_\lambda \rangle^2 = \langle n(\omega_\lambda) + \frac{1}{2} \rangle \hbar \omega_\lambda = \frac{\hbar \omega_\lambda}{2} \coth \frac{\hbar \omega_\lambda \beta}{2}, \quad (2.4)$$

one obtains a frequency domain formula for σ_j^2 ,

$$\sigma_j^2(T) = \frac{\hbar}{2\mu_j} \int_0^{\omega_{max}} \frac{d\omega}{\omega} \rho_j(\omega) \coth \frac{\beta \hbar \omega}{2}. \quad (2.5)$$

Here μ_j is a projected, or effective, reduced mass for scattering path j that insures normalized initial conditions (see Eq. 2.11), $\beta = 1/k_B T$, $\omega_{max} \gtrsim z \sqrt{k_1/\mu_1}$ is maximum frequency of the lattice motion, z is the coordination number, k_1 is the central first-neighbor force constant, μ_1 is reduced mass of the scattering center and its first neighbor, and

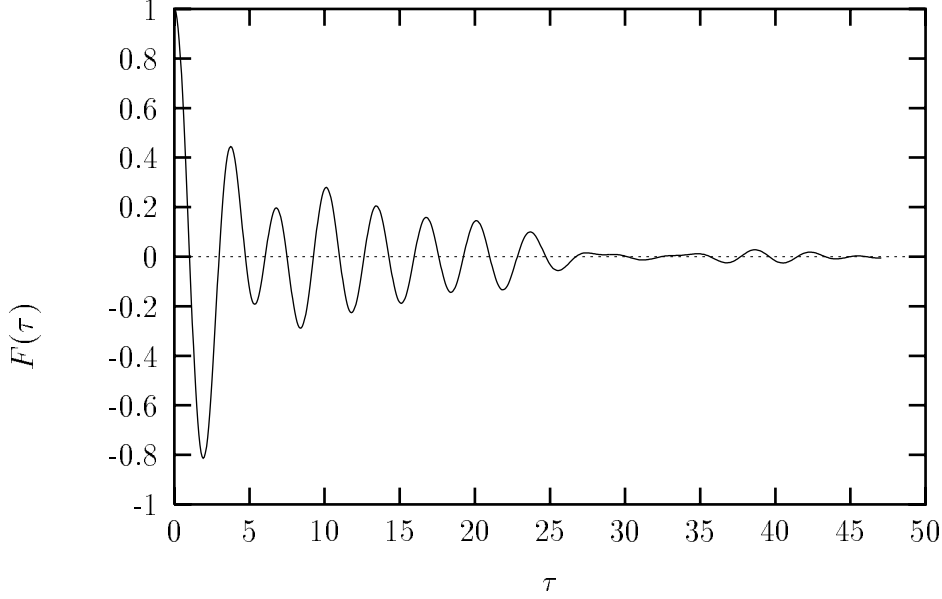


Figure 2.1: Example of the displacement-displacement autocorrelation function with a cutoff term, $F(\tau) \equiv \langle Q_1(\tau)|Q_1(0)\rangle e^{-\varepsilon\tau^2}$, for the first shell in Cu at 300 K vs a dimensionless time parameter $\tau = t/t_0$. Fourier transform of this function defines projected VDOS (see Eq. 2.6).

$$\rho_j(\omega) \equiv \sum_{\lambda} |\langle \lambda | Q_j(0) \rangle|^2 \delta_{\Delta}(\omega - \omega_{\lambda}) = \frac{2}{\pi} \int_0^{t_{max}} \langle Q_j(t) | Q_j(0) \rangle \cos \omega t e^{-\varepsilon t^2} dt \quad (2.6)$$

is the projected VDOS contributing to σ_j^2 . In the time integration $\varepsilon = 3/t_{max}^2$ and $t_{max} = \sqrt{6}/(\omega_{max}\Delta)$ are cutoff parameters that fix the net spectral resolution width Δ (typically 5% of the bandwidth), δ_{Δ} is a narrow δ -like function of width Δ , $\langle Q_j(t) | Q_j(0) \rangle = \sum_{i,\alpha}^{n_j} Q_{i\alpha}(t) Q_{i\alpha}(0)$ is the displacement-displacement autocorrelation function. The displacement state vector $|Q_j(t)\rangle$ is determined by integrating the equations of motion (2.1) numerically using a two-step difference equation approximation with initial velocities set to zero and initial displacements $|Q_j(0)\rangle$. The specific form of the initial displacements depends on the scattering path, as defined below. The cutoff parameters are introduced for efficiency in the calculation, and

focus on the local environment by cutting off long distance behavior.

By substituting Eq. (2.6) for $\rho_j(\omega)$ into (2.5) and evaluating the Fourier transform, one obtains an equivalent real time expression for $\sigma_j^2(T)$

$$\sigma_j^2(T) = \frac{\hbar}{\mu_j \pi} \int_0^{t_{max}} dt \langle Q_j(t) | Q_j(0) \rangle \ln \left[(2 \sinh \frac{\pi t}{\beta \hbar})^{-1} \right] e^{-\varepsilon t^2}. \quad (2.7)$$

Therefore, in principle, it is not necessary to determine $\rho_j(\omega)$ as an intermediate step, and $\sigma_j^2(T)$ can be explicitly calculated from the corresponding displacement-displacement autocorrelation function. Note that in the time domain the Bose-Einstein weight factor is equal to $-\ln[2 \sinh(\pi t / \beta \hbar)]$ and reduces for long time t to $-\pi t / \beta \hbar$ at high temperatures and $\ln(\beta \hbar / 2 \pi t)$ at low. The time integration limit t_{max} is usually of the order of a few vibrational cycles and requires typically 25–35 time-steps per cycle. All the integrals in our implementation of the EM method are evaluated using the trapezoidal rule, which is appropriate for highly oscillatory integrands.

2.2 Multiple scattering σ_j^2

Let us now apply the EM method to calculation of σ_j^2 for a general MS path. The sum of terms in Eq. (1.8) can be regrouped in the following way,

$$\sigma_j^2 = \left\langle \left[\sum_{i=1}^{n_j} \vec{u}_i \cdot \left(\frac{\hat{R}_{ii-} + \hat{R}_{ii+}}{2} \right) \right]^2 \right\rangle. \quad (2.8)$$

Adopting a vector expansion of the displacements from Eq. (2.2), and evaluating the average using Bose-Einstein statistics (Eq. (2.4)), one can rewrite Eq. (2.8) as

$$\sigma_j^2 = \frac{\hbar}{2\mu_j} \sum_{\lambda} \frac{1}{\omega_{\lambda}} \coth \frac{\beta \hbar \omega_{\lambda}}{2} \sum_i \left[\sqrt{\frac{\mu_j}{M_i}} \left(\frac{\hat{R}_{ii-} + \hat{R}_{ii+}}{2} \right) \cdot \vec{\epsilon}_i(\lambda) \right]^2. \quad (2.9)$$

The term in square brackets corresponds to the weight $|\langle \lambda | Q_j(0) \rangle|^2$ in Eq. (2.6) and

can be interpreted as the normalized probability that the initial displacement state, i.e. the N -dimensional vector with only n_j non-zero components

$$|Q_j(0)\rangle \equiv \begin{pmatrix} \sqrt{\frac{\mu_j}{M_1}}(\hat{R}_{1,n_j-} + \hat{R}_{1,2})/2 \\ \vdots \\ \sqrt{\frac{\mu_j}{M_i}}(\hat{R}_{ii-} + \hat{R}_{ii+})/2 \\ \vdots \\ 0 \end{pmatrix}, \quad i = 1, \dots, n_j \quad (2.10)$$

is in vibrational mode $|\lambda\rangle = |\vec{\epsilon}_1(\lambda), \dots, \vec{\epsilon}_N(\lambda)\rangle$. Here μ_j is defined so that $\langle Q_j(0)|Q_j(0)\rangle = 1$, which forces the projected VDOS $\rho_j(\omega)$ to be unit normalized,

$$\frac{1}{\mu_j} \equiv \sum_{i=1}^{n_j} \frac{1}{M_i} \left(\frac{\hat{R}_{ii-} + \hat{R}_{ii+}}{2} \right)^2. \quad (2.11)$$

For example, in the special case of SS the EM initial displacement state is defined as

$$|Q_R(0)\rangle \equiv \begin{pmatrix} -\sqrt{\frac{\mu_R}{M_0}}\hat{R} \\ \sqrt{\frac{\mu_R}{M_R}}\hat{R} \\ 0 \\ \vdots \end{pmatrix}, \quad (2.12)$$

where $\mu_R = (1/M_R + 1/M_0)^{-1}$ is the reduced mass for the $(\vec{0}, \vec{R})$ bond pair.

In order to simplify Eq. (2.9) one can define a normalized, local VDOS $\rho_j(\omega)$ as in Eq. (2.6), which leads to the frequency domain formula for MS σ_j^2 in Eq. (2.5). The VDOS spectrum $\rho_j(\omega)$ can be interpreted as the “sound” of the lattice plucked along the displacement vectors given by the initial conditions.

2.3 Force field models

The EM formalism presented above gives a relation between XAFS DW factors and the local microscopic environment around the scattering center. In order to apply

the method, knowledge of the local FF describing effective interatomic interactions or dynamical matrix D is required. Clearly, the choice of the model depends on the type of the interatomic bonds. For practical considerations the model should be kept as simple as possible, i.e. the number of its independent parameters should be small yet sufficient to avoid unphysical zero frequency modes and to have an accuracy to within a few percent.

One commonly used model is the VFF model [26–28] which expresses energy changes in terms of changes in “internal coordinates” such as bond lengths $\delta r_{ij} = (\vec{u}_i - \vec{u}_j) \cdot \hat{R}_{ij}$, bond angles $\delta\theta_{ijk}$, and torsional angles (or dihedrals) $\delta\tau_{ijkl}$. Since the latter typically are very small (under a few percent of the leading bond stretching interaction), we will ignore them in our FF model. The potential energy of the lattice deformation in this case can be written as a quadratic form

$$V = \frac{1}{2} \sum k_r^{ij} (\delta r_{ij})^2 + \frac{1}{2} \sum k_\theta^{ijk} (\delta\theta_{ijk})^2 + \dots \quad (2.13)$$

Here k_r^{ij} is a bond-stretching force constant for nearest neighbors i and j , k_θ^{ijk} is a bond bending force constant corresponding to an angular rigidity for the angle θ_{ijk} , and remaining terms are due to contributions from non-central interactions proportional to products of changes in different internal coordinates, e.g. $(\delta r_{ij}) \cdot (\delta r_{jk})$, $(\delta r_{ij}) \cdot (\delta\theta_{iji})$, etc. Because interatomic bonds are crucial for describing interactions in molecules and covalent crystals, the VFF model is particularly effective for such structures. An advantage of the model is that the dependence of the deformation energy solely on deformations of the bonds makes it rotationally invariant. For some materials (e.g. copper crystal) only a single near neighbor force constant is needed to approximate most of the structure in vibrational spectra and to obtain σ_j^2 in good agreement with experiment. Sometimes it is more convenient to introduce effective central interactions with further neighbors rather than using bond angles and/or cross-terms, although such interactions may not correspond to “real” chemical bonds.

We adopted this type of interaction in our method in addition to the interactions in the traditional VFF model.

There exist a large number of other prescriptions for treating lattice deformations. These include the Born [29] and Keating [30] models which are used primarily for diamond-type crystals. In any case, the first near neighbor central forces-constants are usually the largest in the interaction picture.

In the present chapter we will not consider effects arising from anharmonic corrections to the potential energy. In general, anharmonicity leads to interactions between the various modes, and gives a contribution to $\sigma_j^2(T)$ that increases with temperature. Further discussions on this topic can be found elsewhere [7, 17, 21, 31]. Due to anharmonic effects, the Gaussian approximation for DW factor Eq. (1.1) is not precisely valid, and the general cumulant expansion [12, 17] has to be considered instead. These corrections are briefly discussed in Sec. 5.1.

2.4 How to find the right FF model

The answer to this question largely depends on the system for which FF model is needed. Unfortunately, as of now, there is no single solution to this problem. There is an extensive review of the existing FF models by Landis *et al.* [28] (includes 251 references) which I would strongly recommend reading for anybody who is interested in FF models in application to organometallic and organic materials and/or would like to have a better understanding of the current situation in molecular mechanics (MM) methods and computations.

The problem of finding the “right” FF model can be subdivided into two parts:

- Defining appropriate molecular topology (i.e. which atoms are bonded to which).
- Choosing the corresponding form of FF and determining its parameters.

Molecular topology determines the choice of the internal coordinates which in turn effects the choice of a FF model. In addition to bonded interactions (bond stretches, bond angles, torsions) to which we limited our VFF, some models used in MM also include nonbonded interactions (i.e. van der Waals and electrostatic interactions) [28]. In organic compounds the molecular topology is chosen in accordance with chemical localized bonds, and usually, is well defined. But in inorganic and organometallic materials which typically have highly delocalized bonding interactions and high coordination numbers dependent on the nature of ligands, assignment of bonds can be unclear (problem of indistinct topologies) [28]. An excellent reference source of structural and topological information for a great variety of inorganic and organometallic materials is *Structural Inorganic Chemistry* by A. F. Wells [32].

Since VFF is, perhaps, the most widely used model in modern MM and is the one adopted in our study, we will limit discussion of obtaining force constants to this particular model. However, not all VFF or VFF-based models are defined identically. Often VFF models are used in combination with Coulomb bonded and/or nonbonded interactions. There is also some freedom in the choice of a set of internal coordinates, as well as, in inclusion of off-diagonal terms (e.g. coupling between different stretches, angles, *etc.*) [28]. Since, there can be nonvanishing correlations between parameters of the same model, the question of transferability has to be addressed before trying to adopt force constants fitted within one set of parameters to a calculation based on a different set of parameters even for the same material. Within the accuracy requirements for σ^2 calculations (10–20%), most of the smaller parameters, such as torsions and off-diagonal terms, can usually be ignored, but Coulomb interaction for bonded terms has to be accounted for. Also, there is a strong correlation between first and second nearest neighbor stretches.

Existing approaches to FF calculation can be subdivided into the following three categories:

- Fit to experiment.
- *Ab initio* analytical calculations.
- FF parameterization and semiempirical methods.

2.4.1 *Fit to experiment*

FF parameters can be fit to a certain type of experimental data. The most direct approach in our case is to fit the force constants to the the measured XAFS spectrum much like Debye and Einstein temperatures are now being fit [12]. This can be done by including the SIGEM subroutine (see Appendix A) into the FEFFIT code [33], or by expressing Einstein temperature (frequency) in terms of force constants [34]. For example, for the first nearest neighbor single force constant in monoatomic fcc crystal lattices $\omega_E(R_1)^2 = 4 k_1/M$ [35] (assuming the force field consists of only one force constant which is a good approximation for fcc structures). Also, there is a relation between Debye and Einstein frequencies. For example, in fcc and bcc lattices $\omega_E(R_1) \simeq 3/4 \omega_D$ [17, 19]. These leads to the following formula connecting k_1 and θ_D in fcc structures,

$$k_1 = \frac{M}{4} \left(\frac{3 k_B \theta_D}{4 \hbar} \right)^2 \quad (2.14)$$

Hence, for Cu one would have $k_1 = 25.2$ N/m ($\theta_D = 315$ K, $M = 63.55$ u. [22]) and for Pt $k_1 = 41.3$ N/m ($\theta_D = 230$ K, $M = 195.09$ u. [22]). In general, for a force field approximated with a single nearest neighbor force constant, k_R , $\omega_E^2(R) = \zeta k_R/\mu_R$ where ζ is a constant depending on the symmetry of the structure. If one roughly (the error can be up to 25%) approximates the actual $\omega_E^2(R)$ with the second moment m_2 of the dynamical matrix¹ (see Chap. 3), then $\zeta = \langle Q_R(0) | \tilde{\Delta} | Q_R(0) \rangle$. Here matrix

¹ A more realistic approximation would be $\omega_E = 1/2 [(m_{-1})^{-1} + (m_{-2})^{-1/2}]$ [17, 25].

element of $\tilde{\Delta}$ for a bond R_{lm} between two nearest neighbors l and m characterized by the stretching force constant k_R and reduced mass μ_R is defined as

$$\tilde{\Delta}_{\alpha,\beta}(l, m) \equiv \frac{\mu_R}{\sqrt{M_l M_m}} \left(\sum_{i=1}^{N_m} \hat{R}_{im}^\alpha \hat{R}_{im}^\beta \delta_{lm} - \hat{R}_{lm}^\alpha \hat{R}_{lm}^\beta \right) \quad (2.15)$$

with the sum running over all nearest neighbors of atom m .

Huber and Herzberg compiled available vibrational (including Einstein frequencies) and structural data for all diatomic molecules and ions [36]. General formulas which relate parameters of VFF model with the normal modes for a number of molecules (e.g. XY_2 , X_2Y_2 , XY_4 , XYZ , *etc.*) are provided by Cyvin [37].

With some luck one can find force constants for the material being studied already fitted to some kind of experimental data in available publications. Although, one should keep in mind that fitted force constants even for the same material can vary greatly depending on the type of experimental data used in the fit. Since our force constants are of vibrational nature, the experimental data has to be chosen accordingly. For example, fits to experimental phonon dispersion curves (e.g. see [38] for c-C, c-Si, c-Ge, and α -Sn, [39] for MnO, CoO and NiO, [40, 41] for selected alkali halides), inelastic neutron scattering (e.g. see [4] for zinc tetraimidazole, [42] for $CH_3CCO_3(CO)_9$), infrared and/or Raman (e.g. see [43] for rubredoxin, [44] for Ge and Si) spectra, elastic constants (e.g. see [45] and [30] for selected tetrahedrally coordinated semiconductors) are appropriate, whereas fits to structural and thermodynamic data usually are of very limited use in our case. Osawa and Lipkowitz [46] provided an extensive list of references (more than 400) to published empirical FFs for organic and organometallic compounds.

Occasionally, especially in solid state physics, the form of the potential is chosen as a function of interatomic distances, $U(R)$, e.g. Morse, Born-Mayer, or Coulomb potentials [22], and parameters defining the form of this function are fitted to experimental data rather than the single force constants. In this case, single force constants

can be obtained by expanding the potential function in Taylor series (see [7] for an example application) [47].

2.4.2 *Ab initio calculations*

A number of codes which allow *ab initio* calculation of Hessian matrix, or matrix of second derivatives, (one would simply need to scale its matrix elements by appropriate mass parameters to get dynamical matrix) has been developed over the last 20 years. These include DGauss [48, 49], Gaussian [50], and CADPAC [51, 52] which are incorporated into the UniChem software package [53] developed within the Cray Research Center. DGauss is a molecular density functional theory (DFT) [54, 55] program using Gaussian-type molecular orbitals and designed for studying electronic, magnetic, and structural properties of atoms, molecules, and clusters. The use of DFT allows an approximate inclusion of electron correlation, an effect which is known to be important in the accurate prediction of molecular properties. DGauss features include calculation of analytic second derivatives, IR frequencies and intensities, Raman frequencies, electron densities of states (DOS), electrostatic potential fit charges, multipole moments, *etc.* DGauss allows to perform geometry optimization to both minima and transition states. It also offers a choice of exchange-correlation potentials to use in self-consistent field (SCF) calculations between a local density approximation (LDA), including different forms of Vosko, Wilk, and Nusair (VWN) functionals, and a general gradient approximation (GGA), including different forms of Perdew-Wang (PW) functionals (88-PW91, PW91-PW91) and others (B88-P86 (also called BP), and B88-LYP (also called BLYP)). Hessian is calculated using second derivative equations derived by Komornicki and Fitzgerald [56]. Due to the sizes of atomic basis sets used in DGauss to represent the molecular orbitals, calculations for systems of more than 15 atoms usually become very time consuming. Because of these system size limitations, it might be impossible to carry out geometry optimization and dynamical matrix calculation for an entire molecule in question but rather for a

small part of it which is of the most interest (for an example case see Section 4.1). Clearly, structural and vibrational properties of this fragment unaffected by force field from the rest of the structure can be different from those of the whole molecule. Thus again, in choosing the size of the fragment the question of transferability of the resulting force constants has to be considered. Also, a reasonable accuracy can be achieved by applying *ab initio* method to FF calculation for only a small fragment of the structure while using semiempirical FF for the remaining part. The accuracy of the calculated second derivatives in DGauss is typically around 10%. DGauss is considered to be one of the most reliable *ab initio* codes. Example application of DGauss for an anion of tetrachloroferrate (II) is presented in Section 4.1.

Gaussian is a system of programs which performs *ab initio*, density functional and semiempirical molecular orbital calculations. Analytic first derivatives are computed using MP2 method (second-order Moller-Plesset perturbation energy [57]), and computation of second derivatives is based on CASSCF (Complete Active Space Self-Consistent Field) method [50]. CADPAC (Cambridge Analytical Derivatives Package) uses *ab initio* molecular orbital theory to compute properties of atoms and molecules quantum mechanically. It is based on SCF approach and Gaussian atomic basis set and supports Hartree-Fock wavefunctions. CADPAC can calculate force constants by fully analytic methods (SCF, MP2, DFT) or by finite difference of gradients.

Force constants can also be derived from molecular dynamics simulation codes by measuring change in the total energy or by tracking forces acting on atoms in the bond of interest as functions of changes in relevant internal coordinates. This can be done by using, for example, the *ab initio* Car-Parrinello (CP) [58] code developed by Hannes Jonsson and his group [59] and based on generalized norm-conserving pseudopotentials [60,61]. The method is implemented by using plane-wave expansion of electronic orbitals and can be successfully applied to finite (less than 100 atom) clusters of crystalline materials. Tests of the method for a 64-atom c-Ge cluster gave

preliminary results for the first nearest neighbor force constant $k=138$ N/m in comparison with 120 N/m used in Section 2.5.2. Additional force constants corresponding to different bond angle bendings can be obtained from CP molecular dynamics simulations by “freezing” all but a few relevant atoms in a cluster.

2.4.3 *FF parameterization and semiempirical methods*

The FF parameterization and semiempirical methods which adopt these parameterized FFs are based on the assumption of transferability of the FF parameters from one compound to another for similar bonds. In MM applications to organometallic and organic systems, parameters of FF models are usually fit to such experimental data as infrared and Raman vibrational spectra [27], structural information, and thermodynamic data. Since the use of structural data in fitting FF parameters is the most frequent practice [62], the resulting FF models might be of limited use to someone interested in vibrational properties. Although, these models are usually able to predict force constants for typical organic bonds such as, for example, C–C, C=C, N–C, N–H, *etc.*), within about 30%. They can also be used in combination with *ab initio* methods. Because most of the efforts in development and implementation of methods for FF calculations are concentrated in the areas of organic chemistry, the available FFs (e.g. AMBER, CHARMM, MM1, MM2, MM3, DREIDING [28]) are parameterized generally for organic materials and without modifications either can not be applied to inorganic and organometallic materials at all (for the lack of needed parameters) or lead to poor agreement with experiment. Also, application of these MM FFs is typically limited to molecules and is not suited for calculations in inorganic crystals.

Although there has been some progress done in the direction of developing general FF models, these models usually perform poorly for inorganic and organometallic materials. One of the earliest models, which with some modifications is still being widely used, is, so called, the Badger’s rules [63, 64]. Badger expressed stretching

force constant k_R for a bond between two arbitrary atoms in a molecule as a simple function of the interatomic distance R :

$$k_R = \frac{C_{ij}}{(R - d_{ij})^3}. \quad (2.16)$$

Here k_R is in the units of N/m, R is in Å, and C_{ij} and d_{ij} are constants dependent upon periodic table rows containing the two atoms (see Table 2.1). The accuracy of the formula in predicting bond stretches is very inconsistent varying from an 8% error for a diatomic molecule of SiF (in comparison with experiment [65]) to a 21% error in CF and 12% in Na₂ molecules. Also, application of the model based on the original Badger's parameters is limited to mostly diatomic molecules and fails for crystalline materials. There has been some work done on generalization of this original formula (see a list of references in [66]). Badger's formula with slightly modified parameters has been used for prediction of force constants of large molecules using artificial neural network (ANN) method [67]. Fischer *et al.* showed that ANN can provide force constants within a 1.5 to 5% error band.

One of the recent and most general FF models available is the UFF (Universal force field) model developed by Rappe *et al.* [66]. Parameters used in the UFF were fitted for a large number of mostly organic molecules and depend on the types of elements in the bond, their hybridization, and connectivity. The total potential energy of a molecule is expressed as a sum of valence (bonded) and nonbonded interactions:

$$V = V_R + V_\theta + V_\phi + V_\omega + V_{vdW} + V_{el}, \quad (2.17)$$

where bond stretching term $V_R = 1/2 \sum_{ij} k_{ij}^R \delta r_{ij}^2$, bond angle bending $V_\theta = \sum_{ijk} k_{ijk}^\theta \times \sum_n A_n \cos n\theta$, dihedral angle torsion $V_\phi = \sum_{ijkl} k_{ijkl}^\phi \sum_n B_n \cos n\phi_{ijkl}$, and inversion term $V_\omega = \sum_{ijkl} k_{ijkl}^\omega (C_0 + C_1 \cos \omega_{ijkl} + C_2 \cos 2\omega_{ijkl})$ are valence interactions, whereas the nonbonded interactions consist of van der Waals forces

Table 2.1: Values of the parameters in Badger’s model for diatomic molecules. Here C_{ij} is in such units that k_R is in N/m.

Type of Molecule				
Atom j	Atom j	Example	C_{ij}	d_{ij} (Å)
Element in row 1	Element in row 1	NO, O ₂	186.17	0.68
— row 1	— row 2	SO, PN	1.53	0.94
— row 1	— row 3	TiO	1.25	1.06
— row 1	— row 4	SnO	1.18	1.18
— row 1	— row 5	PbO	1.18	1.26
— row 2	— row 2	Cl ₂ , S ₂	1.18	1.25
— row 2	— row 4	ICL	1.29	1.48
— row 3	— row 3	Br ₂ , K ₂	1.29	1.48
— row 4	— row 4	I ₂	1.18	1.76

$$V_{vdW} = \sum_{i,j} D_{ij} \left[-2 \left(\frac{x_{ij}}{x} \right)^6 + \left(\frac{x_{ij}}{x} \right)^{12} \right], \quad (2.18)$$

and electrostatic interactions $V_{el} = \sum_{i,j} \gamma Q_i Q_j / (\epsilon R_{ij})$. Here V is in units of joules, $\gamma = 230.718 \times 10^{-20}$, coefficients A_n , B_n , C_n are chosen to satisfy appropriate boundary conditions, D_{ij} is the well depth, x_{ij} is van der Waals bond length, Q_i and Q_j are charges in electron units, R_{ij} is the distance in Å, and ϵ is the dielectric constant (default $\epsilon = 1$). Note that nonbonded interactions are excluded for atoms that interact via a bond stretch or angle bend (i.e. (1,2 interactions) and (1,3 interactions)). In the UFF model the bond length r_{ij} entering into the formula for V_R is defined as a sum $r_{ij} = r_i + r_j + r_{BO} + r_{EN}$, where r_i (r_j) is a single bond radii, $r_{BO} = -\lambda(r_i + r_j) \ln(n)$ is a bond order correction term ($\lambda = 0.1332$ and n is the bond order), and r_{EN} is electronegativity correction of O’Keeffe and Brese [68] (it is typically a 1–3% correction and can be ignored in our case). The bond stretching force constants are based

on generalization of Badger’s rules and defined by formula

$$k_{ij} = K \frac{Z_i^* Z_j^*}{r_{ij}^3}, \quad (2.19)$$

where k_{ij} is in units of N/m, $K = 461.43$ and Z_i^* (Z_j^*) is effective atomic charge in electron units. The angle bend force constants are based on angular generalization of Badger’s rules and defined by formula

$$k_{ijk} = \beta \frac{Z_i^* Z_k^*}{r_{ik}^5} [r_{ij} r_{jk} (1 - \cos^2 \theta_0) - r_{ik}^2 \cos \theta_0], \quad (2.20)$$

where k_{ijk} is in units of J/rad², all r ’s are in units of Å, $r_{ik}^2 = r_{ij}^2 + r_{jk}^2 - 2r_{ij}r_{jk} \cos(\theta_0)$, and $\beta = 461.43$. Selected UFF parameters (r_i , θ_0 , and Z_i) are given in Appendix B (Table B.1). For further details on these and other UFF parameters see the original paper by Rappe *et al.* [66].

My experience with this table showed that it works fairly well for predicting strong (above 400 N/m) organic bonds (e.g. C–C, C=C, C≡C, N–C, C–H, N–H *etc.*) but overestimates some organometallic bonds (e.g. Zn–N, Fe–Cl) and, for example, Ge–Ge bond in crystalline Ge by about a factor of 2. The model absolutely fails for such weak bonds (under 20 N/m) as, for example, in diatomic molecules (e.g. CO, LiCl, NaBr). Therefore, my recommendation in using this model for predicting force constants is that it can be safely used for strong organic bonds, used with caution (might want to divide the results by 2) for organometallic bonds which typically fall into range of 80–200 N/m, and do not trust the numbers for bonds you think are relatively weak (below 70 N/m). Also, one should not rely on this model for crystalline structures, and rather limit its use to large molecules. The limitations in the accuracy of the UFF force constants are largely due to the fact that the model’s parameters were fit mostly to structural data, and were developed primarily for determining molecular structures. The model is known to predict well (within 0.1 Å for bonds and 5–10° for angles) structural features of organic and organometallic

compounds [66].

2.5 Applications

2.5.1 Cu

The first crystalline structure examined in our MS calculations was a 459-atom spherical cluster of a copper crystal with fcc lattice symmetry. Although our method was designed for general aperiodic systems, we chose fcc Cu since it has often been used as a test case for DW and other XAFS studies and accurate XAFS data is available. Following the model of Alben and Rehr [24], only a single central interaction between the first nearest neighbors with force constant $k_1 = 27.9$ N/m was taken into account.

Example results for the first shell SS path and for the 111 triangular MS path versus temperature are shown in Fig. 2.2 in comparison with the CD model ($\theta_D = 315$ K [22]) results calculated by the FEFF code, as well as with experimental data [1,2] and the CE model for the first shell ($\theta_E = 3/4\theta_D \simeq 236$ K [19]). Our results for SS σ_R^2 are in excellent agreement (within 0.3% for the first and second shells, and within 3% for the third shell) with those obtained by Sevillano *et al.* [19] using full lattice dynamical calculations. Excellent agreement with experiment at lower temperatures is also reached. At higher temperatures, i.e. above 500 K, the error between our theory and experiment is likely due to anharmonic effects. The results for σ_j^2 indicate that at all temperatures, the CD model is in good agreement with the EM method for the first shell SS path, i.e. the 10% difference is within the error bars of the two methods. A larger difference (about 25% at high temperatures) is observed for the 111 path. The discrepancies between the two models are smaller at low temperatures. Projected vibrational densities of states $\rho_j(\omega)$ for the two paths are shown in Fig. 2.3a. Note that the VDOS for the 111 triangular path has a sharper dominant peak at about 42 THz, i.e. the $\rho_j(\omega)$ is more monochromatic for this path. One can think about it as the fine tone of a musical “triangle”. This feature also explains the bigger error in

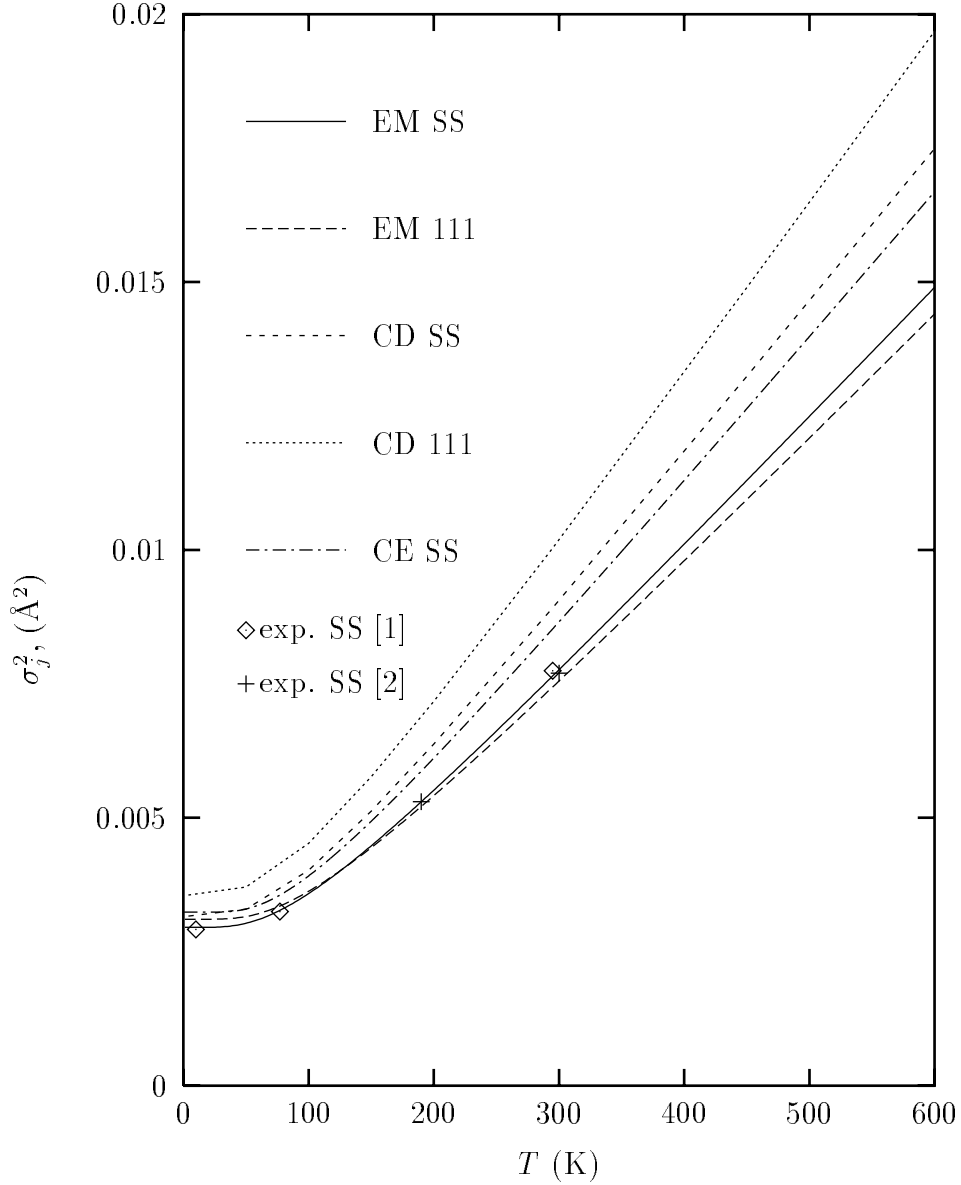


Figure 2.2: Mean square amplitudes σ_j^2 for a 459-atom cluster of Cu vs temperature as calculated from a single force constant ($k_1 = 27.9$ N/m) model for the first shell (EM SS) and for the 111 triangular MS path (EM 111). The CD model ($\theta_D = 315$ K) calculations for the first shell (CD SS) and the 111 triangular MS path (CD 111) and the CE model for the first shell (CE SS) are given for comparison. Points represent experimental values of σ^2 [1,2].

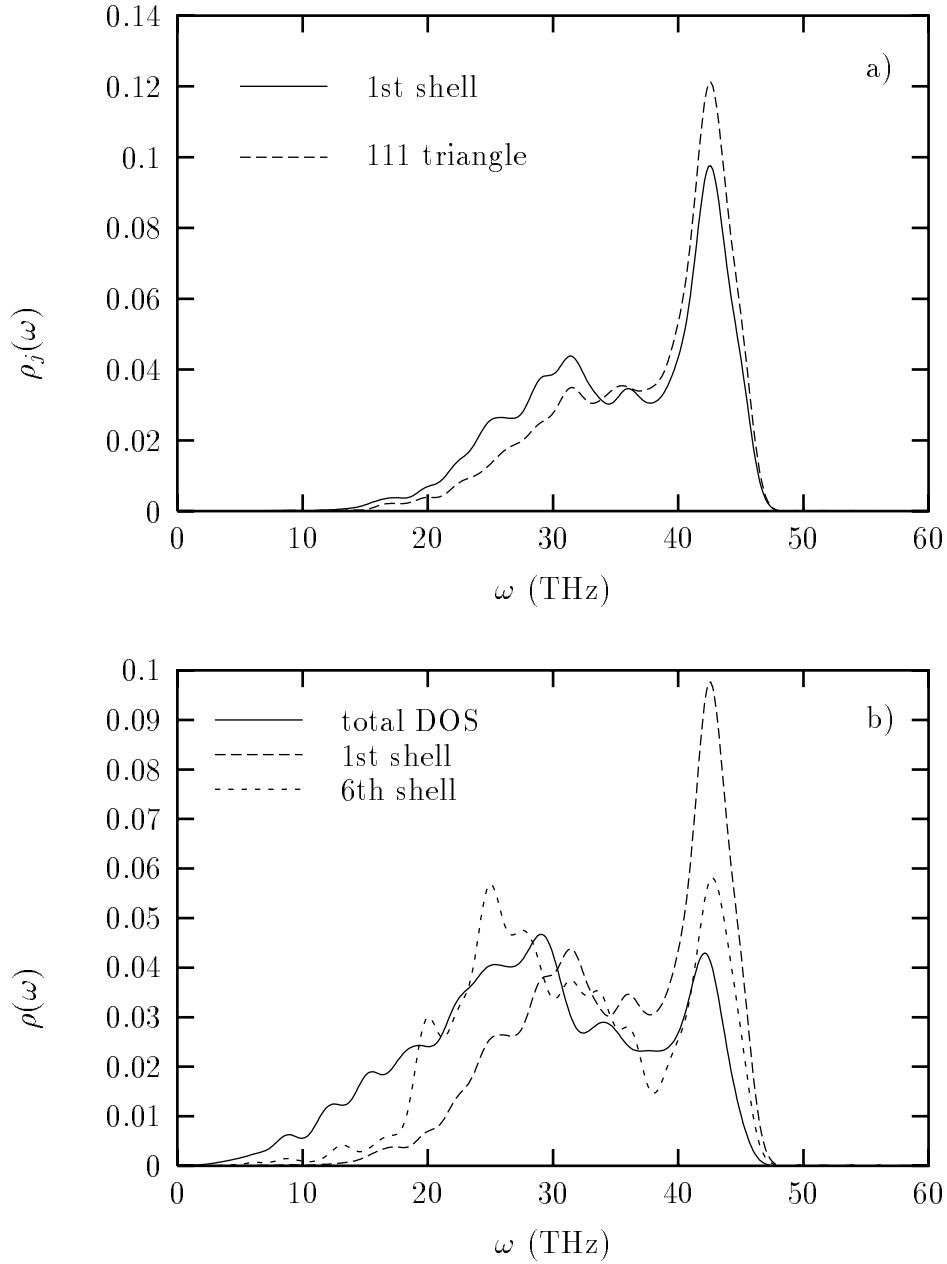


Figure 2.3: a) Projected VDOS $\rho_j(\omega)$ for the first shell (solid) and for the 111 triangular MS path (dashes) for Cu calculated via the EM method. b) Total VDOS $\rho(\omega)$ and projected VDOS $\rho_R(\omega)$ for the first shell and sixth shells of Cu calculated via the EM method.

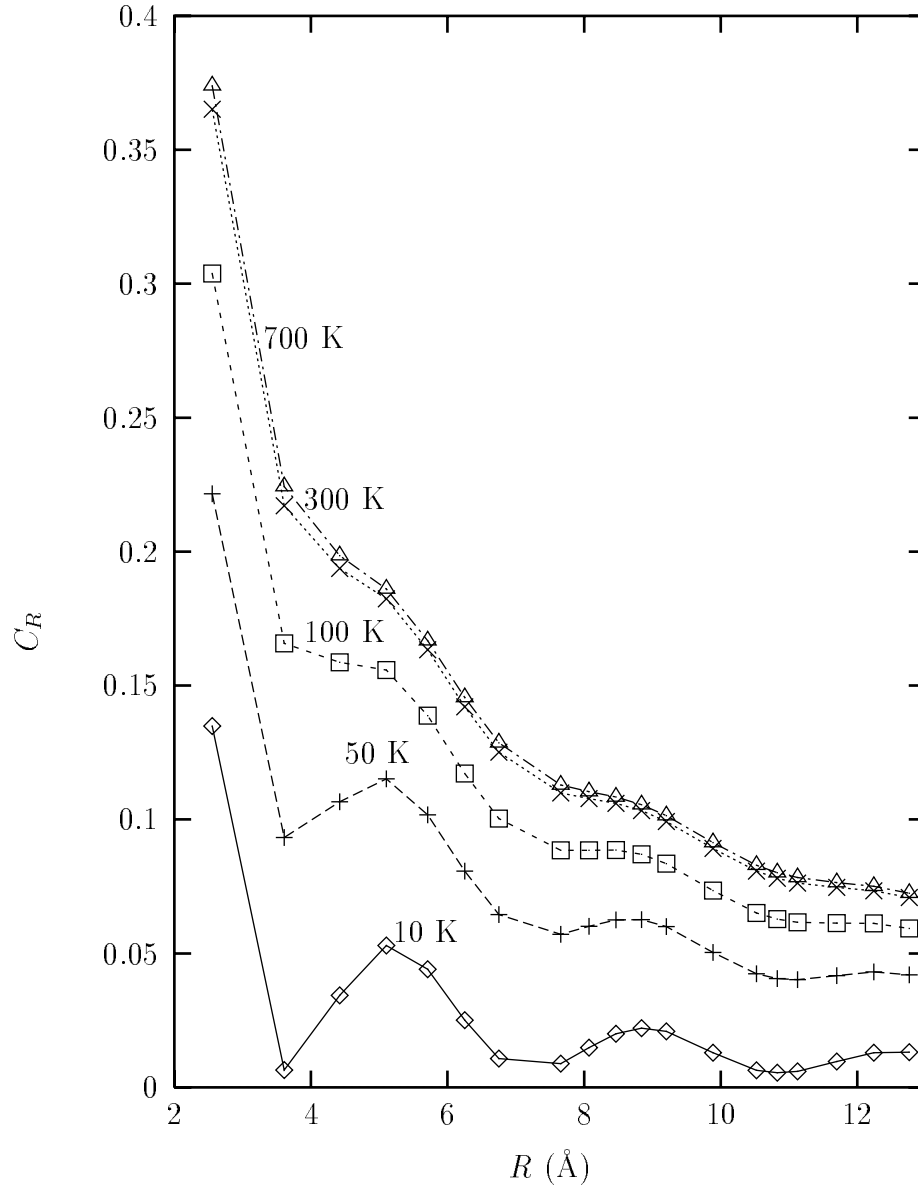


Figure 2.4: Radial dependence of the correlation function C_R calculated for Cu at different temperatures using FEFF code and CD model with $\theta_D = 315$ K. Points correspond to different coordination shells.

Table 2.2: Values of first shell SS σ_1^2 and MS σ_3^2 for 111 triangular MS path as calculated using EM method in comparison with CD model ($\theta_D = 315$ K) and experimental values [6].

T (K)	$\sigma_1^2 \times 10^{-3} \text{ \AA}^2$			$\sigma_3^2 \times 10^{-3} \text{ \AA}^2$		
	EM	CD	exp	EM	CD	exp
10	3.0(3)	3.2	3.4(1)	3.1(3)	3.6	4.2 ± 3.0
50	3.1(3)	3.3	3.5(1)	3.2(3)	3.7	4.1 ± 3.0
150	4.5(4)	5.1	5.2(2)	4.4(4)	5.8	5.3 ± 3.0

the CD $\sigma_j^2(T)$ for this path. Fig. 2.3b illustrates the importance of correlations for nearest neighbors as well as the decay of the correlation function with distance. Note that the projected VDOS for the sixth shell is very similar to the total VDOS which indicates that contribution from the correlations is negligible for the further shells. A more quantitative illustration of correlations is shown in Fig. 2.4. The correlation function

$$C_R = \left\langle (\vec{u}_R \cdot \hat{R})(\vec{u}_0 \cdot \hat{R}) \right\rangle / u^2 = 1 - \sigma_R^2 / (2u^2) \quad (2.21)$$

shows how fast σ_R^2 is approaching $u^2 = \langle (\vec{u}_0 \cdot \hat{R})^2 \rangle$. In CD approximation in low and high temperature limits one has [17, 25]

$$C_R = \begin{cases} \left(\frac{\sin(k_D R/2)}{k_D R/2} \right)^2, & T \rightarrow 0 \\ \frac{S_i(k_D R)}{k_D R}, & T \rightarrow \infty. \end{cases} \quad (2.22)$$

Note that correlations are stronger at higher temperatures and decay more slowly with distance.

DW factors for MS triangular paths are usually very hard to fit due to the weakness of XAFS signal contributed by these paths and their strong correlations with other fitting parameters. As a result, σ^2 for these paths typically have very large error bars.

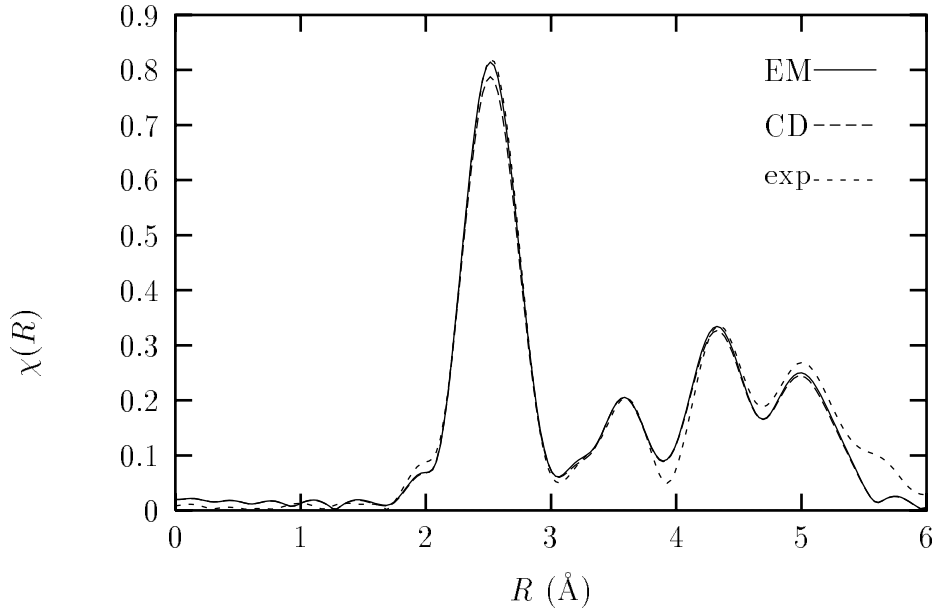


Figure 2.5: Magnitude of the phase corrected Fourier transform $\tilde{\chi}(R) = \text{FT}[k\chi(k)]$ for Cu at $T = 150$ K as extracted from experiment using the phase corrected FEFFIT code (solid line), and fitted using theoretical results with the DW factors calculated via the CD (long dashes) and single force constant EM (short dashes) models.

Values of first shell σ_1^2 and 111 triangle σ_3^2 as calculated via EM and CD methods in comparison with their values fit to XAFS experiment are presented in Tab. 2.2. As one can see both methods provide results within the error bars of the experiment.

This study shows that overall the CD model is a reasonably good approximation for Cu, which might be expected since the fcc structure is highly isotropic. This also can be seen from a comparison of the XAFS Fourier transform $\tilde{\chi}(R)$ with fits of theoretical FEFF calculations using DW factors obtained via the CD model and the EM method (see Fig. 2.5). Fits of theoretical $\tilde{\chi}(R)$ to experiment measured at 150 K were performed using a phase-corrected version of FEFFIT, i.e. with theoretical phase shifts taken from FEFF7. As fitting parameters for the EM model we used a shift of energy origin ΔE and a constant amplitude factor S_0^2 , whereas for the CD models we used ΔE and Debye temperature θ_D , and set S_0^2 equal to the value derived from

the EM fit (0.927). The data was fitted in the range between 1.7 and 5.2 Å for the 16 most significant scattering paths which span first four shells. The fitted value for θ_D was 327 ± 9 K, within error bars of the value $\theta_D = 315$ K [22]. As Fig. 2.5 shows, both methods yield XAFS in excellent agreement with experiment, though the EM method is noticeably better.

2.5.2 Ge

The second crystal considered in our study was a 147-atom spherical cluster of Ge of the diamond space group. In the application of the EM method to such loose, anisotropic structures like Ge, a single spring model is inadequate, and it is necessary to include noncentral forces to account for bond bending interactions. Otherwise there is no resistance to shear, and the projected VDOS exhibits an unphysical zero frequency mode. The force field model used in our calculations included central interactions out to the third neighbors ($k_1 = 120$ N/m for the first neighbors, 4.0 N/m for the second and -1.1 N/m for the third), and non-central bond-bending interactions [44] with $k_1^{nc} = 0.04 \times k_1$ fit to the experimental [3] VDOS. The values for the central interaction force constants were based on results of Goldammer *et al.* [38] and then adjusted by hand to fit experimental spectrum determined from neutron scattering [3].

Fig. 2.6 shows the calculated total and projected VDOS for this model in comparison with experimental total VDOS. The MS σ_j^2 at 300 K calculated by the EM method in comparison with results obtained from CD model ($\theta_D = 360$ K [22]) and several SS experimental values [2] are presented in Fig. 2.7 versus scattering paths index listed in order of increasing path length as generated by FEFF7. For example, path number 1 corresponds to first shell SS, 2 to second shell SS, 3 to 121 triangular MS path, 4 to triangular 211 MS path, 5 to third shell SS, 6 to double scattering from the first neighbor ($\sigma_6^2 = 4\sigma_1^2$) etc. According to the EM calculations for the first three paths, projected VDOS's for paths 1 and 3 (see Fig. 2.6) have sharper dominant

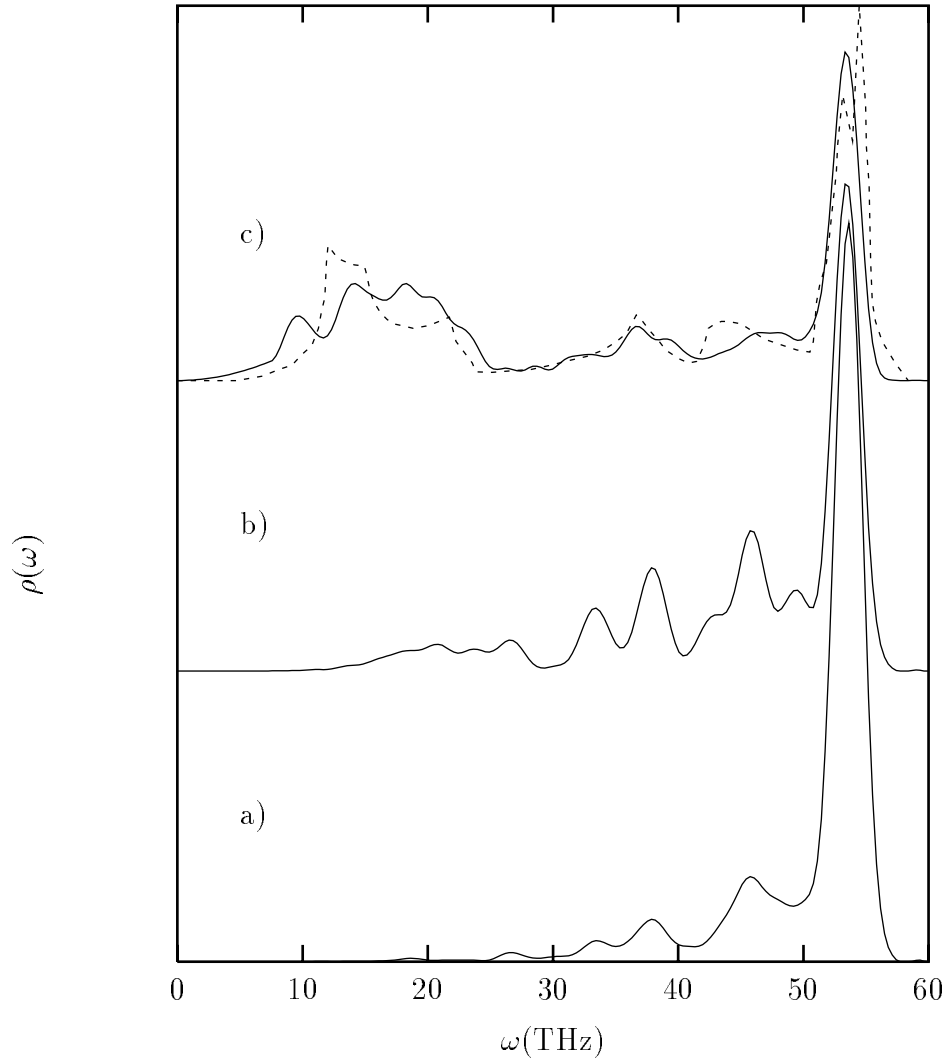


Figure 2.6: VDOS for a 633-atom cluster of Ge as calculated via the EM method: a) for the first shell, b) for 121 triangular MS path c) total experimental spectrum determined from neutron scattering [3] in comparison with theoretical total VDOS $\rho(\omega)$.

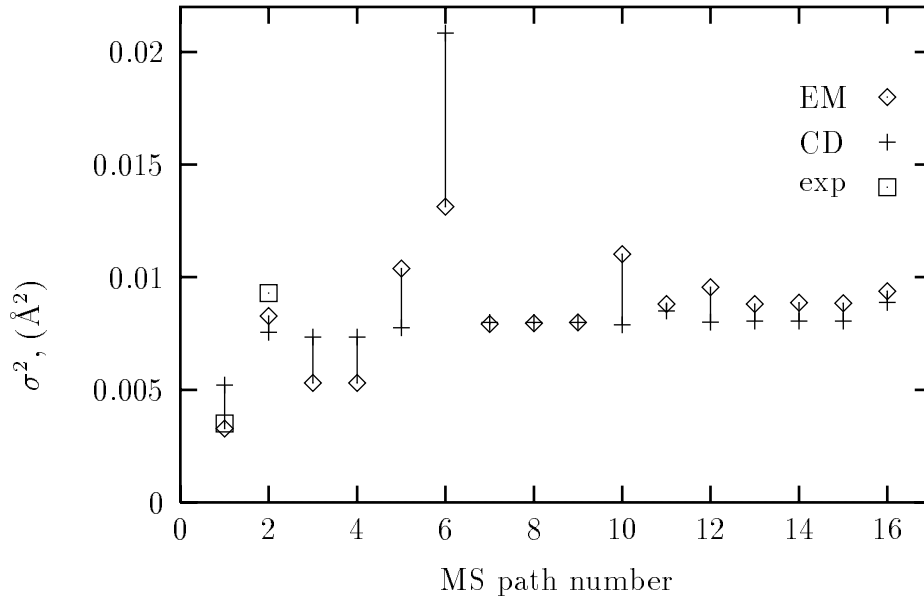


Figure 2.7: XAFS MS σ^2 for 147-atom cluster of Ge as calculated with the EM and CD models at $T = 300$ K vs MS path index (see text). Two experimental values [2], corresponding to the first and second shell SS, are given for comparison.

optical peaks at about 50 THz whereas the VDOS for path 2 has a more smeared out spectrum and, thus, is probably better approximated with CD model. This explains a smaller difference with CD model for path 2. The deficiency of the CD model for Ge is illustrated by the poor fit of the theoretical $\chi(R)$ to experimental XAFS spectra (see Fig. 2.8).

Using the same fitting parameters as in the case of Cu above, the 300 K data was fitted in R -space in the range between 2.0 and 5.2 \AA for the 20 most significant scattering paths spanning the first five shells. The fitted value for θ_D was 375 ± 16 K, which again is within error bars from the value 360 K [22].

2.5.3 Zn-tetraimidazole

The study of the vibrational and dynamical properties of complex organic structures such as zinc tetraimidazole is complicated by a large number of degrees of freedom and

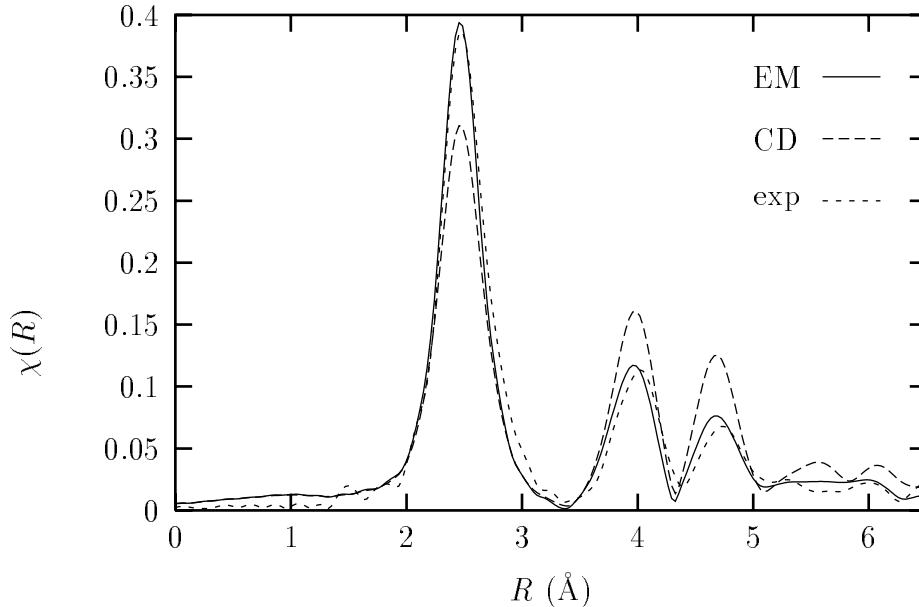


Figure 2.8: Magnitude of the phase corrected Fourier transform $\tilde{\chi}(R) = \text{FT}[k\chi(k)]$ for Ge at $T = 300$ K as extracted from experiment using the phase-corrected FEFFIT code (solid line) and fitted using theoretical results with the DW factors calculated via the CD (long dashes) and EM (short dashes) models.

a corresponding number of force constants. Imidazole is a crucial organic compound occurring in nucleic acid bases and amino acids, e.g. is an important constituent of the amino acid histidine. We chose zinc tetraimidazole since it was studied in detail by Loeffen, Pettifer and Tomkinson [4] (LPT) and thus permits quantitative comparisons. This macromolecule consists of four imidazole ring molecules ($\text{N}_2\text{C}_3\text{H}_4$) attached to a zinc atom forming a slightly distorted tetrahedral structure (Fig. 2.9). The entire cluster has C_2 point symmetry group with zinc atom lying on a two-fold axis and includes 37 atoms. To obtain all the parameters describing the force field of such complex materials is rarely possible and, therefore it is crucial for XAFS analysis to have a simplified prescription for calculating DW factors using a minimum set of parameters.

As a basis for the EM calculations we started with the full harmonic force field

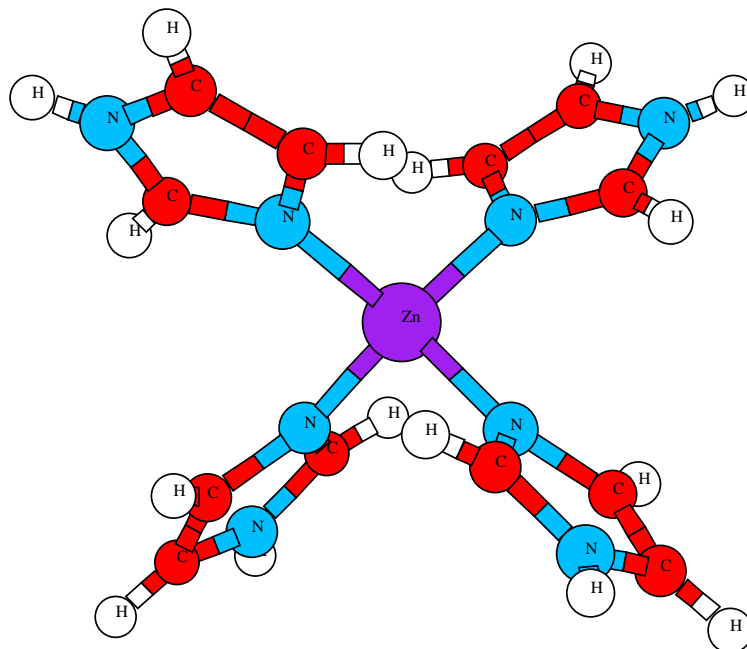


Figure 2.9: Structure of the 37-atom zinc tetraimidazole macromolecule based on the coordinates given by LPT [4].

deduced from inelastic neutron scattering of natural and deuterated zinc tetraimidazole compounds [4]. This force field is essentially a VFF with deformations described in terms of combinations of internal coordinates such as bond stretches, angle bends and torsions, and contains more than 60 distinct force constants, 40 of which correspond to internal vibrations of the imidazole branches. As may be guessed from the geometry of the structure, these internal modes as well as the “flapping” modes of the branches, have little effect on the radial vibrations of the Zn–N bonds that dominate σ_1^2 . Thus, by simplifying VFF of the imidazole units, the number of the parameters used in the calculations can be significantly reduced without causing large errors in σ_1^2 . Because torsional force constants are two orders of magnitude smaller than the dominant stretches, we neglected their effects in our simulations altogether. Several other negligibly small force constants were omitted as well. Our study consists of

Table 2.3: Force constants used in our VFF models 1–2 for σ_j^2 calculation in zinc tetraimidazole. Here \tilde{N} and \tilde{C} are pseudo-atoms (see text). All angle bends are scaled by corresponding near-neighbor distances.

Symbol	Description	Value (N/m)
k_0	Zn– \tilde{N} stretch	110
θ_0	\tilde{N} –Zn– \tilde{N} bend	37
k_1	N– \tilde{C} stretch	626
θ_1	\tilde{C} –N– \tilde{C} bend	2590

three steps in building the model structure analogous to that of LPT. Starting with a simple five-atom cluster, we then gradually add more degrees of freedom. At the first two steps, averages of the several similar force constants were used rather than their slightly different fitted values, which further reduced the number of the parameters. We refer the reader to the paper by LPT for detailed definitions of the internal coordinates (i.e. bonds and angles). The numerical implementation of our method was successfully checked by comparing EM calculations of frequency modes with those calculated analytically by applying a group theoretic analysis to a tetrahedral XY_4 model with three force constants: bond stretching, angle bending and bond coupling.

1) As a starting model (Fig. 2.10a) we considered a five-atom cluster consisting of a zinc atom in the center surrounded by four pseudo-atoms \tilde{N} with masses equal to the mass of the imidazole ring (68. u). The geometry of the cluster was kept the same as in the ZnN_4 group of the original structure. Only two force constants were used in the calculation: a bond-stretching k_0 (degeneracy 4) and an angle bending θ_0 (degeneracy 6) (see Table 2.3). The first parameter was set equal to the average of the two Zn–N stretches in the full VFF of LPT, and the latter to the average of the four N–Zn–N angle bends (taking into account degeneracy due to the symmetry). The model yielded SS $\sigma_1^2 = 2.06 \times 10^{-3} \text{ \AA}^2$ at 20 K, about 18% below the value

Table 2.4: Force constants used in the VFF 3 for σ_j^2 calculation in zinc tetraimidazole.
All angle bends are scaled by corresponding near-neighbor distances.

Symbol	Description	Value (N/m)
$k_0^{(A)}$	Zn–N stretch	111
$k_0^{(B)}$	Zn–N stretch	108
α	Zn–N/Zn–N	27.4
β	Zn–N/Zn–N	3.77
θ_{01}	N–Zn–N bend	46.1
θ_{02}	N–Zn–N bend	26.1
θ_{03}	N–Zn–N bend	40.9
θ_{04}	N–Zn–N bend	21.8
ϕ_{11}	imid out – of – plane bend	9.0
ϕ_{12}	imid out – of – plane bend	7.3
k_{11}	N ₁ –C ₂ stretch	670
k_{12}	N ₁ –C ₅ stretch	681
k_{13}	C ₄ =C ₅ stretch	561
k_{14}	N ₃ –C ₄ stretch	500
k_{15}	N ₃ =C ₂ stretch	752
γ_1	N ₁ –C ₂ /N ₁ –C ₅	47.3
γ_2	N ₁ –C ₅ /C ₄ =C ₅	45.0
γ_3	C ₄ =C ₅ /N ₃ –C ₄	25.4
γ_4	N ₃ –C ₄ /N ₃ =C ₂	81.1
θ_{11}	Zn–N–C bend	10.9
θ_{12}	Zn–N–C bend	14.8
ζ_A	ring deformation	260
ξ_B	ring deformation	250

estimated from experimental XAFS data $(2.5 \pm 0.2) \times 10^{-3} \text{ \AA}^2$.

2) In the second, slightly bigger calculation, we included the ZnN_4 group and 8 pseudo-atoms in place of the carbon atoms nearest to the nitrogens (see Fig. 2.10b). Four of these pseudo-atoms (\tilde{C}_1) had masses equal to the sum $M(\text{C}) + M(\text{N}) + 2M(\text{H}) \simeq 28$. u and the other four (\tilde{C}_2) to $2 \cdot (M(\text{C}) + M(\text{H})) \simeq 26$. u. Four force constants were used in the calculation (see Table 2.3): in addition to the 2 parameters of model 1) we considered a stretch k_1 between the nitrogen and the nearest to it \tilde{C}_i equal to the average of the two N–C stretches and an angle bending θ_1 (the result of the combining two ring deformations and calculating coefficients at the corresponding angle bend term). For the short Zn–N bond the resulting $\sigma_1^2 = 2.43 \times 10^{-3} \text{ \AA}^2$ at 20 K.

3) Finally, we included all atoms of the imidazole units except the hydrogens (see Fig. 2.10c) and used 23 distinct force constants in the VFF model: two Zn–N bond-stretches $k_0^{(A)}$ and $k_0^{(B)}$, two Zn–N bond-coupling α and β , six skeletal angle bends θ_{0i} , two out-of-plane angle bends of the imidazole branches ϕ_{1i} , five bond-stretches inside the imidazole rings k_{1i} , four imidazole bond-coupling γ_i and two ring-deformation constants ζ_A and ξ_B (see Table 2.4). The result for the weaker (108 N/m) Zn–N bond is $\sigma_1^2(20\text{K}) = 2.64 \times 10^{-3} \text{ \AA}^2$, in good agreement with the value obtained by LPT ($2.62 \times 10^{-3} \text{ \AA}^2$). For the stronger (111 N/m) bond the EM calculation yielded $2.63 \times 10^{-3} \text{ \AA}^2$, again in excellent agreement with the values calculated by LPT ($2.60 \times 10^{-3} \text{ \AA}^2$).

We also used these three models to calculate $\sigma_j^2(20\text{K})$ for four MS triangular paths of the type $\text{Zn} \rightarrow \text{N}^{(1)} \rightarrow \text{N}^{(2)} \rightarrow \text{Zn}$ where $\text{N}^{(1)}$ and $\text{N}^{(2)}$ are the nearest neighbors to the scattering center (see Table 2.5). Note a significant effect of the $\text{N}^{(1)} - \text{Zn} - \text{N}^{(2)}$ bending force constants and geometry on the σ_j^2 values. The wider the angle, the greater resistance to its deformation, and hence these σ_j^2 's are inversely proportional to φ_j . The values of σ_j^2 appear to be rather large since there is no explicit N–N stretching involved.

These results (Table 2.6) show that, due to the local nature of σ^2 , it is possible

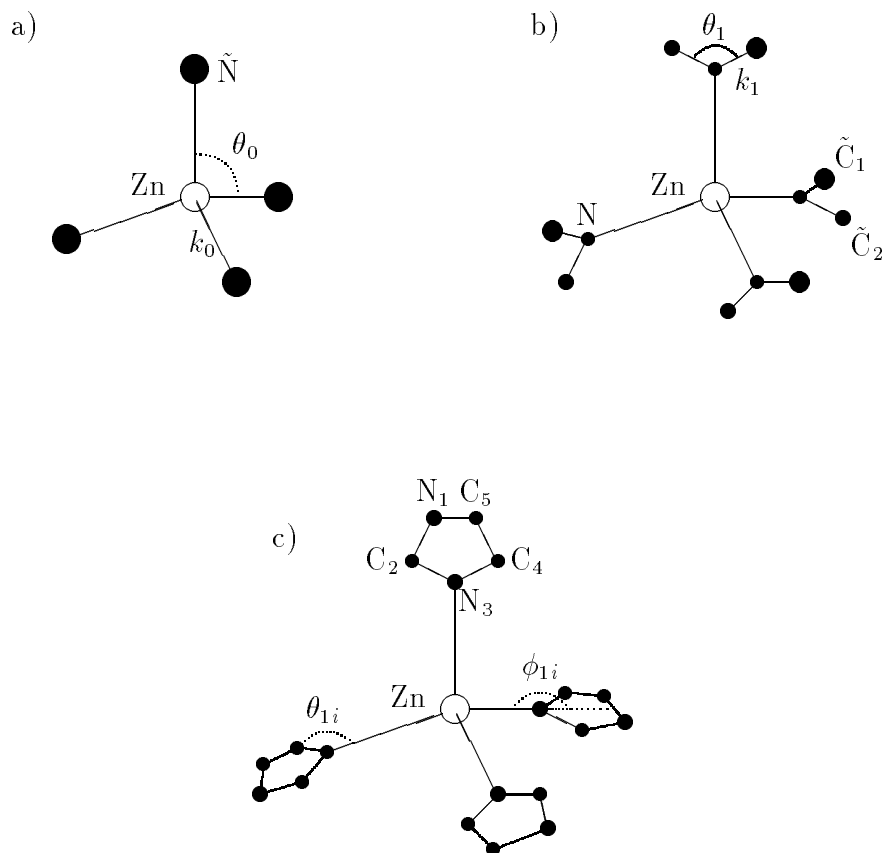


Figure 2.10: Reduced structural models used to approximate the VFF of zinc tetraimidazole with a) two and b) four effective force constants, as well as c) the 23-parameter VFF.

Table 2.5: Values of MS σ_j^2 at 20 K calculated for four central MS paths of the type $\text{Zn} \xrightarrow{k^{(1)}} \text{N}^{(1)} \xrightarrow{\theta} \text{N}^{(2)} \xrightarrow{k^{(2)}} \text{Zn}$ in zinc tetraimidazole depending on the number of the force constants (ν) used in the VFF model. Here j is the MS path index, R_j its effective length, φ_j the scattering angle $\text{N}^{(1)} - \text{Zn} - \text{N}^{(2)}$ in degrees, $k^{(i)}$ the force constant for the bond $\text{Zn} - \text{N}^{(i)}$ and θ is the bending force constant for the corresponding φ_j . All force constants are given in N/m.

j	R_j (Å)	φ_j	σ_j^2 (10^{-3} Å ²)			$k^{(1)}$	$k^{(2)}$	θ
			$\nu = 2$	4	23			
19	3.57	107	3.17	4.10	3.94	108	111	40.9
20	3.59	108	3.17	4.71	4.95	111	111	26.1
21	3.62	111	3.16	4.05	3.86	108	111	46.1
22	3.63	112	3.15	4.47	4.87	108	108	21.8

Table 2.6: Values of SS σ_1^2 at 20 K for the weak Zn–N bond in zinc tetraimidazole depending on the number of the force constants (ν) used in the VFF model. Here $\epsilon_{exp} = 100(\sigma_1^2 - \sigma_{exp}^2)/\sigma_{exp}^2$ and $\epsilon = 100(\sigma_1^2 - \sigma_{LPT}^2)/\sigma_{LPT}^2$ with $\sigma_{exp}^2 = (2.5 \pm 0.2) \times 10^{-3}$ Å² and $\sigma_{LPT}^2 = 2.62 \times 10^{-3}$ Å².

ν	σ_1^2 (10^{-3} Å ²)	ϵ_{exp} (%)	ϵ (%)
2	2.06	18	21
4	2.43	3	7
23	2.64	6	1

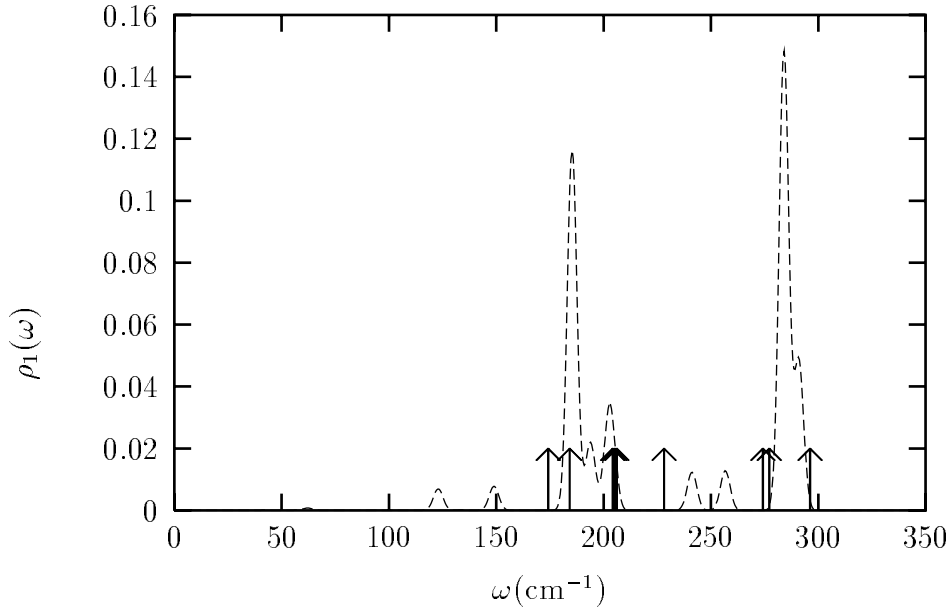


Figure 2.11: Low frequency part of the first shell projected VDOS $\rho_R(\omega)$ for the 23-parameter model of Zn-tetraimidazole ($N = 21$). The lines at 296, 277, 274, 228, 206, 205, 204, 184 and 174 cm^{-1} indicate low frequency tetrahedral modes obtained by LPT [4] for the entire 37-atom macromolecule.

to reduce dramatically the number of the parameters in the VFF even for very complex structures while still attaining a 5–10% accuracy in the final results for σ^2 in comparison with both more precise theory and experimental data. This accuracy is satisfactory, since the error bars for the force constants themselves are usually of the same order, e.g. about 15% for Zn–N bond-stretching constants in zinc tetraimidazole, and the accuracy of the EM method, as implemented in our code, is fixed to be about 5%.

The vibrational spectrum of the zinc tetraimidazole molecule can be subdivided into high and low frequency regimes. The high frequency regime ($> 500\text{cm}^{-1}$) corresponds to the modes caused by internal motion of the imidazole branches, while the low frequency regime ($< 500\text{cm}^{-1}$) consists of skeletal vibrational modes such as tetrahedral deformations, and in- and out-of-plane librations of the imidazole branches.

These low frequency modes yield almost 70% of the calculated σ_1^2 . The low frequency part of the projected VDOS for Zn–N bond (first shell) is presented in Fig. 2.11. The peaks lying in the range between 170 cm^{-1} and 300 cm^{-1} correspond to the tetrahedral modes, whereas the lower part of the spectrum is due to the librations of the imidazole branches. Due to the small size of the system the spectra is highly discrete. For such heterogeneous materials like zinc tetraimidazole, a single parameter CD or CE model is not accurate.

2.5.4 *Semiempirical dynamical matrix calculation*

We used AM1 (Austin model 1) [69] method in MNDO94 code which is part of the UniChem package to optimize geometry configuration of zinc tetraimidazole molecule and to calculate cartesian dynamical matrix for this geometry. AM1 is a parametric quantum mechanical molecular model based on the NDDO approximation [69]. The resulting optimized geometry (see Table 2.7) is in a good agreement with the experiment: bond lengths are within 4% of their experimental values and angles are within 3%. The dynamical matrix was then used in EM calculations to obtain values of σ^2 . These values appear to be in good agreement with ones obtained using the VFF of Loeffen *et al.* [4] (see Table 2.8).

Table 2.7: Values of selected bonds and angles in zinc tetraimidazole obtained from AM1 geometry optimization in comparison with experimental values given by Loeffen *et al.* [4]. All bonds are in units of Å, angles are in degrees.

bonds and angles	AM1	experiment
Zn – N ₂	2.0626	1.9835
Zn – N ₇	2.0629	1.9832
Zn – N ₁₃	2.0635	1.9835
Zn – N ₁₇	2.0625	1.9832
N ₂ – Zn – N ₇	109.60	111.53
N ₂ – Zn – N ₁₃	108.97	108.01
N ₂ – Zn – N ₁₇	109.88	106.66
N ₇ – Zn – N ₁₃	109.79	106.66
N ₂ – C ₃	1.3656	1.3256
N ₂ – C ₆	1.4014	1.3838
C ₂ – N ₄	1.3852	1.3366
N ₄ – C ₅	1.3960	1.3710
C ₅ – C ₆	1.4062	1.3485

Table 2.8: Values of MS σ_j^2 (10^{-3} \AA^2) at 20 K and 300 K calculated for several MS paths in zinc tetraimidazole based on AM1 dynamical matrix in comparison with values obtained by Loeffen *et al.* [4].

path description	σ_j^2 (20K)		σ_j^2 (300K)	
	AM1	Loeffen	AM1	Loeffen
experiment	2.5 ± 0.2			
Zn – N ₁₃ – Zn	2.51	2.62	3.92	4.29
Zn – N ₂ – Zn	2.51	2.62	3.93	4.29
Zn – N ₇ – Zn	2.51	2.60	3.92	4.25
Zn – N ₁₇ – Zn	2.51	2.60	3.91	4.25
Zn – C ₆ – Zn	4.36	4.23	10.25	8.82
Zn – C ₁₁ – Zn	4.36	4.23	10.24	8.82
Zn – C ₁₄ – Zn	4.37	4.23	10.29	8.82
Zn – C ₂₁ – Zn	4.36	4.23	10.26	8.82
Zn – C ₃ – Zn	4.03	3.99	8.99	8.37
Zn – C ₈ – Zn	4.02	3.99	8.99	8.37
Zn – C ₁₂ – Zn	4.03	4.01	9.01	8.57
Zn – C ₁₈ – Zn	4.03	4.01	9.01	8.57
Zn – N ₂ – N ₄ – N ₂ – Zn	3.09	2.83	5.04	4.93
Zn – N ₂ – C ₅ – Zn	3.23	3.20	5.47	5.66
Zn – N ₁₃ – C ₁₅ – Zn	3.24	3.15	5.48	5.46
Zn – C ₃ – N ₄ – N ₂ – Zn	3.17	3.40	5.83	6.34
Zn – C ₁₂ – N ₁₆ – N ₁₃ – Zn	3.17	3.12	5.84	5.72

Chapter 3

RECURSION METHOD

The traditional single frequency CE approximation does not differentiate between acoustic and optical modes and can lead to poor agreement with experimental data. Here we present an improvement to the traditional CE model by using the recursion, or Lanczos, method (RM) [25, 70] and a set of local force constants. Instead of calculating the entire projected VDOS as in the EM approach, the RM calculations are based on a double δ -function representation and, thus, are much faster. We discuss our results in comparison with the CE and EM calculations.

3.1 Formalism

The RM is a technique for determining local physical behavior by successive approximations which involve more and more of a given system. We are interested in the projected density $\rho_j(\omega)$, but it is more convenient to deal with the distribution with respect to $\omega^2 = x$,

$$g_j(x) \equiv \langle Q_j | \delta(x - D) | Q_j \rangle = \frac{\rho_j(\omega)}{2\omega}. \quad (3.1)$$

Here again (see Chap. 2) $D_{\alpha,\beta}(l, m) = \Phi_{\alpha,\beta}(l, m) / \sqrt{M_l M_m}$ is $3N \times 3N$ dynamical matrix with $\Phi_{l\alpha, m\beta}$ denoting the second derivatives of the potential energy V of the lattice deformation with respect to the atomic displacements $u_{l\alpha}$ and $u_{m\beta}$ taken in the equilibrium configuration, and $|Q_j\rangle$ is the normalized initial displacement state for MS path j defined in Eq. 2.10. If only the central interaction between the nearest neighbors is taken into account, then $V = 1/2 \sum k_{lm} (\delta r_{lm})^2$ for bond stretches $\delta r_{lm} =$

$(\vec{u}_l - \vec{u}_m) \cdot \hat{R}_{lm}$ and the matrix of the second derivatives can be written in the form

$$\Phi_{\alpha,\beta}(l, m) = \sum_{i=1}^{N_m} k_{im} \hat{R}_{im}^\alpha \hat{R}_{im}^\beta \delta_{lm} - k_{lm} \hat{R}_{lm}^\alpha \hat{R}_{lm}^\beta, \quad (3.2)$$

where k_{lm} is a bond-stretching force constant for nearest neighbors l and m , N_m is a number of the nearest neighbors of atom m , and \hat{R}_{lm}^α is the α th cartesian component of the directing unit vector between atoms l and m .

The RM yields a continued fraction representation of $g_j(x)$, i.e.

$$g_j(x) = -\frac{1}{\pi} \text{Im} \frac{1}{x - a_0 - \frac{b_0}{x - a_1 - \frac{b_1}{x - a_2 - \dots}}} \quad (3.3)$$

in which $\text{Im } x \rightarrow 0^+$. The coefficients a_n and b_n determine a 3-term recursion relation which defines new orthogonal basis states $|n\rangle$,

$$\begin{aligned} |n+1\rangle &= (D - a_n)|n\rangle - b_{n-1}|n-1\rangle, \\ |0\rangle &\equiv |Q_j\rangle, \quad |-1\rangle \equiv 0. \end{aligned} \quad (3.4)$$

One can picture these states roughly as “shell states” since their largest components are typically on the n th shell of neighbors to the atoms in the path. If one truncates the fraction after N tiers, the continued fraction can be unfolded as an $[N/N+1]$ Padé approximate, $Q_N(x)/P_{N+1}(x)$, the polynomials in which may be generated by recurrence relations similar to Eq. (3.4). Taking the imaginary part then yields an N -point δ -function representation,

$$\rho_j(\omega) \approx \sum_{i=1}^N w_i \delta(\omega - x_i^{1/2}), \quad (3.5)$$

where w_i and x_i are respectively residues and poles of $Q_N(x)/P_{N+1}(x)$. This approximant yields exactly the leading $2N$ power moments m_n of the spectrum $g_j(x)$, and also gives an N -point Gaussian quadrature formula for σ_j^2 ,

$$\sigma_j^2(T) = \frac{\hbar}{2\mu_j} \sum_{i=1}^N \frac{w_i}{x_i^{1/2}} \coth \frac{\beta \hbar x_i^{1/2}}{2}. \quad (3.6)$$

Clearly, the result for a single tier is $g_j(x) = 1/(1 - a_0)$ which corresponds to the traditional CE approximation with $\omega_E^2 \equiv a_0 = \langle Q_j | D | Q_j \rangle$ which is equal to the second moment m_2 .

In the present study we limit the continued fraction to the second tier. Thus, the vibrational spectrum is approximated with two δ -functions centered at the effective frequencies $\omega_{1,2} = \sqrt{x_{1,2}}$ with the corresponding weight factors $w_1 = (a_1 - x_2)/(x_1 - x_2)$ and $w_2 = (x_1 - a_1)/(x_1 - x_2)$, where

$$x_{1,2} = \frac{1}{2} \left[a_0 + a_1 \pm \sqrt{(a_0 - a_1)^2 + 4b_0} \right]. \quad (3.7)$$

In this, case the lowest frequency represents an effective acoustic mode whereas the highest one corresponds to an effective optical mode.

3.2 Calculations and results in Cu

The model structure used in the calculation is a 225-atom cluster (11 shells, $R_{\max} = 8.47 \text{ \AA}$) of fcc Cu crystal without periodic boundary conditions. Following the model of Rehr and Alben [24], only a single central interaction between the first nearest neighbors with force constant $k = 27.9 \text{ N/m}$ was taken into account. The MS σ_j^2 at 295 K calculated using the RM in comparison with results obtained from the EM method and a single frequency CE model with ω_E based on the second moment of the dynamical matrix are presented in Fig. 3.1 versus scattering paths index j listed in order of increasing path length as generated by FEFF7 (also see Table 3.1). For example, path number 1 corresponds to first shell single scattering (SS), 2 to second shell SS, 3 to 111 triangular MS path, 4 to triangular 211 MS path, 5 to third shell SS, 12 to double scattering from the first neighbor ($\sigma_{12}^2 = 4\sigma_1^2$) etc.

Table 3.1: Values of MS $\sigma_j^2 \times 10^{-3} \text{ \AA}^2$ at 295 K for a 225-atom cluster of Cu as calculated with a single force constant ($k = 27.9 \text{ N/m}$) model using RM (σ_{RM}^2) and CE (σ_{CE}^2) approximation vs MS path index j . Two experimental values [2] corresponding to the first and second shell SS are given for comparison. Also, given are Einstein frequencies ω_E , effective frequencies $\omega_{1,2}$ (all in THz), and the corresponding weight factors $w_{1,2}$ (dimensionless).

j	σ_{RM}^2	σ_{CE}^2	σ_{exp}^2	ω_E	ω_1	ω_2	w_1	w_2
1	7.34	6.26	7.93	36.4	27.5	41.9	0.434	0.566
2	9.67	7.72	11.08	32.5	24.9	41.2	0.592	0.408
3	7.26	6.45		38.1	28.9	42.2	0.349	0.651
4	8.76	7.22		35.5	26.3	41.7	0.458	0.542
5	9.39	7.72		32.5	25.0	39.8	0.550	0.450

The σ_j^2 calculated via the RM appear to be within about 9% of the corresponding EM values which are in a good agreement with experiment (2.7% for the 1st shell and 4.4% for the 2nd), whereas the CE values are typically 15-27% off in comparison with EM. These results indicate that the RM provides a much better agreement with the EM method and experiment than the CE model for all MS paths.

Typically, the RM somewhat underestimates the σ^2 values for Cu due to insufficient weight at the lower part of the spectrum. In cases when VDOS contains low frequency acoustic modes, in order to account for these modes it is sufficient to add a factor of 9/8 to the weight of the lowest effective frequency. This factor is calculated in such a way that it weights low frequency modes as they would be in the CD model. For example, in case of Cu at 295 K this correction brings σ_1^2 and σ_2^2 up to 7.91 and $10.62 \times 10^{-3} \text{ \AA}^2$, in much closer agreement with EM method and experiment.

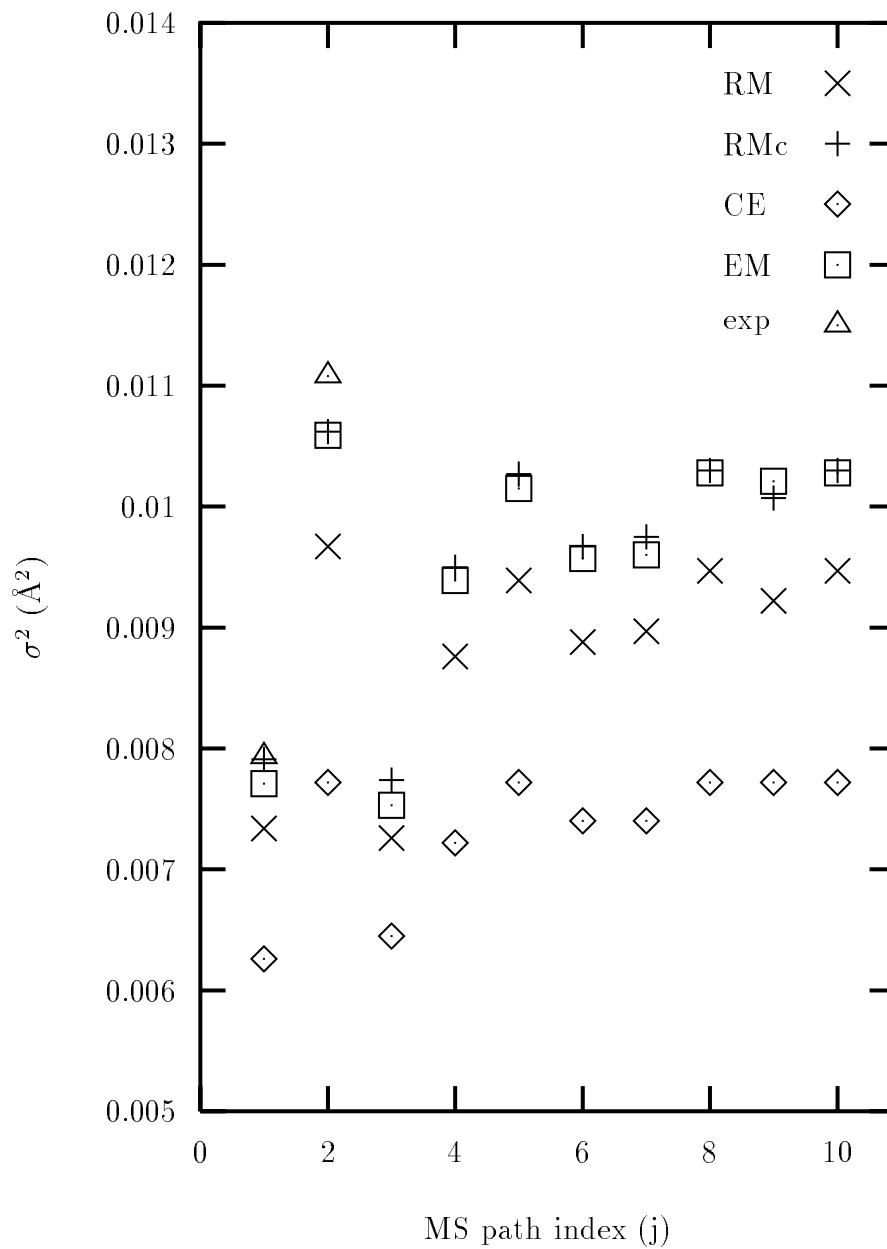


Figure 3.1: MS XAFS σ_j^2 for Cu at 295 K as calculated with a single force constant ($k = 27.9$ N/m) with RM, RM corrected with the 9/8 factor (RMc), EM and CE methods vs MS path index. Two experimental values [2] corresponding to the first and second shell SS are given for comparison.

Chapter 4

XANES AND XAFS CALCULATIONS IN ORGANOMETALLIC SYSTEMS

Fitting values of σ^2 to experiment in organic and organometallic systems is usually complicated because of a large number of fitting parameters and a small number of independent points in these systems. Also, the traditional isotropic models, such as the CD and CE models, do not work very well for such highly inhomogeneous materials as biological molecules. In this case, the EM method is a valuable alternative.

In the present chapter we consider XANES and XAFS calculations in the organometallic systems tetramethylammonium tetrachloroferrate (II) and *Pyrococcus Furi-ous* rubredoxin. XAFS DW factors for these compounds were calculated using the EM method with force constants calculated *ab initio* for the first material and fitted to experimental vibrational spectra for the second.

4.1 *Ab initio* calculation of the DW factors in tetrachloroferrate (II)

4.1.1 Force constant matrix for an XY_4 molecule

The XY_4 molecular model [37] consists of five atoms with the central atom X surrounded by four tetrahedrally oriented atoms Y (see Fig. 2.10a for an example). All compounds considered in this dissertation can be approximated with an XY_4 model.

Cartesian force constant matrix Φ is the matrix of the second derivatives of the potential energy of the lattice deformations with respect to atomic displacements in cartesian coordinates. To better understand the nature of a molecular FF characterized by Φ , it is helpful to rewrite this matrix in terms of internal coordinates S_t such

as bond lengths r_{ij} and bond angles θ_{ijk} , so that its matrix elements are comprised of the local force constants. It is traditional [37] to define ten internal coordinates for tetrahedral molecules of the type XY_4 . For example, in a molecule of tetrachloroferrate (TCF) FeCl_4^{-2} (see Fig. 4.3), these include four bond stretches between the central Fe_1 atom and a Cl atom, $S_t = \delta r_{1t}$ where $t = 2, \dots, 5$, and six $\text{Cl}_i - \text{Fe}_1 - \text{Cl}_j$ angle bends, where $i, j = 2, \dots, 5$. Out of these six angle bends only five are independent, since the condition $\sum_{ij} \theta_{ij} = 0$ has to be satisfied. Thus we have nine independent internal coordinates which correspond to the nine ($3N - 6$ with $N = 5$) degrees of freedom.

We will define a 10×15 transformation matrix B which transforms a 15-dimensional cartesian displacement vector $\delta \vec{\xi} = (u_{1x}, u_{1y}, \dots, u_{5z})$ into a 10-dimensional vector of the corresponding changes in the internal coordinates, $\delta \vec{S}$,

$$\delta \vec{S} = B \cdot \delta \vec{\xi}. \quad (4.1)$$

Thus, the force constant matrix in terms of the internal coordinates Φ_{int} is related to Φ by the matrix transformation

$$\Phi_{int} = (B^{-1})^T \cdot \Phi \cdot B^{-1}, \quad (4.2)$$

where the resulting Φ_{int} is a symmetric 10×10 matrix. For example, if only the central interaction between the nearest neighbors is taken into account, the cartesian force constant matrix elements can be written as in Eq. 3.2. Thus, in this case the elements of the B matrix consist of the directing cosines $\pm \hat{R}_{lm}^\alpha$ and the matrix elements of Φ_{int} are simply the bond stretching force constants k_{lm} (Table 4.1).

Similarly, potential energy arising due to changes in bond angles,

$$\delta \theta_{ijk} = \vec{s}_{ti} \cdot \vec{u}_i + \vec{s}_{tj} \cdot \vec{u}_j + \vec{s}_{tk} \cdot \vec{u}_k, \quad (4.3)$$

where

Table 4.1: Matrix B for an XY_4 molecule.

$t \setminus \xi_i$	x_1	y_1	z_1	x_2	y_2	z_2	x_3	y_3	z_3	x_4	y_4	z_4	x_5	y_5	z_5
r_{12}	\hat{R}_{12}^x	\hat{R}_{12}^y	\hat{R}_{12}^z	$-\hat{R}_{12}^x$	$-\hat{R}_{12}^y$	$-\hat{R}_{12}^z$	0	0	0	0	0	0	0	0	0
r_{13}	\hat{R}_{13}^x	\hat{R}_{13}^y	\hat{R}_{13}^z	0	0	0	$-\hat{R}_{13}^x$	$-\hat{R}_{13}^y$	$-\hat{R}_{13}^z$	0	0	0	0	0	0
r_{14}	\hat{R}_{14}^x	\hat{R}_{14}^y	\hat{R}_{14}^z	0	0	0	0	0	0	$-\hat{R}_{14}^x$	$-\hat{R}_{14}^y$	$-\hat{R}_{14}^z$	0	0	0
r_{15}	\hat{R}_{15}^x	\hat{R}_{15}^y	\hat{R}_{15}^z	0	0	0	0	0	0	0	0	0	$-\hat{R}_{15}^x$	$-\hat{R}_{15}^y$	$-\hat{R}_{15}^z$
θ_{213}	s_{11}^x	s_{11}^y	s_{11}^z	s_{12}^x	s_{12}^y	s_{12}^z	s_{13}^x	s_{13}^y	s_{13}^z	0	0	0	0	0	0
θ_{214}	s_{21}^x	s_{21}^y	s_{21}^z	s_{22}^x	s_{22}^y	s_{22}^z	0	0	0	s_{24}^x	s_{24}^y	s_{24}^z	0	0	0
θ_{215}	s_{31}^x	s_{31}^y	s_{31}^z	s_{32}^x	s_{32}^y	s_{32}^z	0	0	0	0	0	0	s_{35}^x	s_{35}^y	s_{35}^z
θ_{314}	s_{41}^x	s_{41}^y	s_{41}^z	0	0	0	s_{43}^x	s_{43}^y	s_{43}^z	s_{44}^x	s_{44}^y	s_{44}^z	0	0	0
θ_{315}	s_{51}^x	s_{51}^y	s_{51}^z	0	0	0	s_{53}^x	s_{53}^y	s_{53}^z	0	0	0	s_{55}^x	s_{55}^y	s_{55}^z
θ_{415}	s_{61}^x	s_{61}^y	s_{61}^z	0	0	0	0	0	0	s_{64}^x	s_{64}^y	s_{64}^z	s_{65}^x	s_{65}^y	s_{65}^z

$$\vec{s}_{ti} = \frac{\hat{R}_{ji} \cos \theta_{ijk} - \hat{R}_{jk}}{r_{ji} \sin \theta_{ijk}}, \quad (4.4)$$

$$\vec{s}_{tj} = \frac{(r_{ji} - r_{jk} \cos \theta_{ijk}) \hat{R}_{ji} + (r_{jk} - r_{ji} \cos \theta_{ijk}) \hat{R}_{jk}}{r_{ji} r_{jk} \sin \theta_{ijk}}, \quad (4.5)$$

$$\vec{s}_{tk} = \frac{\hat{R}_{jk} \cos \theta_{ijk} - \hat{R}_{ji}}{r_{jk} \sin \theta_{ijk}} \quad (4.6)$$

[27], is equal to $V_{ang} = 1/2 \sum \kappa_{ijk} (\delta\theta_{ijk})^2$. This leads to the force constant matrix elements in the following form

$$\Phi_{\alpha,\beta}^{ang}(l, m) = \sum_t \kappa_t s_{tl}^\alpha s_{tm}^\beta \delta_{tl} \delta_{tm}, \quad (4.7)$$

where the sum runs over all bond angles, index t is equivalent to the corresponding set of the three atomic indices $\{i, j, k\}$, $\kappa_t \equiv k_\theta^{ijk}$, and δ_{tl} is equal to 1 if at least one index from the set is equal to l and to 0 otherwise. Therefore, in this case vector components s_{tl}^α are the matrix elements of B and the angle bending force constants κ_t are those of Φ_{int} (Table 4.1).

Because six cartesian displacements and one internal coordinate are redundant, B is singular and therefore, singular value decomposition [71] (SVD) technique has to be adopted in order to find its inverse. In our study we developed a simple code B_REV based on the subroutine SVDCMP [71] to calculate Φ_{int} for an XY_4 type molecule via Eq. 4.2. This code takes as matrices Φ and B as an input and returns matrix Φ_{int} as an output.

4.1.2 Geometry optimization, VDOS and σ^2

A model structure used in the *ab initio* DGauss calculation was a 5-atom high-spin (multiplicity 5) anion of TCF (II), FeCl_4^{-2} , which has a slightly distorted tetrahedral symmetry. Two independent runs using different approaches in the SCF calculations, one based on the LDA with VWN80 form of the exchange-correlation functional and

Table 4.2: Definitions and values of the internal coordinates S_t used in the study: the bond lengths (\AA) and the bond angles (deg). The values are given for the LDA and GGA optimized structures.

t	S_t	LDA	GGA
1	$\text{Fe}_1 - \text{Cl}_2$	2.305	2.379
2	$\text{Fe}_1 - \text{Cl}_3$	2.304	2.375
3	$\text{Fe}_1 - \text{Cl}_4$	2.302	2.371
4	$\text{Fe}_1 - \text{Cl}_5$	2.304	2.375
5	$\text{Cl}_2 - \text{Fe}_1 - \text{Cl}_3$	105.37	110.36
6	$\text{Cl}_2 - \text{Fe}_1 - \text{Cl}_4$	118.78	111.91
7	$\text{Cl}_2 - \text{Fe}_1 - \text{Cl}_5$	105.37	105.85
8	$\text{Cl}_3 - \text{Fe}_1 - \text{Cl}_4$	105.10	106.22
9	$\text{Cl}_3 - \text{Fe}_1 - \text{Cl}_5$	117.85	112.11
10	$\text{Cl}_4 - \text{Fe}_1 - \text{Cl}_5$	105.10	110.49

the other on the GGA with PW91 form, were performed on the structure. The resulting values of the optimized bonds and angles are given in Table 4.2. The GGA bonds appear to be about 0.07 \AA longer than the corresponding LDA bonds which is a typical effect of the non-local corrections in transition metal systems of this type. Both approximations give structural results in good agreement with experiment (see Table 4.3). But since the LDA bond lengths for the anion are closer to their experimental values in the molecule of tetramethylammonium TCF (II) $[\text{N}(\text{CH}_3)_4]_2[\text{FeCl}_4]$ molecule [5], which is a focus of our XAFS analysis in the next section, we will use the LDA results in our study.

We also performed a trial LDA calculation for a low-spin (multiplicity 3) state of the FeCl_4^{-2} anion. The resulting LDA optimized configuration had two Fe–Cl bonds with lengths 2.2898 \AA , one bond with length 2.2872 \AA , and the shortest bond with

Table 4.3: Bond distances and angles in FeCl_4^- anion found in different studies and different compounds (see [5] for references).

Salt	Fe–Cl (Å)	Cl–Fe–Cl (deg)
$[\text{C}_5\text{H}_5\text{S}_2]_2[\text{FeCl}_4]$	[2] 2.289(5)	[1] 112
	[2] 2.335(5)	[1] 116
	(av) 2.313(4)	[2] 106
		[2] 108
$[\text{C}_5\text{H}_5\text{S}_2]_2[\text{FeCl}_4]$	[2] 2.31(1)	[1] 112
	[2] 2.34(1)	[1] 116
	(av) 2.33(2)	[2] 106
		[2] 108
$\{[\text{Fe}(\eta\text{-C}_5\text{H}_5)(\text{CO})_2]\text{SbCl}_2\}[\text{FeCl}_4]$	[2] 2.284(5)	[1] 104.2(3)
	[2] 2.320(5)	[1] 108.5(2)
	(av) 2.302(18)	[2] 107.2(2)
		[2] 115.0(2)
$[\text{N}(\text{CH}_3)_4]_2[\text{FeCl}_4]$	[2] 2.296(2)	[1] 113.6(1)
	[1] 2.290(2)	[1] 110.9(1)
	[1] 2.289(2)	[2] 108.2(1)
	(av) 2.292(2)	[2] 108.0(1)

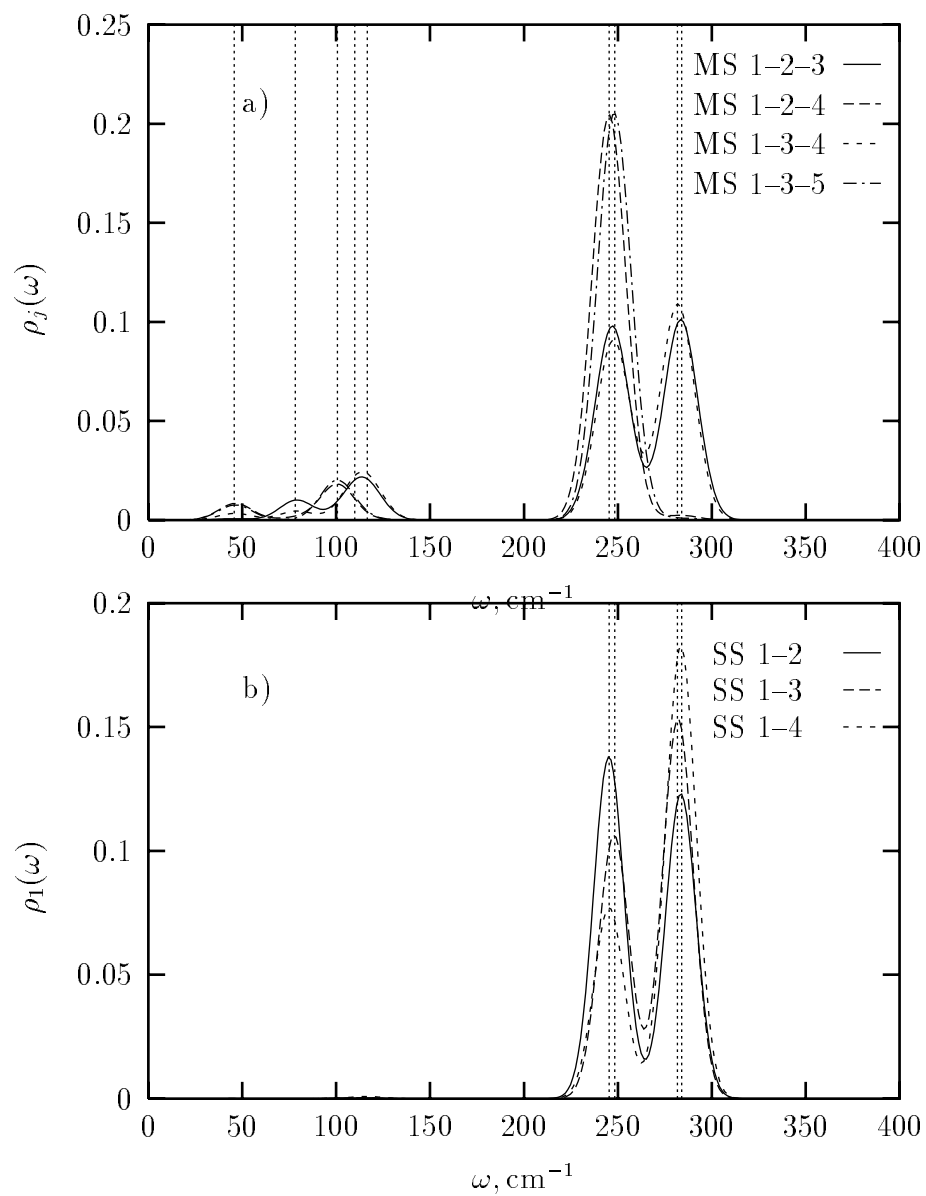


Figure 4.1: Projected VDOS for three distinct triangular MS (a) and SS (b) paths in FeCl_4^{2-} . The lines at 45.68, 78.23, 100.64, 109.89, 116.57, 245.34, 248.39, 281.77, and 284.02 cm^{-1} indicate the infrared vibrational modes calculated by DGauss.

Table 4.4: Matrix elements of Φ_{int} in units of $(10^2 \times \text{mdyn}\text{\AA}/[S_{t_1}]/[S_{t_2}])$ where $[S_{t_i}]$ is in \AA for bonds and in rad for angles.

t	1	2	3	4	5	6	7	8	9	10
1	92.57	12.90	7.61	12.57	-4.42	-2.25	-3.29	3.79	3.85	2.54
2	12.90	95.71	12.05	7.89	-2.88	3.72	3.06	-4.89	-1.81	2.91
3	7.61	12.06	96.25	12.66	2.34	-0.73	2.57	-3.43	2.94	-3.50
4	12.57	7.88	12.67	95.82	3.58	3.52	-3.08	2.62	-1.99	-4.57
5	-4.43	-2.87	2.36	3.58	25.69	-2.41	-2.73	-6.18	-2.25	-12.64
6	-2.25	3.71	-0.73	3.52	-2.45	15.78	-0.92	-0.15	-10.06	-1.91
7	-3.27	3.07	2.56	-3.08	-2.66	-0.97	23.26	-14.79	0.28	-5.27
8	3.74	-4.86	-3.42	2.63	-6.27	-0.18	-14.84	26.17	-0.82	-4.05
9	3.85	-1.83	2.94	-1.98	-2.24	-10.06	0.27	-0.88	17.51	-3.71
10	2.59	2.90	-3.52	-4.59	-12.59	-1.88	-5.18	-4.16	-3.78	27.17

2.2169 \AA . This result is consistent with the discussion of Lauher and Ibers [5] that bond lengths in this type of systems tend to increase for a higher spin state. A large distortion in the fourth bond can be attributed to a spontaneous symmetry breaking due to Jahn-Teller effect [72, 73].

Vibrational spectrum and cartesian 15×15 force constant matrix were then calculated for the LDA optimized structure. Since there are only nine degrees of freedom in a 5-atom nonplanar molecule, there exist only nine distinct vibrational modes. Based on the calculated force constant matrix, projected VDOS for selected SS and MS paths were obtained via the EM method, yielding vibrational modes in excellent agreement with those found by DGauss (Fig. 4.1a–b). The peaks in the spectra calculated by the EM method are in perfect agreement with the corresponding DGauss modes.

Matrix Φ_{int} calculated using the matrix transformation (4.2) with B based on the

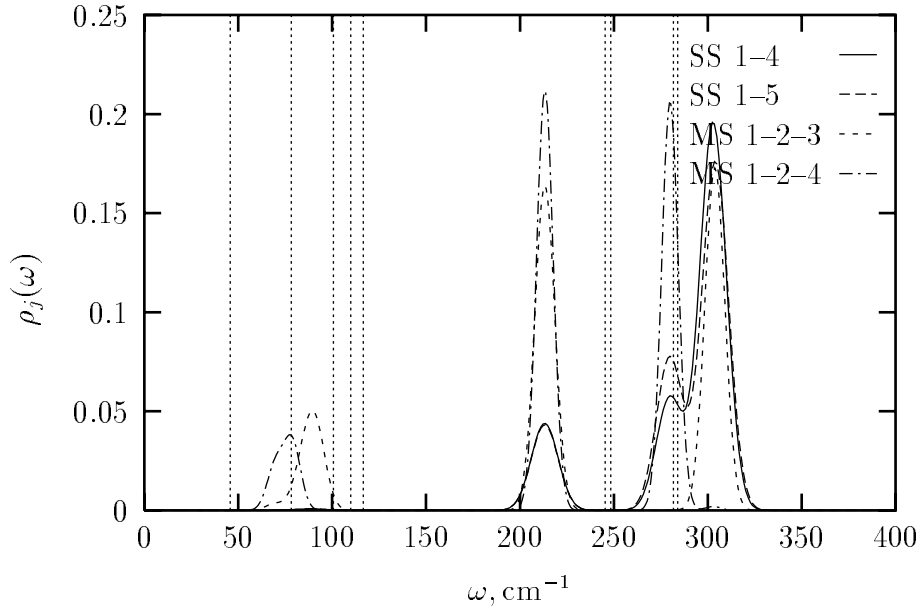


Figure 4.2: Projected VDOS for two SS paths, $\text{Fe}_1 \rightarrow \text{Cl}_4$ and $\text{Fe}_1 \rightarrow \text{Cl}_5$, and two MS paths, $\text{Fe}_1 \rightarrow \text{Cl}_2 \rightarrow \text{Cl}_3$ and $\text{Fe}_1 \rightarrow \text{Cl}_2 \rightarrow \text{Cl}_4$, calculated using the EM method and the 10-parameter VFF model.

internal coordinates S_t described above (Table 4.2) is given in Table 4.4. As one can see there is a significant coupling between different internal modes, e.g. $S_1 S_4$ and $S_6 S_9$ among others, which is important in DW factors for non-linear MS paths but has a much smaller effect for SS Fe–Cl paths (see Table 4.5 and Fig. 4.2). The values of σ_j^2 calculated at 20 and 300 K via the EM method using entire force constant matrix are presented in Table 4.5 in comparison with those obtained using the VFF model (see Sec. 2.3) with only 10 most important diagonal force constants, i.e. four bond stretches and six angle bends. The average EM σ^2 for the first shell at 10 K is equal to $2.925 \times 10^{-3} \text{ \AA}^2$ which is only 10.1% higher than the experimental value of $2.656 \times 10^{-3} \text{ \AA}^2$ [74] and is within our error bars of about 10-15%. Projected VDOS for four selected SS and MS paths based on the 10-parameter VFF model are shown in Fig. 4.2. The difference between these spectra and those shown in Fig. 4.1a–b illustrate the effect of non-diagonal force constants on vibrational spectra.

Table 4.5: SS and MS σ_j^2 for selected paths calculated via the EM method at two temperatures using the entire force constant matrix Φ in comparison with calculations based on the 10-parameter VFF model. Here scattering path indices j are equal to the corresponding internal coordinate indices t .

j	path description	20 K		300 K	
		Φ	VFF	Φ	VFF
1	$\text{Fe}_1 \rightarrow \text{Cl}_2$	2.97	2.84	5.40	5.09
2	$\text{Fe}_1 \rightarrow \text{Cl}_3$	2.92	2.80	5.25	4.94
3	$\text{Fe}_1 \rightarrow \text{Cl}_4$	2.89	2.79	5.24	4.92
4	$\text{Fe}_1 \rightarrow \text{Cl}_5$	2.92	2.79	5.26	4.93
5	$\text{Fe}_1 \rightarrow \text{Cl}_2 \rightarrow \text{Cl}_3$	4.59	4.97	12.53	14.59
6	$\text{Fe}_1 \rightarrow \text{Cl}_2 \rightarrow \text{Cl}_4$	5.13	5.06	17.68	15.56
7	$\text{Fe}_1 \rightarrow \text{Cl}_2 \rightarrow \text{Cl}_5$	4.83	5.02	15.24	15.16
8	$\text{Fe}_1 \rightarrow \text{Cl}_3 \rightarrow \text{Cl}_4$	4.66	4.93	13.66	14.43
9	$\text{Fe}_1 \rightarrow \text{Cl}_3 \rightarrow \text{Cl}_5$	5.04	5.01	16.92	15.12
10	$\text{Fe}_1 \rightarrow \text{Cl}_4 \rightarrow \text{Cl}_5$	4.52	4.90	11.94	14.18

The bond stretching force constants from the GGA calculations (i.e. 75.70, 78.05, 76.40, and 76.06 N/m) are approximately 20% weaker than those from the LDA calculations. Also, the GGA vibrational modes are 5–30 cm^{-1} lower. These discrepancies are largely due to the 3% difference between the GGA and LDA bond lengths.

4.2 XANES and XAFS analysis of tetramethylammonium tetrachloroferrate (II)

Theoretical calculations of K-edge XANES spectra in tetramethylammonium TCF (II) were done using the FEFF8X code. FEFF8X calculates EXAFS and XANES using real space multiple scattering approach and allows self-consistent calculation of

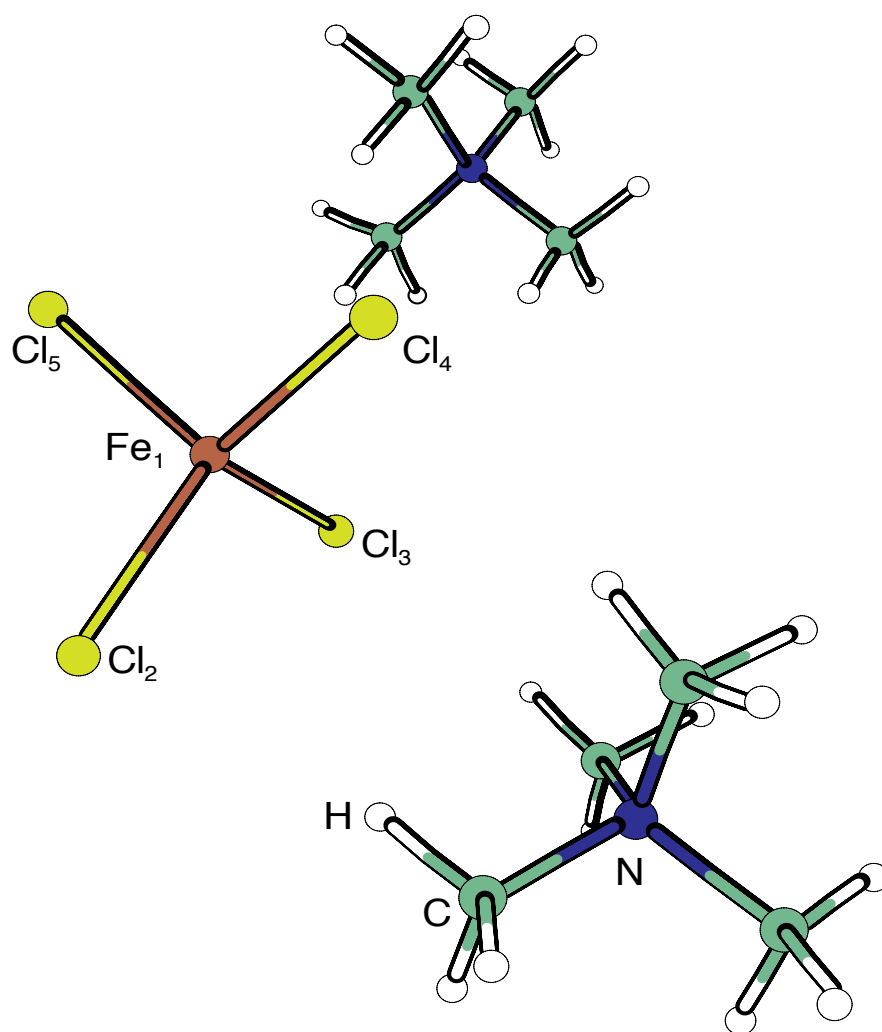


Figure 4.3: Structure of the 39-atom molecule of tetramethylammonium TCF (II), $[N(CH_3)_4]_2[FeCl_4]$, based on the coordinates given by Lauher and Ibers [5].

the potentials [20]. However, the self-consistent calculation did not produce adequate charge transfer for this material and was not used in the final calculations. Instead we used overlapped atomic potentials with ionicity 0.5 on the central Fe atom. In the course of the study we found that this slight ionization provides a better background $\mu_0(E)$ which is more peaked at the edge. Also, due to the low symmetry (slightly distorted tetrahedral for the first shell and overall orthorhombic space group D_{2h}^{16}), the spherically symmetric atomic potentials might be insufficient ¹.

The exchange correlation models used here were Hedin-Lundqvist with constant imaginary part for χ calculation and ground state with constants imaginary part for μ_0 [75]. The calculations were done for one entire molecule of tetramethylammonium TCF (II) containing 39 atoms with atomic coordinates as given by Lauher and Ibers [5] and the distance to the furthest atom equal to 6.9 Å. The resulting XANES spectrum is shown in Fig. 4.4 and the fine structure in Fig. 4.5 in comparison with experimental data [74]. An overall good agreement was achieved, although the white-line peak is not sufficiently high. The deficiency seems to be caused mostly by μ_0 calculation.

Projected electron densities of states (DOS) from the FEFF8X runs were compared to the corresponding DOS obtained from UniChem calculations for the same molecule (Fig. 4.6–4.8). Also, p-DOS was compared to χ since there is a direct correspondence between a K-edge fine structure and p-DOS (see Fig. 4.7). These comparisons provide a good test of accuracy of the calculations. The FEFF calculated DOS are in good agreement with DFT calculations up to a few eV above the Fermi level. The discrepancy for higher energies is due to insufficiencies in a basis set used in the DFT calculations by UniChem. Note that the FEFF d-DOS gives a crystal field splitting around 5 eV below the Fermi level on $e-$ (double degenerate) and t -orbitals (triple degenerate), thus there should be a 2:3 ratio in the heights of the peaks which is well

¹This could also be the reason why the charge transfers in the self-consistent runs were not very good.

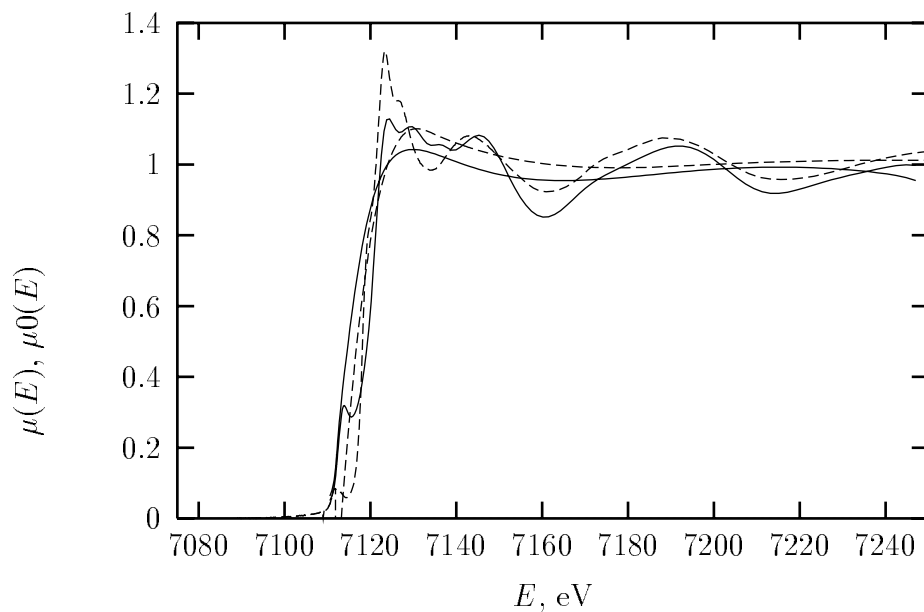


Figure 4.4: K-edge XANES spectra $\mu(E)$ and the corresponding backgrounds $\mu_0(E)$ for tetramethylammonium TCF (II) calculated with FEFF8X (solid) in comparison with experimental data (dashes).

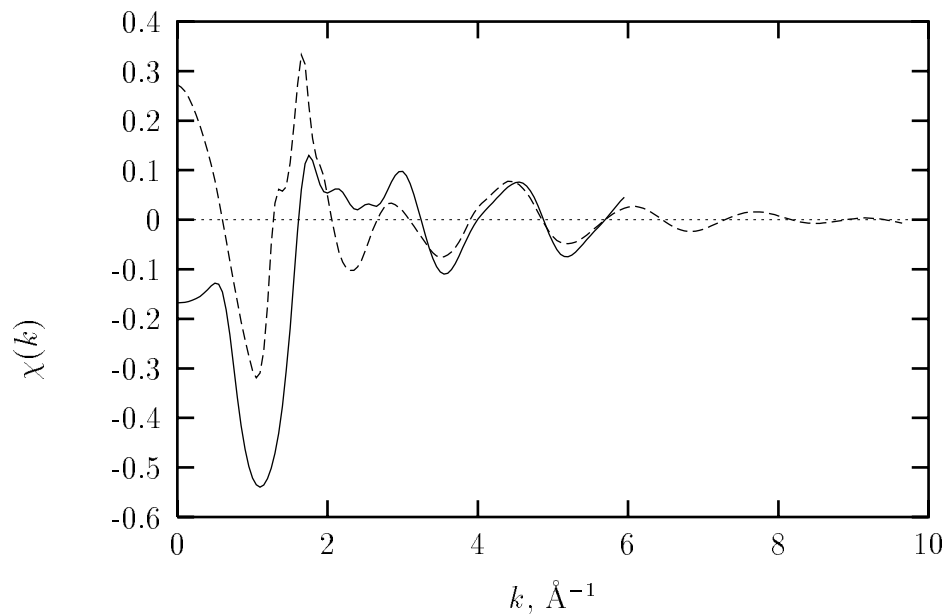


Figure 4.5: K-edge XAFS $\chi(k)$ for tetramethylammonium TCF (II) calculated with FEFF8X (solid) in comparison with experimental data (dashes).

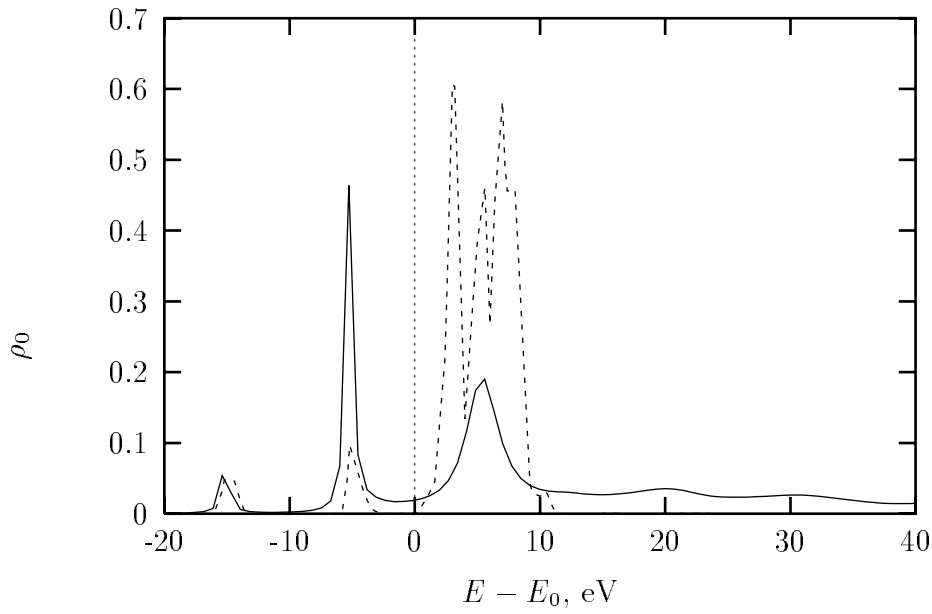


Figure 4.6: s-DOS for the central Fe^{+2} atom in tetramethylammonium TCF (II) as calculated with FEFF8X (solid line) in comparison with s-DOS calculated by UniChem (dashes).

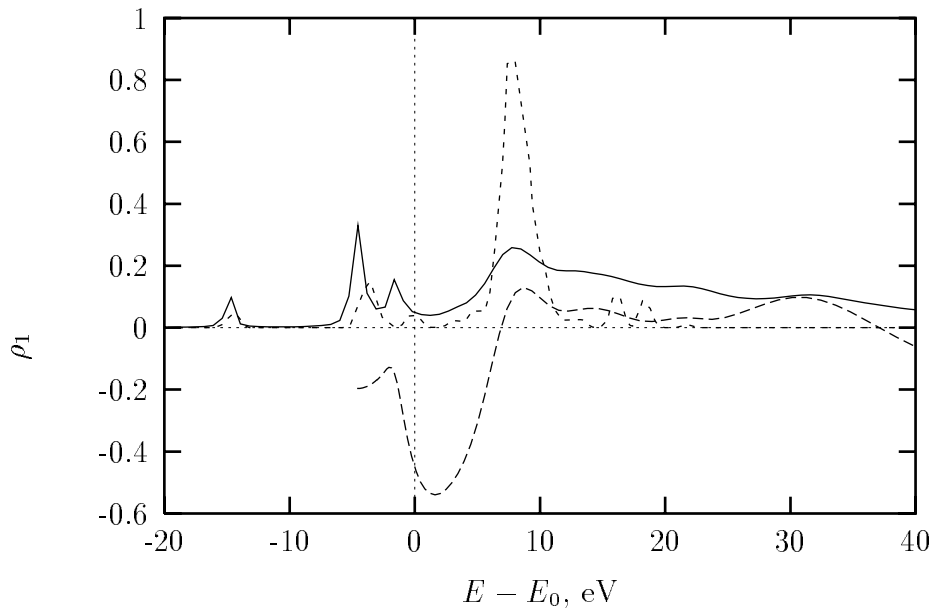


Figure 4.7: p-DOS for the central Fe^{+2} atom (solid line) and $\chi(k)$ (long dashes) for tetramethylammonium TCF (II) as calculated with FEFF8X in comparison with p-DOS calculated by UniChem (short dashes).

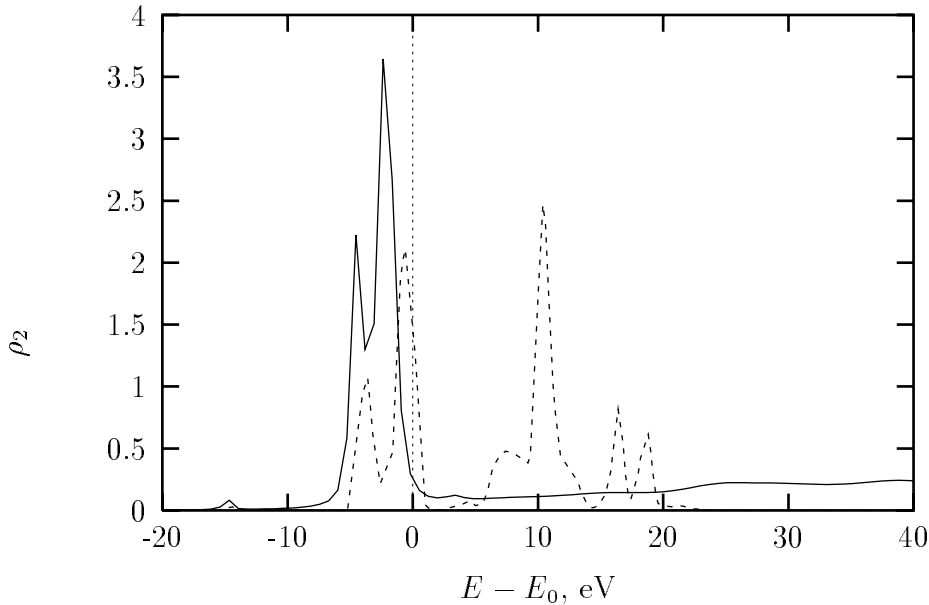


Figure 4.8: d-DOS for the central Fe^{+2} atom in tetramethylammonium TCF (II) as calculated with FEFF8X (solid line) in comparison with d-DOS calculated by UniChem (dashes).

reproduced in Fig. 4.8.

Fourier transforms of the fitted theoretical (FEFF8X) and experimental XAFS spectra for the first shell (Fe–Cl) of tetramethylammonium TCF (II) at room temperature are in very good agreement over the entire fit range, $R = [1.9, 3.5] \text{ \AA}$ (Fig. 4.9). The values of the fitting parameters found by FEFFIT are $S_0^2 = 0.94(3)$, $E_0 = -2.3(6)$ eV, and $\delta r = 0.052(5) \text{ \AA}$ with a strong correlation between E_0 and δr (0.87). This test provides another proof that our *ab initio* DW factors for the first shell are very close to their experimental values.

4.3 XANES and XAFS analysis of *Pyrococcus Furious* Rubredoxin

Rubredoxins are relatively low-molecular-weight proteins that contain a single iron atom tetrahedrally coordinated by four cysteinyl sulfur atoms. Two forms of *Pyrococcus Furious* rubredoxin, oxidized (Fe^{+3}) and reduced (Fe^{+2}), were considered in

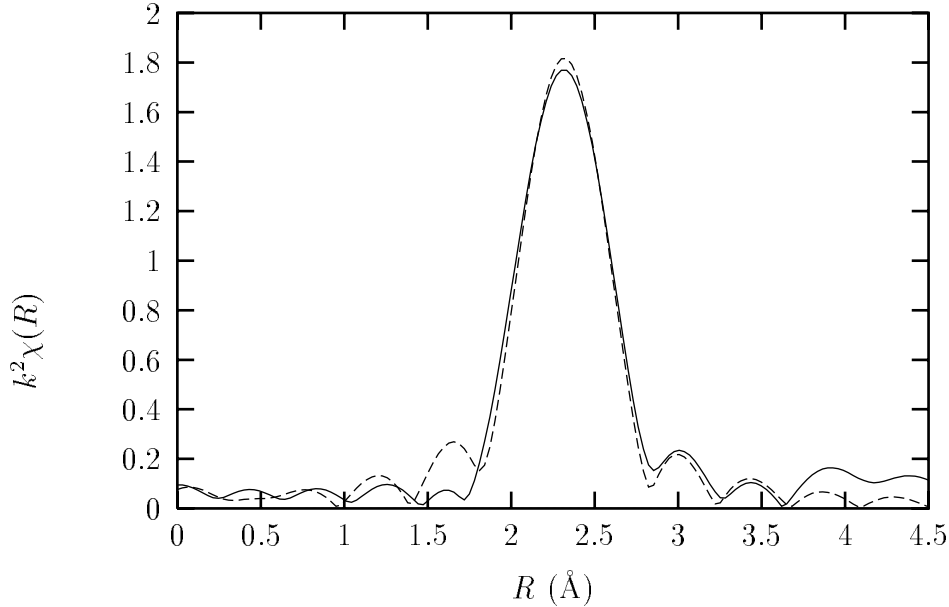


Figure 4.9: Magnitude of the phase corrected Fourier transform $\tilde{\chi}(R) = \text{FT}[k^2\chi(k)]$ for the first shell in tetramethylammonium TCF (II) at $T = 300$ K as extracted from the experiment (solid line), and as fitted using FEFF8X theoretical results with DW factors calculated via the EM method (dashes).

the XANES study. Both of them have a slightly distorted tetrahedral symmetry in the first coordination shell of the iron atoms. The average Fe–S interatomic distances are 2.289 \AA in the oxidized form and 2.330 \AA in reduced.

K-edge XANES spectra for the two rubredoxins were calculated using FEFF8X with self-consistent muffin-tin (SCMT) potentials and their automatic overlap. For exchange correlation potentials we used Hedin-Lundqvist form for the χ calculation and ground state with imaginary part for the μ_0 . The clusters for both materials consisted of one 25-atom molecule of *Pyrococcus Furious* rubredoxin with R_{max} equal to 5.659 \AA in the oxidized form and 5.707 \AA in reduced. The resulting XANES spectra are shown in Fig. 4.12 for the oxidized form and in Fig. 4.13 for reduced. As one can see, experimental features were reproduced fairly well in both cases. Also, above 7180 eV theoretical spectrum of oxidized rubredoxin exhibits a relative shift to the

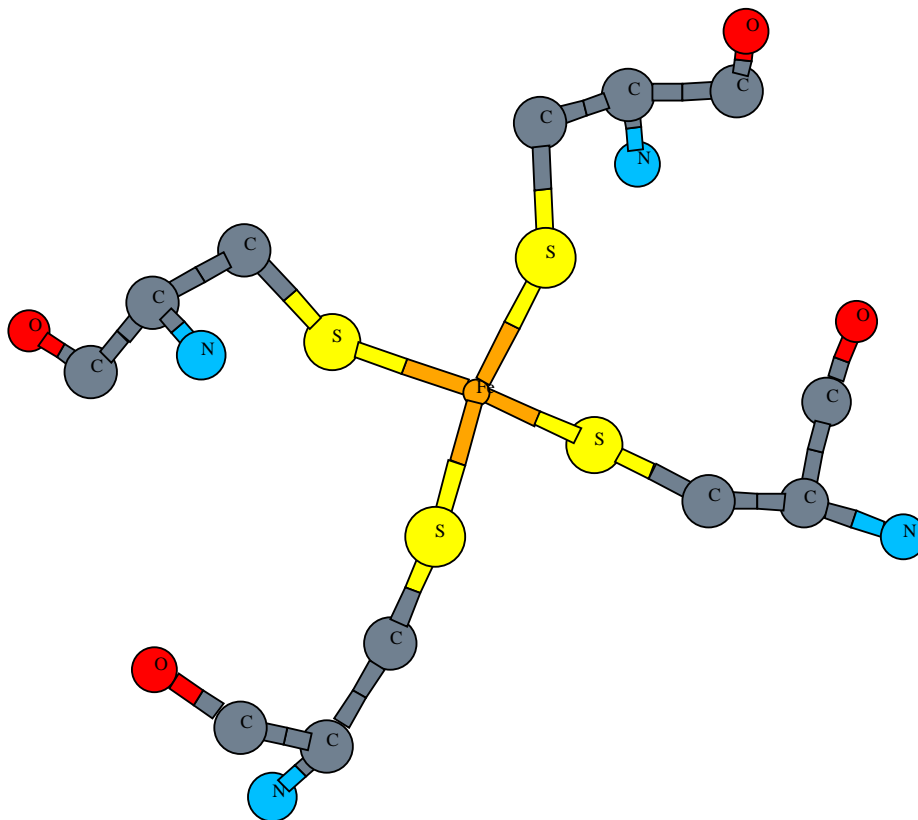


Figure 4.10: Atomic structure of a molecule of oxidized *Pyrococcus Furiosus* Rubredoxin.

right by about 5 eV relatively to the spectrum of its reduced form. This effect is consistent with the corresponding shift in the experimental spectra (see Fig. 4.13).

Projected electron p -DOS for the two rubredoxins were compared to the corresponding XAFS (see Fig. 4.14). There is an apparent correlation of peaks in p -DOS and χ .

Force constants for the bonds and angles involving Fe, S, and C atoms which we used in the σ^2 calculations were fitted to experimental vibrational spectra for oxidized rubredoxin and its analogs by Czernuszewicz *et al.* [43] whereas the remaining force

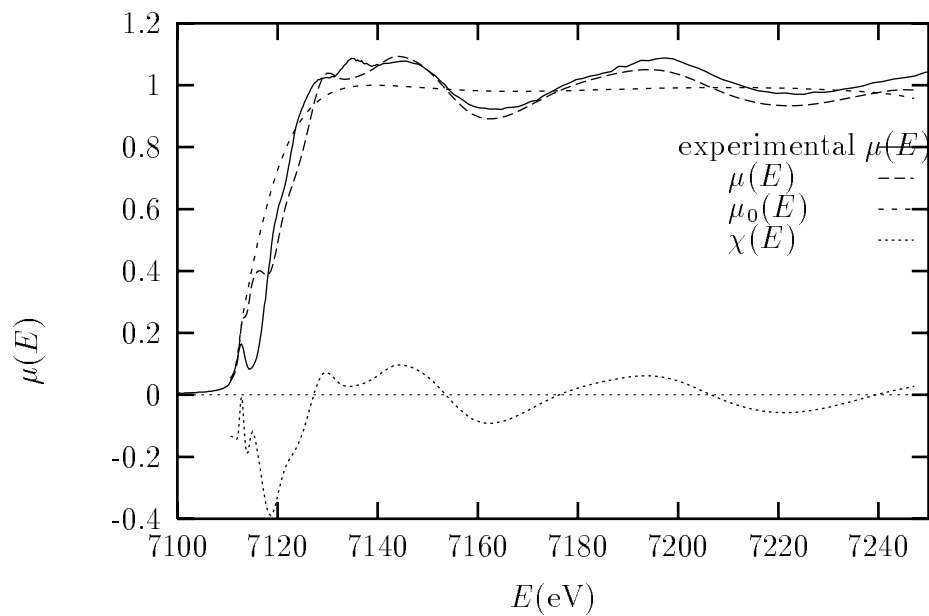


Figure 4.11: Fe K-edge XANES spectra for oxidized (Fe^{+3}) rubredoxin calculated with FEFF8X in comparison with experimental data.

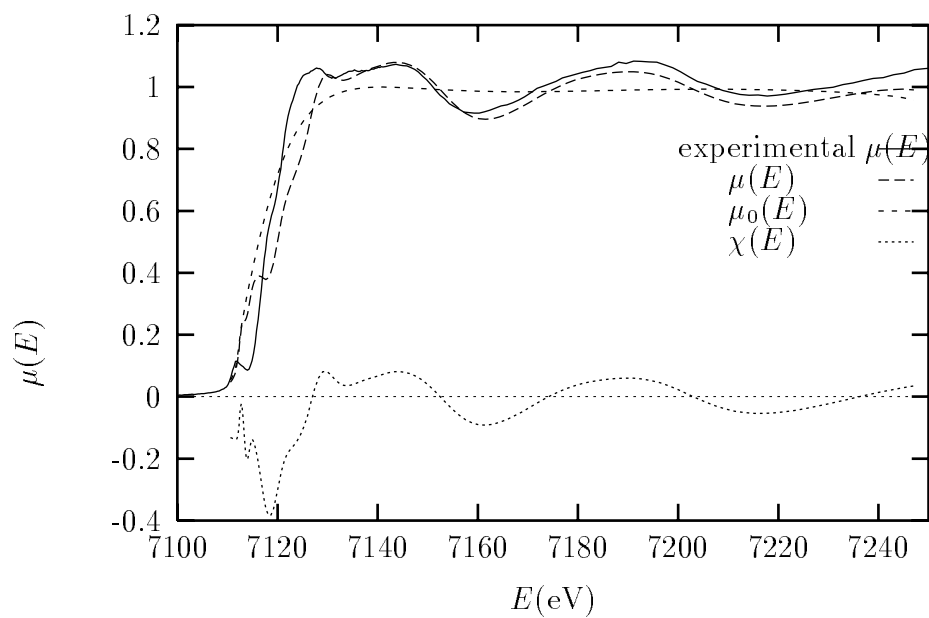


Figure 4.12: Fe K-edge XANES spectra for reduced (Fe^{+2}) rubredoxin calculated with FEFF8X in comparison with experimental data.

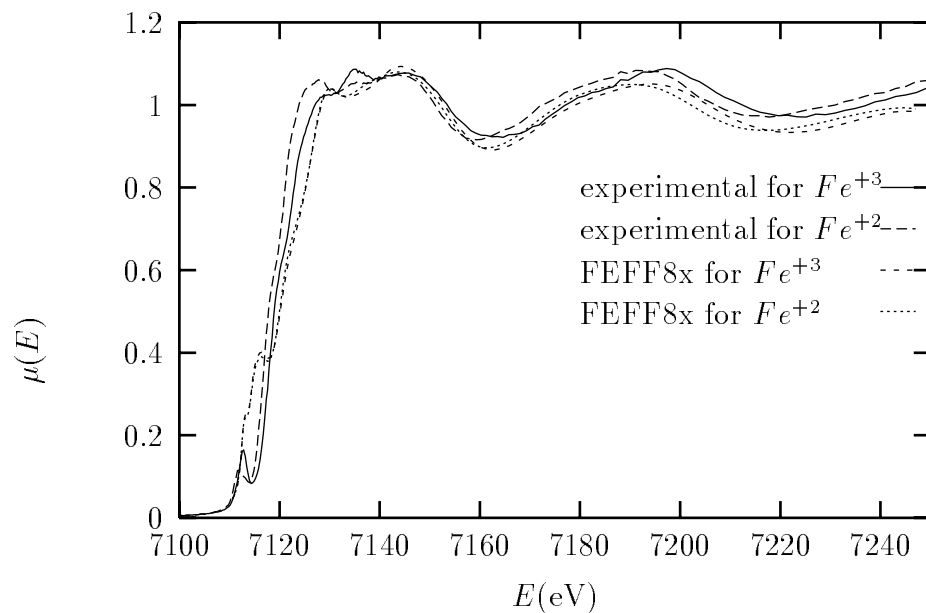


Figure 4.13: Comparison of XANES spectra $\mu(E)$ calculated with FEFF8X and experimental data for both forms of rubredoxin.

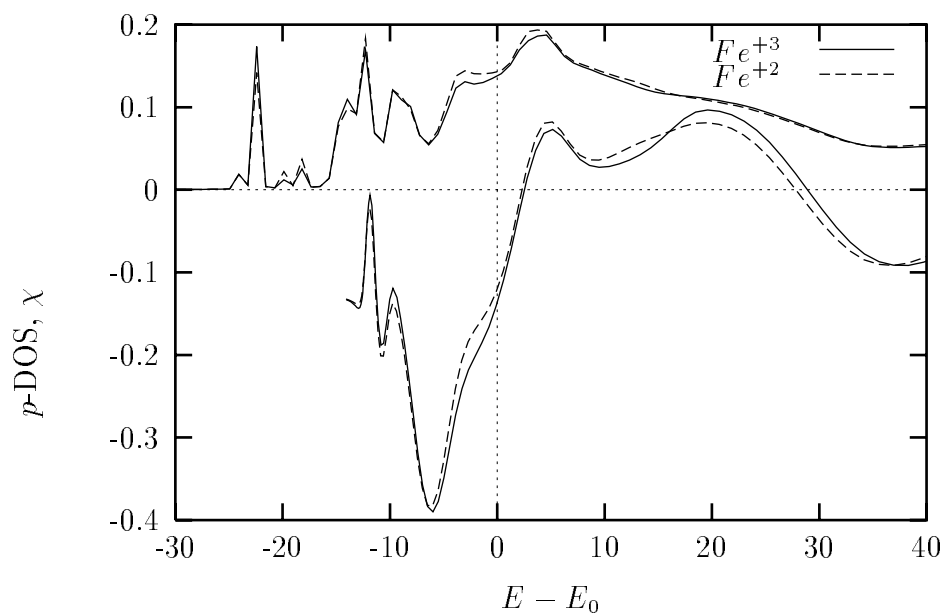


Figure 4.14: p-DOS for the central Fe atom and χ in both forms of rubredoxin.

Table 4.6: Force constants used for σ_j^2 calculation in oxidized rubredoxin. Bond stretching force constants are in units of mdyn/Å and bond bending are in mdynÅ/rad².

Description	Value
Fe–S stretch	1.34
C–S stretch	3.05
C–C stretch	4.80
C–N stretch	8.39
S–Fe–S bend	0.35
Fe–S–C bend	0.25
S–C–C bend	0.82
N–C–C bend	1.12
Fe–S\Fe–S coupling	0.07

constants (i.e. C–N stretch and N–C–C bend) were calculated using the UFF model [66] (see Section 2.4). Resulting σ^2 's for selected paths are presented in Tab. 4.7. The average EM σ^2 for the first shell at 10 K is equal $2.475 \times 10^{-3} \text{ \AA}^2$ which is 9.7% lower than its experimental value of $2.74(10) \times 10^{-3} \text{ \AA}^2$ [76].

Fourier transforms of the fitted theoretical (FEFF8X) and experimental XAFS spectra for the first 40 most significant paths (with maximum $R_{\text{eff}} = 4.702 \text{ \AA}$) at 10 K are in very good agreement for distances of up to 4.5 \AA in R-space (Fig. 4.15). We were able to reproduce the spectral features in $3.5\text{--}4.5 \text{ \AA}$ range by going beyond the first shell fit. This agreement with experiment also shows that our EM DW factors for MS work very well for this material. The values of fitting parameters found by FEFFIT are $S_0^2 = 0.95(4)$, $E_0 = -7.3(9) \text{ eV}$, and $\delta r = 0.008(6) \text{ \AA}$ with a strong correlation between E_0 and δr (0.88).

Table 4.7: SS and MS σ_j^2 for selected paths calculated via the EM method at two temperatures 10 and 300 K.

j	path description	R_j	$\sigma_j^2(10K)$	$\sigma_j^2(300K)$
1	$\text{Fe}_1 \rightarrow \text{S}_2$	2.2528	2.48	3.94
2	$\text{Fe}_1 \rightarrow \text{S}_3$	2.2538	2.48	3.94
3	$\text{Fe}_1 \rightarrow \text{S}_4$	2.3104	2.47	3.93
4	$\text{Fe}_1 \rightarrow \text{S}_5$	2.3300	2.47	3.93
5	$\text{Fe}_1 \rightarrow \text{C}_6$	3.2260	7.52	31.94
6	$\text{Fe}_1 \rightarrow \text{C}_7$	3.2402	7.51	31.95
9	$\text{Fe}_1 \rightarrow \text{C}_6 \rightarrow \text{S}_4$	3.6756	4.22	11.58
10	$\text{Fe}_1 \rightarrow \text{C}_7 \rightarrow \text{S}_5$	3.6893	4.22	11.59
14	$\text{Fe}_1 \rightarrow \text{N}_{10}$	3.7331	6.66	26.56
15	$\text{Fe}_1 \rightarrow \text{S}_4 \rightarrow \text{S}_3$	4.0629	4.06	10.83

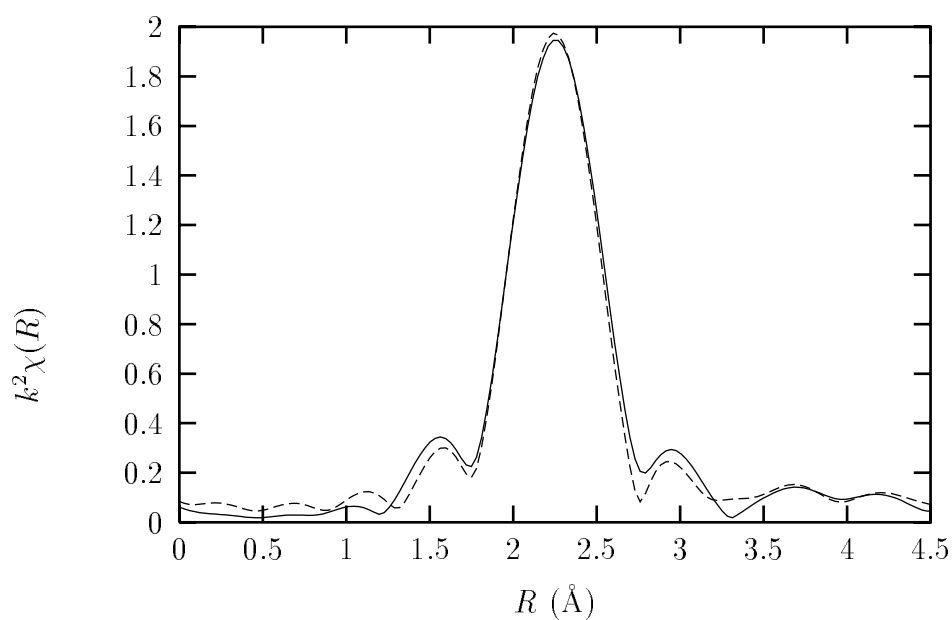


Figure 4.15: Magnitude of the phase corrected Fourier transform $\tilde{\chi}(R) = \text{FT}[k^2\chi(k)]$ for oxidized rubredoxin at $T = 10$ K as extracted from the experiment (solid line), and fitted using FEFF8X theoretical results with DW factors calculated via the EM method (dashes).

Chapter 5

ANHARMONIC AND SPHERICAL WAVE CORRECTIONS

Here we will show how effects due to anharmonic corrections to the potential energy may be approximated by using the results from Refs. [21] and [7]. Sample case of Cu is considered. We will also show how to approximate effects arising from spherical wave corrections based on the values of σ^2 .

5.1 Cumulant expansion

In general, anharmonicity leads to interactions between the various modes, and gives a contribution to $\sigma_j^2(T)$ that increases with temperature. Detailed discussions on this topic can be found in the literature [7, 17, 21, 31], here we will only briefly outline the main formalism. Due to anharmonic effects, the Gaussian approximation for DW factor Eq. (1.1) is not precisely valid, and the general cumulant expansion [17] has to be considered instead, that is

$$\langle e^{i2k(r_j - R_j)} \rangle = \exp \sum_{n=0}^{\infty} \frac{(2ik)^n}{n!} \sigma_j^{(n)} = e^{-W_j + i\Phi_j}, \quad (5.1)$$

where $\sigma_j^{(n)}$ denotes the n th cumulant average,

$$\sigma_j^{(1)} = \langle (r_j - R_j) \rangle, \quad (5.2)$$

$$\sigma_j^{(2)} = \langle (r_j - R_j)^2 \rangle \equiv \sigma_j^2(T), \quad (5.3)$$

$$\sigma_j^{(3)} = \langle (r_j - R_j)^3 \rangle, \quad (5.4)$$

$$\sigma_j^{(4)} = \langle (r_j - R_j)^4 \rangle - 3(\sigma_j^{(2)})^2, \quad (5.5)$$

etc. Thus, neglecting small contributions from the mean free path, the general DW factor contains only even moments $W_j = 2\sigma_j^2 k^2 - 2/3 \sigma_j^{(4)} + \dots$, whereas odd moments contribute to the XAFS phase $\Phi_j = 2k\sigma_j^{(1)} - 4/3 \sigma_j^{(3)} k^3 + \dots$. We will adopt the prescription originally derived for the anharmonic CE model, [7,21] as characterized by an effective cubic anharmonic pair potential $V(x) = 1/2 kx^2 + k_3 x^3$ which includes the effects of neighboring springs (here $x = r - R$). In this prescription all the cumulants can be expressed simply as a function of the second cumulant $\sigma_j^2(T)$ and the ratio of the cubic anharmonicity parameter k_3 to the effective spring constant k ,

$$\frac{\sigma_j^{(3)}}{\sigma_j^{(1)} \sigma_j^2(T)} = 2 - \frac{4}{3} \left[\frac{\sigma_{0j}^2}{\sigma_j^2(T)} \right]^2. \quad (5.6)$$

Here, generalized for the MS case, $\sigma_{0j}^2 = \hbar(8m_j \omega_E(R_j))^{-1}$ is zero-point contribution to $\sigma_j^2(T)$, $\omega_E^2(R_j) = \langle Q_j(0) | D | Q_j(0) \rangle$, $\sigma_j^{(1)} = -3\sigma^2(T)k_3/k$, and $k \equiv 4m_j \omega_E^2(R_j)$. Thus only $\sigma_j^2(T)$, e.g. from Eq. (2.5) or from the CE model $\sigma_j^2(T) = \sigma_{0j}^2 \coth(\theta_E^j/T)$, and k_3/k are needed to obtain $\sigma_j^{(1)}$ and $\sigma_j^{(3)}$. The latter can be obtained using its relation to thermal expansion coefficient, $\alpha = (1/R)dR(T)/dT$ [21],

$$\frac{k_3}{k} = \frac{-2k^2(1-z)^3}{3z(1+z)\ln(1/z)(\hbar\omega)^2} \alpha \sigma_j^2(T) R_j T, \quad (5.7)$$

where $z \equiv \exp(-\theta_E^j/T)$.

Furthermore, because of thermal expansion, one expects the microscopic force constants, which depend on the bond lengths, and hence, the phonon frequencies, to vary with temperature and pressure. To estimate the effect at high temperatures ($T \geq \theta_D$), one may approximate $\sigma_j^2 \sim k_B T \int d\omega \rho_j(\omega)/\omega^2 = k_B T/\bar{\omega}^2$. This yields an additional linear anharmonic temperature dependence,

$$\sigma_j^2(T) \rightarrow \sigma_j^2(T)(1 + CT). \quad (5.8)$$

Table 5.1: Third cumulants for the first nearest neighbor in Cu calculated using thermal expansion coefficient α [7] for different temperatures T .

T (K)	α (10^{-5} K $^{-1}$)	$\sigma_{Einstein}^2$ (\AA^2)	σ^3 (10^{-4}\AA^3)	σ_{exp}^3 (10^{-4}\AA^3)
77	0.59	0.00290	0.138	–
100	0.80	0.00311	0.175	–
295	1.65	0.00626	1.56	1.3

Here the coefficient $C \simeq -2/\bar{\omega} d\bar{\omega}/dT = 6\alpha\gamma$ is linearly proportional to the linear thermal expansion coefficient $\alpha = (3V)^{-1}\partial V/\partial T$ and the Gruneisen parameter $\gamma = -\partial(\ln\bar{\omega})/\partial(\ln V)$. Quartic and higher cubic ($\sim k_3^2$) terms in the lattice Hamiltonian also lead to corrections of the same linear in T form as in Eq. (5.8). For Cu $C \simeq 0.05/\theta_D$. [17]

Equations 5.6–5.7 were used to calculate σ^3 for the first shell in Cu crystal. Here CE model with $\omega_E = 36.4$ THz (see Sec. 3.2) was used to obtain σ^2 values. Results are presented in Tab. 5.1.

5.2 Spherical wave corrections

The effect of spherical wave corrections can be estimated using the spherical wave approximation. [77] In this approximation the effective scattering amplitude has an additional phase factor for each l , i.e. $t_l \rightarrow t_l \exp(iL^2/pR)$, where $t_l = \exp(i\delta_l) \sin(\delta_l)$ is the dimensionless scattering matrix in terms of partial-wave phase shifts δ_l and $L^2 = l(l+1)$. Consequently there is an additional l -dependent DW factor for each l , $t_l \rightarrow t_l \exp(-W_l)$ where

$$W_l = 2p^2\sigma_R^2 \left[\left(1 - \frac{L^2}{2p^2 R^2} \right)^2 - 1 \right] \simeq -\frac{2\sigma_R^2 L^2}{R^2}, \quad (5.9)$$

where $p = \sqrt{k^2 + k_F^2} + i/\lambda$. Note that these contributions are independent of energy

and are usually small since t_l is negligible for $l > pR$. They tend to reduce the DW factor. The leading correction in Eq. (5.9) is often sufficient since $|p| > k_F$, where $k_F = O(1\text{\AA}^{-1})$. There are also small corrections to the XAFS phase from the overall $1/(pR)^2$ and $\exp(-2R/\lambda)$ factors, i.e. $W \rightarrow 2p^2\sigma_R^2 - 4ip\sigma_R^2/R$.

Chapter 6

CONCLUSIONS

I do not know what I may appear to the world; but to myself I seem to have been only like a boy playing on the sea-shore, and diverting myself in now and then finding a smoother pebble or a prettier shell than ordinary, whilst the great ocean of truth lay all undiscovered before me.

Issac Newton, (1642–1727)

Despite the wide use and popularity of XAFS analysis, conventional methods for calculation of XAFS DW factors are still very limited in their application: some of them are restricted to only SS cases [9, 19], others, such as CD and CE models, are isotropic and can be very inaccurate for inhomogeneous materials. Although our results indicate that the CD model works fairly well for isotropic materials like crystalline Cu, where the error for all paths at high temperatures does not exceed 25% and is half of that at low temperatures, it works poorly for the first shell in crystalline Ge, giving an error of about 50% at 300 K (Fig. 2.7). The importance of taking into account distinct features of the local environment around the scattering center, such as details of the interaction field, has been demonstrated in this dissertation for a number of cases.

In the present work we attempted to improve the existing methods and to develop a new general formalism for XAFS DW factor calculations. Two possible improvements include the EM method and the recursion method. These methods allow an efficient and general approach to calculation of the XAFS DW factors for MS as well as SS cases in terms of a few local force constants.

Our results illustrate a number of advantages of the EM method in comparison

with traditional isotropic models, especially for heterogeneous materials which are those of the greatest interest in XAFS studies. Due to the local nature of the DW factors, the EM method can be successfully applied to small and irregular structures by focusing on the vicinity of the scattering atom. It requires no symmetry specification or boundary conditions. Because no secular equations or matrix diagonalizations are involved and the scaling of the numerical procedure is linear with system size, the method is efficient even for clusters of more than several hundred atoms. In that case solving the “exact” eigenvalue problem is very time-consuming, since it scales as $(3N)^3$ for systems with low symmetry where N is the number of atoms in the cluster. The real time approach to calculations of σ_j^2 's using Eq. (2.7) shows that, in principle, it is not necessary to determine the projected VDOS as an intermediate step which further simplifies the numerical computation. We have not used this approach in the present work for it is valuable to see the VDOS as well. Also, values of $\sigma_j^2(T)$ for any temperature T can be calculated once $\rho_j(\omega)$ is obtained. In fact, in many cases analysis of vibrational spectra may provide additional information for refining the dynamical model used in the EM method. As mentioned earlier, our study shows that isotropic models can be inaccurate not only for such highly inhomogeneous materials as organic and organometallic complexes but even for some loose packed monoatomic crystals like Ge. Our results also illustrate the importance of correlations in modeling vibrational properties of materials. The correlations decay with distance, and indicate how σ_j^2 converges to $\sum u_j^2$.

The EM method can be very valuable when applied to EXAFS analysis in biological systems. One of its most important features is that given a few FF parameters one can calculate XAFS DW factors from first principles even when experimental data for ω_D or ω_E is not available or hard to extract, which is often the case for biological complexes. Having a general and efficient method for the DW factor calculations is also important because of the difficulties in fitting these factors to experiment. The typical number of independent points in EXAFS measurement [12,33] for a biological

compound is rather small, about 10–15. This is because the data is reliable only in a narrow band in k -space (because of large scattering from the low-weight atoms) and in a narrow range of about 1.5–5.0 Å in R -space (because of large disorder). Thus, there is a strong limitation on the number of fitting parameters for such materials. Since for highly disordered systems there is usually a need to fit many structural parameters, it is very helpful to have a reliable theoretical method for DW factors calculation in such cases. For the same reason, it is also desirable to have a general, efficient, and reliable way of obtaining VFF model parameters *ab initio*, and we are currently exploring this possibility. DFT code DGauss has been successfully tested for this purpose in application to an anion of tetrachloroferrate (II), allowing us to calculate DW factors from first principles. These DW factors were then used in XAFS analysis of tetramethylammonium tetrachloroferrate (II). The resulting theoretical Fourier transform of the spectrum is in very good agreement with experiment, and the *ab initio* σ^2 value for the first shell appear to be within the error bars of the experimental value. Although *ab initio* calculations are definitely appealing, they are also very time consuming. Another option for a source of force constants would be to use semiempirical FF parameters. In Sec. 2.4, we provided a discussion on the availability and transferability of FF parameters in application to both crystalline and disordered materials. We also calculated and successfully applied semiempirical SS and MS DW factors in XAFS analysis of oxidized *Pyrococcus Furiosus* rubredoxin. In conclusion to our development of the MS EM formalism, we can say that the excellent agreement of theoretical and experimental spectra in R -space for all materials tested, both crystalline and biological, shows that the EM DW factors work very well for SS as well as MS paths. These are novel results which meet the goals set in the beginning of our work.

In this dissertation we also introduced a next step improvement to the traditional CE model which is applicable to both MS and SS cases, i.e. the recursion method. The RM is based on a two-point δ -function approximation of the projected VDOS obtained

from a few local force constants and takes into account both effective optical and acoustic modes. Although the RM yields accuracy comparable to the EM method, it requires less computation time and can be easily used for ionic crystals, in which EM approach can be unstable unless proper boundary conditions are applied.

Our study also shows that the largest errors of isotropic models typically correspond to the first few most significant paths. Therefore, for some cases it might be reasonable to use the RM or the EM method only for these most significant paths while adopting the isotropic models for the rest. This could save a significant amount of computation time without sacrificing much accuracy. Both presented methods are coded in FORTRAN 77 and are compatible with the FEFF program.

Although a large amount of research on the XAFS DW factor calculations has been done in this dissertation, there are still many remaining issues to resolve and ideas to investigate. Future extensions to this work might include:

- Incorporation of the SIGEM subroutine into FEFFIT to test our prescription for direct fitting of the FF parameters to XAFS spectra.
- Inclusion of higher (third, fourth, *etc.*) tiers in the RM. These corrections could improve the method in application to materials with highly inhomogeneous structure and wide vibrational bands.
- Continuation of work on *ab initio* FF calculations. Ideally, it would be nice to have a subroutine within the FEFF code to do the job.
- Solving the exact problem, i.e. in terms of eigenvalues and eigenfunctions (Eq. 2.9), and comparing its results to the EM method. This might be a good alternative method for very small atomic clusters ($N < 20$).

BIBLIOGRAPHY

- [1] R. B. Gregor and F. W. Lytle. Extended x-ray absorption fine structure determination of thermal disorder in Cu: Comparison of theory and experiment. *Phys. Rev. B*, **20**:4902, 1979.
- [2] E. A. Stern, B. A. Bunker, and S. M. Heald. Many-body effects on extended x-ray absorption fine structure amplitudes. *Phys. Rev. B*, **21**:5521, 1980.
- [3] M. F. Thorpe. Effect of local order on phonon density of states. *Phys. Rev. B*, **8**:5352, 1973.
- [4] P. W. Loeffen, R. F. Pettifer, and J. Tomkinson. Vibrational force field of zinc tetraimidazole from inelastic neutron scattering. *Chem. Phys.*, **208**:403, 1996.
- [5] J. W. Lauher and J. A. Ibers. Structure of Tetramethylammonium Tetrachloroferrate (II), $[\text{N}(\text{CH}_3)_4]_2[\text{FeCl}_4]$. Comparison of Iron (II) and Iron (III) Bond lengthd in Hight-Spin Tetrahedral Environments. *Inorganic Chemistry*, **14**:348, 1975.
- [6] Matt Newville. private communication.
- [7] N. V. Hung and J. J. Rehr. Anharmonic correlated Einstein-model Debye-Waller factors. *Phys. Rev. B*, **56**:43, 1997.
- [8] G. Beni and P. M. Platzman. Temperature and polarization dependence of extended x-ray absorption fine-structure spectra. *Phys. Rev. B*, **14**:1514, 1976.

- [9] G. Dalba and P. Fornasini. EXAFS Debye-Waller factor and thermal vibrations of crystals. *J. Synchrotron Rad.*, **4**:243, 1997.
- [10] Edward A. Stern. *X-Ray Absorption: Principles, Applications, Techniques of EXAFS, SEXAFS, and XANES*, chapter 1, Theory of EXAFS. John Wiley & Sons, Inc, 1988.
- [11] S. I. Zabinsky, J. J. Rehr, A. Ankudinov, R. C. Albers, and M. J. Eller. MS calculations of x-ray-absorption spectra. *Phys. Rev. B*, **52**:2995, 1995.
- [12] M. G. Newville. *Local Thermodynamic Measurements of Dilute Binary Alloys Using XAFS*. PhD thesis, University of Washington, 1995.
- [13] A. V. Poiarkova and J. J. Rehr. *Ab initio* XAFS Debye-Waller factors. *J. Phys. IV France*, **7**:C2–155, 1997.
- [14] A. V. Poiarkova and J. J. Rehr. Multiple-scattering x-ray absorption fine-structure Debye-Waller factor calculations. *Phys. Rev. B*, **59**:948, 1999.
- [15] A. V. Poiarkova and J. J. Rehr. Recursion method for multiple scattering XAFS Debye-Waller factors. *J. Synchrotron Rad.*, 1999. to be published.
- [16] T. Fujikawa and J. J. Rehr. *J. Synchrotron Rad.*, 1998. to be published.
- [17] E. D. Crozier, J. J. Rehr, and R. Ingalls. Amorphous and Liquid Systems. In D. C. Koningsberger and R. Prins, editors, *X-Ray Absorption: Principles, Applications, Techniques of EXAFS, SEXAFS, and XANES*, pages 375–384. John Wiley & Sons, 1988.
- [18] A. A. Maradudin, E. W. Montroll, G. H. Weiss, and I. P. Ipatova. *Theory of Lattice Dynamics in the harmonic Approximation*. Academic Press, 2nd edition, 1971.

- [19] E. Sevillano, H. Meuth, and J. J. Rehr. Extended x-ray absorption fine structure Debye-Waller factors. I. Monoatomic crystals. *Phys. Rev. B*, **52**:4908, 1979.
- [20] J. J. Rehr A. L. Ankudinov, B. Ravel and S. D. Conradson. Real-space multiple-scattering calculation and interpretation of x-ray-absorption near-edge structure. *Phys. Rev. B*, **58**:7565, 1998. see also <http://leonardo.phys.washington.edu/feff>.
- [21] A. I. Frenkel and J. J. Rehr. Thermal expansion and x-ray-absorption fine-structure cumulants. *Phys. Rev. B*, **48**:585, 1993.
- [22] Neil W. Ashcroft and N. David Mermin. *Solid State Physics*. Saunders College Publishing, 1976.
- [23] D. Beeman and R. Alben. Vibrational properties of elemental amorphous semiconductors. *Adv. Phys.*, **26**:339, 1977.
- [24] J. J. Rehr and R. Alben. Vibrations and electronic states in a model amorphous metal. *Phys. Rev. B*, **16**:2400, 1977.
- [25] J. J. Rehr. EXAFS Debye-Waller Factors II: Theory. unpublished.
- [26] M. J. P. Musgrave and J. A. Pople. A general valence force field for diamond. *Proc. Roy. Soc. (London)*, **A268**:474, 1962.
- [27] Jr. E. Bright Wilson, J. C. Decius, and Paul C. Cross. *Molecular Vibrations. The theory of infrared and Raman Vibrational Spectra*. McGraw-Hill Book Company, Inc., 1955.
- [28] Clark R. Landis, Daniel M. Root, and Thomas Cleveland. *Reviews in Computational Chemistry*, volume Vol. VI, chapter Chapter 2. Molecular mechanics force fields for modeling inorganic and organometallic compounds, pages 73–148. VCH Publishers, Inc. New York, 1995.

- [29] M. Born and K. Huang. *Dynamical Theory of Crystal Lattices*. Oxford University Press, 1954.
- [30] P. N. Keating. Effect of invariance requirements on the elastic strain energy of crystals with application to the diamond structure. *Phys. Rev.*, **145**:637, 1966.
- [31] T. Fujikawa, T. Miyanaga, and T. Suzuki. Quantum statistical approach to Debye-Waller factors in EXAFS, EELS and ARXPS. V. Real space approach to one-dimensional systems. *J. Phys. Soc. Jpn.*, **66**:2897, 1997.
- [32] A. F. Wells. *Structural Inorganic Chemistry*. Clarendon Press, Oxford, 1984.
- [33] E. A. Stern, M. Newville, B. Ravel, Y. Yakoby, and D. Haskel. The UWXAFS analysis package: philosophy and details. *Phys. Rev. B*, **208&209**:117, 1995. see also <http://leonardo.phys.washington.edu/uwxafs>.
- [34] J. M. Tranquada and C. Y. Yang. EXAFS measurements of bond-stretching force constants in arsenic and arsenic compounds. *Solid State Communications*, **63**:211, 1987.
- [35] C. Isenberg. Expansion of the vibrational spectrum at low frequencies. *Phys. Rev.*, **150**:712, 1966.
- [36] K. P. Huber and G. Herzberg. *Molecular Spectra and Molecular Structure. IV. Constants of diatomic molecules*. Van Nostrand Reinhold Company, New York, 1979.
- [37] Sven J. Cyvin. *Molecular Vibrations and Mean Square Amplitudes*. American Elsevier Publishing Company, Inc., 1968.
- [38] W. Goldammer, W. Ludwig, and W. Zierau. Nonlocal dipole model for the phonon dispersion in diamond-type lattices. *Phys. Rev. B*, **36**:4624, 1987.

- [39] Manvir S. Kushwaha. Normal modes of vibrations in transition metal oxides. *Physica B & C*, **112B+C**:232, 1982.
- [40] Manvir S. Kushwaha. Lattice dynamics of alkali halides (LiF and NaCl). *Nuovo Cimento B*, **60B**:187, 1980.
- [41] Manvir S. Kushwaha. Lattice dynamics of sodium and rubidium halides. *Nuovo Cimento B*, **60B**:201, 1980.
- [42] Gordon J. Kearly. A profile-refinement approach for normal-coordinate analyses of inelastic neutron-scattering spectra. *J. Chem. Soc. Faraday Trans. 2*, **82**:41, 1986.
- [43] Roman S. Czernuszewicz, LaTonya K. Kilpatrick, Stephen A. Koch, and Thomas G. Spiro. Resonance Raman Spectroscopy of Iron(III) Tetrathiolate Complexes: Implications for the Conformation and Force Field of Rubredoxin. *J. Am. Chem. Soc.*, page 7134, 1994.
- [44] R. Alben, D. Weaire, J. E. Smith, and M. H. Brodsky. Vibrational properties of amorphous Si and Ge. *Phys. Rev. B*, **11**:2271, 1974.
- [45] Richard M. Martin. Elastic properties of ZnS structure semiconductors. *Phys. Rev. B*, **1**:4005, 1970.
- [46] Eiji Osawa and Kenny B. Lipkowitz. *Reviews in Computational Chemistry*, volume Vol. VI, chapter Appendix 1. Published force field parameters, pages 355–381. VCH Publishers, Inc. New York, 1995.
- [47] Peper Brüesch. *Phonons: Theory and Experiments I. Lattice dynamics and models of Interatomic Forces*. Springer-Verlag, New York, 1982.

- [48] J. Andzelm and E. Wimmer. Density functional Gaussian-type-orbital approach to molecular geometries, vibrations, and reaction energies. *J. Chem. Phys.*, **90**(2):1280, 1992.
- [49] D. A. Dixon, J. Andzelm, G. Fitzgerald, E. Wimmer, and P. Jasien. *Benchmarking and Testing of the Local Density Functional Method for Molecular Systems*. Springer-Verlag, New York, 1991.
- [50] M. J. Frisch, G. W. Trucks, H. B. Schlegel, P. M. W. Gill, B. G. Johnson, M. W. Wong, J. B. Foresman, M. A. Robb, M. Head-Gordon, E. S. Repogle, R. Gomperts, J. L. Andres, K. Raghavachari, J. S. Binkley, C. Gonzales, P. L. Martin, D. J. Fox, D. J. DeFrees, J. Baker, J. J. P. Stewart, and J. A. Pople. Gaussian 92/dft, 1993. also see <http://www.gaussian.com>.
- [51] R. D. Amos and J. E. Rice. Implementation of analytic derivative methods in quantum chemistry. *Computer Physics Reports*, **10**:147–87, 1989.
- [52] CADPAC. <http://ket.ch.cam.ac.uk/software/cadpac.html>.
- [53] UniChem. <http://www.oxmol.com/prods/unichem/>.
- [54] P. Hohenberg and W. Kohn. *Phys. Rev. B*, **136**:864, 1964.
- [55] W. Kohn and L.J. Sham. *Phys. Rev. A*, **140**:1133, 1965.
- [56] A. Komornicki and G. Fitzgerald. Molecular gradients and Hessians implemented in density functional theory. *J. Chem. Phys.*, **98**:1398, 1993.
- [57] J. A. Pople, R. Krishnan, H. B. Schlegel, and J. S. Binkley. Derivative Studies in Hartree-Fock and Moller-Plesset Theories. *Int. J. Quantum Chem. Symp.*, **13**:225, 1979.

- [58] Dahlia K. Remler and Paul A. Madden. Molecular dynamics without effective potentials via the Car-Parrinello approach. *Mol. Phys.*, **70**:921–966, 1990.
- [59] James Wiggs and Hannes Jonsson. A hybrid decomposition parallel implementation of the Car-Parrinello method. *Computer Physics Communications*, **81**:1–18, 1994.
- [60] N. Troullier and Jose Luis Martins. Efficient pseudopotentials for plane-wave calculations. *Phys. Rev. B*, **43**:1993, 1991.
- [61] D. R. Hamann. Generalized norm-conserving pseudopotentials. *Phys. Rev. B*, **40**:2980, 1989.
- [62] Peter Comba. *Coordination Chemistry Review*, volume **123**, chapter The relation between ligand structures, coordination stereochemistry, and electronic and thermodynamic properties, pages 1–48. Elsevier Sequoia, 1993.
- [63] R. M. Badger. A relationship between internuclear distances and bond force constants. *J. Chem. Phys.*, **2**:128, 1934.
- [64] R. M. Badger. The relation between the internuclear distances and force constants of molecules and its applications to polyatomic molecules. *J. Chem. Phys.*, **3**:710, 1935.
- [65] *CRC Handbook of Chemistry and Physics, 78th edition*. CRC Press, Boca Raton New York, 1997-1998.
- [66] A. K. Rappe, C. J. Casewit, K. S. Colwell, W. A. Goddard III, and W. M. Skiff. UFF, a full periodic table force field for molecular mechanics and molecular dynamics simulations. *J. Am. Chem. Soc.*, **114**:10024, 1992.

- [67] Thomas H. Fischer, Wesley P. Petersen, and Hans Peter Luth. A new optimization technique for artificial neural networks applied to prediction of force constants of large molecules. *J. Comp. Chem.*, **16**:923, 1995.
- [68] M. O’Keeffe and N. E. Brese. Atom sizes and bond lengths in molecules and crystals. *J. Am. Chem. Soc.*, **113**:3226, 1991.
- [69] Michael J. S. Dewar, Eve G. Zoebisch, Eamonn F. Healy, and James J. P. Stewart. AM1: A new general purpose quantum mechanical molecular model. *J. Am. Chem. Soc.*, **107**:3902, 1985.
- [70] R. Haydock, V. Heine, and M. J. Kelly. Electronic structure based on the local atomic environment for tight-binding bands: II. *J. Phys.*, **C8**:2591, 1975.
- [71] W. H. Press, S. A. Teukolsky, W. T. Vetterling, and B. P. Flannery. *Numerical recipes in Fortran 77: the art of scientific computing*, volume 1. William H. Press, 1995.
- [72] G. Herzberg. *Molecular spectra and molecular structure. III. Electronic spectra and electronic structure of polyatomic molecules*. New York, Van Nostrand, 1966.
- [73] B. N. Figgis. *Introduction to ligand fields*. Interscience Publishers, 1966.
- [74] Britt Hedman and Graham George. private communication.
- [75] A. L. Ankoudinov. *Relativistic Spin-dependent X-ray Absorption Theory*. PhD thesis, University of Washington, 1996.
- [76] G. N. George, R. C. Prince, and S. P. Cramer. X-ray absorption spectroscopy of *Pyrococcus furiosus* rubredoxin. *Science*, **243**:789, 1989.

- [77] J. J. Rehr and R. C. Albers. Scattering-matrix formulation of curved-wave multiple-scattering theory: Application to x-ray-absorption fine structure. *Phys. Rev. B*, **41**:8139, 1990.

Appendix A

COMPUTER PROGRAMS SIGEM AND SIGRM

A.1 Program structure

Computer programs SIGEM and SIGRM calculate values of $\sigma_j^2(T)$ for SS and MS paths at a given temperature T using the EM method (Chap. 2) and RM (Chap. 3) accordingly. These programs are coded in FORTRAN 77 and implemented as FEFF subroutines parallel to the already existing SIGMS subroutine which calculates $\sigma_j^2(T)$ via the CD model. A new keyword, `idwopt`, was added to DEBYE card in the `feff.inp` file in order to incorporate these new options:

```
DEBYE    temp    thetad    [idwopt]
```

This keyword is optional in a sense that if `idwopt` is omitted, i.e. DEBYE card is in its old format, then the CD method will be used in the calculation. It allows one to choose a method for the DW factor calculations in the FEFF run: CD if `idwopt=0`, EM if `idwopt=1`, or RM if `idwopt=2`. Here `temp` is temperature T in degrees of Kelvin at which DW factors will be calculated and `thetad` is Debye temperature for the given material (these two keywords are exactly the same as in the old DEBYE card). If `idwopt` is negative or if DEBYE card is omitted, DW factors will not be calculated and all $\sigma_j^2(T)$'s will be set to 0. If `idwopt` is equal to 1 or 2, then an additional input file, `spring.inp`, containing force field description is *required*. Figure A.1 shows an example of the `feff.inp` file with the new DEBYE card.

The implementation scheme is following. If DEBYE card with `idwopt` equal to 1 or 2 is read, FEFF calls one of the subroutines, SIGEM or SIGRM, as specified by the keyword. Then SIGEM (SIGRM) calls subroutine DWRDIN which reads the list of

```

TITLE    13-atom model of zinc tetraimidazole
CONTROL  1 1 1 1 1 1
PRINT    5 0 0 0 0 0
DEBYE    300.  0.  2

POTENTIALS
* ipot   z  label
      0   30  Zn   3  3
      1    7   N   3  3
      2    6   C   3  3

ATOMS
      0.000000   0.000000   0.000000   0
      1.558800  -1.502400   2.056700   2
      1.400100  -1.165700   0.784400   1
      2.329100  -1.907500   0.076100   2
     -2.185200   1.371100   1.432900   2
     -0.889900   1.103100   1.387200   1
     -0.317600   1.778000   2.445200   2
     -1.558800  -1.502400  -2.056700   2
     -1.400100  -1.165700  -0.784400   1
     -2.329100  -1.907500  -0.076100   2
      2.185200   1.371100  -1.432900   2
      0.889900   1.103100  -1.387200   1
      0.317600   1.778000  -2.445200   2

END

```

Figure A.1: A sample feff.inp file for use in a FEFF SX run with EM option for DW factor calculation.

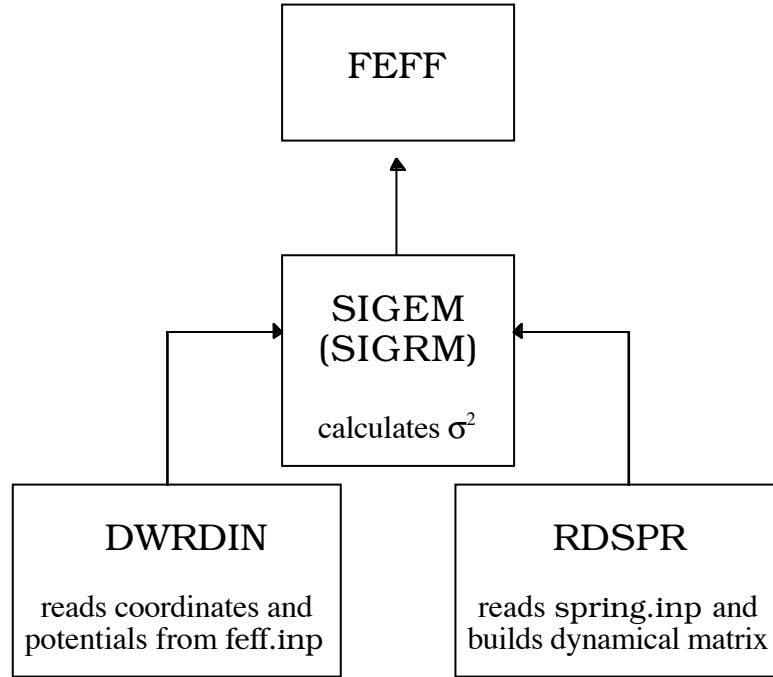


Figure A.2: Implementation scheme.

atomic coordinates and potentials from the `feff.inp` file. After that `RDSPR` reads the `spring.inp` file, searches for all similar bonds and angles, creates complete lists of all bond stretches and angle bends, and then, based on the force field and geometry of the structure, calculates cartesian force constant matrix as a sum of Φ^{str} (3.2) and Φ^{ang} (4.7) and scales it with atomic masses to have the dynamical matrix. It also uses another new subroutine `SANG` to calculate vectors \vec{s}_{ti} based on Eq. 4.4. The dynamical matrix is then passed to the corresponding main subroutine, i.e. `SIGEM` for the EM method or `SIGRM` for the RM, and saved there to be accessed for σ_j^2 calculation for each scattering path in the list.

A.2 *Input file* `spring.inp`

The new additional input file `spring.inp` for a `FEFF` run with the new DW factor options has to be created by the user. This file has the same user-friendly format

```

* 13-atom model of zinc tetraimidazole
*
*          res          wmax   dosfit   acut
VDOS      0.02      1       1.2      3
PRINT 5
STRETCHES
* i      j      k_ij      dR_ij (%)
  0      2      110.      2.
  1      2      626.      5.
ANGLES
* i      j      k      ktheta      dtheta (%)
  2      0      5      37.      10.
  1      2      3      2590.      10.

```

Figure A.3: A sample `spring.inp` file for 13-atom model of zinc tetraimidazole. The corresponding `feff.inp` is shown in Fig. A.1.

as the `feff.inp` file (e.g. the comment lines begin with an asterisk (*), empty lines are ignored, the order in which the cards are used is arbitrary, *etc.*). A sample `spring.inp` file is shown in Fig. A.3. Detailed description of the new cards used in the `spring.inp` file follows below.

VDOS `res` `wmax` `dosfit` [`acut`]

This card is needed only for the EM runs and is optional, i.e. if it is omitted, the default values are used. The keywords in the `VDOS` card define the integration parameters used in the `VDOS` calculation. Here `res` is the `VDOS` spectral resolution width (default `res` = 0.05, i.e. 5% of the bandwidth). The smaller this number the more fine structure is present in the spectrum and the longer the computation time. Finer resolution is usually helpful for mode analysis in small molecules. The next keyword, `wmax` is a multiplication factor used to increase (decrease) the maximum frequency to which `VDOS` is calculated by `wmax` times (default `wmax`=1). Keyword

`dosfit` is a real positive number governing how much of the low frequency part of the VDOS is to be fitted to Debye like behavior, $A \cdot \omega^2$. If it is equal to 0 then no fitting will be applied. The higher the number the more of VDOS will be fitted. The default value is `dosfit = 1` (about 10% of the total width). This parameter is useful for elimination of low frequency “noise” and zero-frequency modes. Finally, `acut` is the time integration cutoff parameter. It rarely needs to be changed (usually in cases of very small open molecular structures). The higher this number the longer the computation time. The `acut` keyword is optional and if omitted the default value, `acut=3`, is used. The entire VDOS card is ignored by `sigrm`.

```
*           res      wmax  dosfit
VDOS       0.02      1     1.2
```

PRINT [iprdos]

The use of the PRINT card is different in SIGEM and SIGRM runs. If DW factors are calculated using the EM method and this card is present, then `prdenNNNN.dat` files containing projected VDOS for selected number of scattering paths will be printed out. Here `iprdos` is the number of paths from the paths list for which (and only which) these files will be written. If `iprdos=0` or if the PRINT card is omitted, no VDOS files will be printed out. If `iprdos=n`, there will be n `prdenNNNN.dat` files created for the first n paths in the list.

If DW factors are calculated using the RM and the PRINT card is present then the file `s2_rm1.dat` containing first tier results will be printed out. The keyword `iprdos` is ignored in this case.

```
PRINT 5
```

STRETCHES

```
i   j   k_ij   dR_ij
```


This card is *absolutely required* for both, the EM and RM, runs and is followed by the list of bond stretching force constants to be used in the calculation. Here i and j are atomic indices (just like in the `geom.dat` file, e.g. the absorbing atom has index 0), and `k_ij` is a single central force constant characterizing the interaction between atoms i and j in units of $10^2 \times \text{mdyn}/\text{\AA}$, or N/m. One should include as many distinct bonds in the list as possible and then the code will search for the similar ones and assign to them the same force constants. The last parameter in the row, `dR_ij`, is tolerance in the bond length when searching for similar bonds and is measured in percentage points. For example, if `dR_ij=5` then all bonds between two atoms with the same potentials as i and j and with the bond length being within 5% of R_{ij} will be assigned the same stretching force constant `k_ij`.

STRETCHES

* i	j	k_ij	dR_ij (%)
0	2	110.	2.
1	2	626.	5.

ANGLES

i	j	k	ktheta	dtheta
---	---	---	--------	--------

This card is similar to the `STRETCHES` but is optional in most cases and allows one to include θ_{ijk} angle bending force constants, k_{θ}^{ijk} , in the calculation. The force constants are in units of $10^2 \times \text{mdyn}\text{\AA}/\text{rad}^2$. Here `dtheta` is tolerance in the angle value when searching for similar angles. Sometimes it is useful to include this card in order to avoid zero-frequency modes.

ANGLES

* i	j	k	ktheta	dtheta (%)
2	0	5	37.	10.
1	2	3	2590.	10.

A.3 Output files

All σ_j^2 values in the output files are given in units of \AA^2 , all frequencies are in units of THz, and all reduced masses are in atomic units.

The output files from a SIGEM calculation include

- `s2_em.dat` which contains σ_j^2 for each scattering path in `paths.dat` (see Fig. A.5c and Fig. A.7c). Here `N_at` is the number of atoms in the cluster for which σ_j^2 's are calculated, `ipath` is the current scattering path index, `nleg` is the number of the scattering legs in the path, `sig2` is the corresponding value of σ_j^2 , `mu_ipath` is projected reduced mass for the path (Eq. 2.11), and `check0` is equal to a percentage error in the VDOS normalization to 1 and is a rough indicator of how “good” the VDOS is (if this number is above 10% then there might be something wrong with the spectrum, e.g. part of the spectrum is being cut off at high frequencies because the ω_{max} value is too low; it will also be large if a zero-frequency mode was eliminated by `dosfit`).
- `prdenNNNN.dat` which contains projected VDOS for selected scattering paths (as indicated by the **PRINT** card).

The SIGRM calculation produces the following output files.

- `s2_rm2.dat` which contains values of σ_j^2 calculated via the RM using the second tier approximation for each scattering path in `paths.dat` (see Fig. A.5b and Fig. A.5b). Here `w1` and `w2` are the second tier frequencies, and `A1` and `A2` are the corresponding weight factors (see Sec. 3.1). The rest of the parameters are the same as in `s2_em.dat`.
- `s2_rm1.dat` which contains values of σ_j^2 calculated via the RM using the first tier approximation (see Fig. A.5a and Fig. A.5a). Here `we` = $a_0^{1/2} = \langle Q_j | D | Q_j \rangle$ is the first tier frequency (see Sec. 3.1).

A.4 Local variables, their dimensions, and descriptions

In this section we present information which is of limited value to regular users but could be useful to someone who would like to modify the code.

There are five variables which are passed to the subroutines SIGEM and SIGRM through the argument list. These include temperature `tk`, index of the current path `ipath`, maximum number of the scattering legs `nlegx`, number of the scattering legs in the current path `nleg`, and coordinates of atoms involved in the current scattering path `rat`. All frequency variables used within the codes are in units of `w0` which is equal to a square root of the second moment of the dynamical matrix for a bond between the absorber and its first nearest neighbor with which it has a non-zero central interaction (i.e. natural frequency of the first nearest neighbor bond). All time variables are in units of $1/w0$.

Parameters used to dimension local arrays consist of maximum number of atoms in the cluster `natxdw` (it is typically equal to 200), maximum number of scattering legs in a path `nlegx` (passed through the argument list), and maximum number of the frequency grid points `nwx` (set to 700).

Primary local arrays used in the codes include

- arrays used in both subroutines, SIGEM and SIGRM:

<code>rat1(3,natxdw)</code>	cartesian coordinates of all atoms in the cluster
<code>iz(natxdw)</code>	atomic numbers of all atoms in the cluster
<code>dm(3,3,natxdw,natxdw)</code>	matrix elements $D_{\alpha,\beta}(l,m)$ of the cartesian dynamical matrix
<code>rnn(3,natxdw,natxdw)</code>	cartesian components R_{lm}^α of the directing unit vectors between atoms l and m
<code>nnl(natxdw,natxdw)</code>	list of atoms for which tensor $D(l,m)$ has non-zero elements (used to avoid summation of 0's)

<code>rat(3,0:nlegx)</code>	coordinates of atoms in the current scattering path j
<code>nconv(0:nlegx)</code>	converts the index of the atom in the path to its index in the list of all atoms in the cluster
<code>q0(3,natxdw)</code>	initial state vector $ 0\rangle = Q_j\rangle$

- arrays used only in the subroutine SIGEM:

<code>gr(nwx)</code>	VDOS $\rho_j(\omega)$
<code>w(nwx)</code>	frequency grid from 0 to ω_{max}
<code>uu(3,natxdw)</code>	displacement state $ Q_j(t)\rangle$
<code>up(3,natxdw)</code>	displacement state $ Q_j(t - \Delta t)\rangle$
<code>ff(3,natxdw)</code>	acceleration $d^2 Q_j(t)\rangle/d^2t$

- arrays used only in the subroutine SIGRM:

<code>q1(3,natxdw)</code>	state vector $ 1\rangle = D Q\rangle$
<code>nq1(natxdw)</code>	list of atoms involved in $ 1\rangle$

A.5 Example input and output files

Example input file for a 177-atom cluster of Cu crystal is shown in Fig. A.4. Here only a single central force constant between the first nearest neighbors was taken into account (Sec. 2.5.1). The corresponding output files from the SIGRM and SIGEM runs for several scattering paths are presented in Fig. A.5. Similar input files can be constructed for other fcc structures, e.g. Pt, Al, *etc.*

Figure A.6 shows example input file for a 147-atom cluster of c-Ge crystal. The force constants used here were fitted to the phonon dispersion curves [38]. The corresponding output files are presented in Fig. A.7. Similar input files can be constructed for other diamond-type lattices, e.g. Si, C, *etc.*

```
*          res    wmax  dosfit  acut
VDOS      0.03   0.5    1
PRINT 3
STRETCHES
* i        j      k_ij    dR_ij (%)
  0        1      27.9    2.
```

Figure A.4: Sample `spring.inp` file for Cu crystal.

a) Cu metal fcc a=3.61

temperature = 300.00 N_at = 177

```
-----
ipath  nleg    sig2    mu_ipath    w_e
  1      2    0.00635    31.775     36.36
  2      2    0.00784    31.775     32.52
  3      3    0.00654    28.244     38.13
  4      3    0.00732    28.793     35.53
```

b) Cu metal fcc a=3.61

temperature = 300.00 N_at = 177

```
-----
ipath  nleg    sig2    mu_ipath    w_1    w_2    A1    A2
  1      2    0.00745    31.775     41.89    27.51    0.566  0.434
  2      2    0.00996    31.775     40.70    24.31    0.438  0.562
  3      3    0.00737    28.244     42.24    28.93    0.651  0.349
  4      3    0.00898    28.793     41.52    25.77    0.564  0.436
```

c) Cu metal fcc a=3.61

temperature = 300.00 N_at = 177

```
-----
ipath  nleg    sig2    mu_ipath    check0(%)
  1      2    0.00821    31.775     0.20
  2      2    0.01208    31.775     0.23
  3      3    0.00787    28.244     0.24
  4      3    0.01038    28.793     0.24
```

Figure A.5: Sample output files for Cu crystal at 300 K: a) s2_rm1.dat, b) s2_rm2.dat, and c) s2_em.dat.

```
*          res   wmax  dosfit  acut
VDOS      0.02   0.7    0.     3.
PRINT 6
STRETCHES
* i        j        k_ij      dR_ij (%)
  0        1        103.58     2.
  0        5         5.81      2.
  0       20        -1.08      2.
  0       30        -0.30      2.
ANGLES
* i        j        k        ktheta    dtheta (%)
  1        0        2         31.45     2.
```

Figure A.6: Sample `spring.inp` file for for Ge crystal.

a) Ge diamond structure

temperature = 300.00 N_at = 147

```
-----
ipath  nleg   sig2   mu_ipath  w_e
  1     2   0.00304  36.295   50.62
  2     2   0.00426  36.295   42.02
  3     3   0.00377  33.765   46.73
  4     3   0.00377  33.765   46.73
```

b) Ge diamond structure

temperature = 300.00 N_at = 147

```
-----
ipath  nleg   sig2   mu_ipath  w_1   w_2   A1   A2
  1     2   0.00324  36.295   52.79  36.77  0.844  0.156
  2     2   0.00593  36.295   50.43  27.09  0.571  0.429
  3     3   0.00450  33.765   51.69  31.72  0.707  0.293
  4     3   0.00452  33.765   51.58  31.26  0.717  0.283
```

c) Ge diamond structure

temperature = 300.00 N_at = 147

```
-----
ipath  nleg   sig2   mu_ipath  check0(%)
  1     2   0.00340  36.295   0.67
  2     2   0.00911  36.295   0.49
  3     3   0.00538  33.765   0.55
  4     3   0.00626  33.765   0.55
```

Figure A.7: Sample output files for Ge crystal at 300 K: a) s2_rm1.dat, b) s2_rm2.dat, and c) s2_em.dat.

Appendix B

TABLE OF SELECTED PARAMETERS USED IN THE UFF MODEL

(see text in Section 2.4 for details)

Atom types in Table B.1 have the following notation. The first two characters correspond to the chemical symbol (an underscore is used in place of the second character if the atomic symbol consists of only one letter, e.g. I_ is iodine, Cl is chlorine). The third character denotes hybridization (geometry): 1=linear, 2=trigonal, R=resonant, 3=tetrahedral, 4=square planar, 5=trigonal bipyramidal, 6=octahedral. The fourth and fifth characters indicate formal oxidation state (e.g. Rh6+3 is an octahedral rhodium formally in the +3 oxidation state as in $\text{Rh}(\text{NH}_3)_6^{3+}$ and other alternate parameters (e.g. H_b corresponds to a bridging hydrogen as in B_2H_6 , O_3_z is an oxygen suited for framework oxygens of a zeolite lattice, P_3_q is a tetrahedral four-coordinate phosphorus used to describe organometallic coordinated phosphines as in $(\text{Ph}_3\text{P})_2\text{PtCl}_2$). All parameters and notations in the table are taken from the original paper by Rappe *et al.* [66].

Table B.1: Values of selected UFF model parameters for different atoms.

atom type	r_i (Å)	θ_0 (rad)	Z_i^*
H	0.354	180.0	0.712
H_b	0.460	83.5	0.712
<i>continued on next page</i>			

<i>continued from previous page</i>			
atom type	r_i (Å)	θ_0 (rad)	Z_i^*
He4 + 4	0.849	90.0	0.098
Li	1.336	180.0	1.026
Be3 + 2	1.074	109.47	1.565
B_3	0.838	109.47	1.755
B_2	0.828	120.0	1.755
C_3	0.757	109.47	1.912
C_R	0.729	120.0	1.912
C_2	0.732	120.0	1.912
C_1	0.706	180.0	1.912
N_3	0.700	106.7	2.544
N_R	0.699	120.0	2.544
N_2	0.685	111.2	2.544
N_1	0.656	180.0	2.544
O_3	0.658	104.51	2.300
O_3_z	0.528	146.0	2.300
O_R	0.680	110.0	2.300
O_2	0.634	120.0	2.300
O_1	0.639	180.0	2.300
F_	0.668	180.0	1.735
Ne4 + 4	0.920	90.0	0.194
Na	1.539	180.0	1.081
Mg3 + 2	1.421	109.47	1.787
Al3	1.244	109.47	1.792
<i>continued on next page</i>			

<i>continued from previous page</i>			
atom type	r_i (Å)	θ_0 (rad)	Z_i^*
Si3	1.117	109.47	2.323
P_3 + 3	1.101	93.8	2.863
P_3 + 5	1.056	109.47	2.863
P_3 + q	1.056	109.47	2.863
S_3 + 2	1.064	92.1	2.703
S_3 + 4	1.049	103.20	2.703
S_3 + 6	1.027	109.47	2.703
S_R	1.077	92.2	2.703
S_2	0.854	120.0	2.703
Cl	1.044	180.0	2.348
Ar4 + 4	1.032	90.0	0.300
K_	1.953	180.0	1.165
Ca6 + 2	1.761	90.0	2.141
Sc3 + 3	1.513	109.47	2.592
Ti3 + 4	1.412	109.47	2.659
Ti6 + 4	1.412	90.0	2.659
V_3 + 5	1.402	109.47	2.679
Cr6 + 3	1.345	90.0	2.463
Mn6 + 2	1.382	90.0	2.43
Fe3 + 2	1.270	109.47	2.43
Fe6 + 2	1.335	90.0	2.43
Co6 + 3	1.241	90.0	2.43
Ni4 + 2	1.164	90.0	2.43
<i>continued on next page</i>			

<i>continued from previous page</i>			
atom type	r_i (Å)	θ_0 (rad)	Z_i^*
Cu3 + 1	1.302	109.47	1.756
Zn3 + 2	1.193	109.47	1.308
Ga3 + 3	1.260	109.47	1.821
Ge3	1.197	109.47	2.789
As3 + 3	1.211	92.1	2.864
Se3 + 2	1.190	90.6	2.764
Br	1.192	180.0	2.519
Kr4 + 4	1.147	90.0	0.452
Rb	2.260	180.0	1.592
Sr6 + 2	2.052	90.0	2.449
Y ₃ + 3	1.698	109.47	3.257
Zr3 + 4	1.564	109.47	3.667
Nb3 + 5	1.473	109.47	3.618
Mo6 + 6	1.467	90.0	3.40
Mo3 + 6	1.484	109.47	3.40
Tc6 + 5	1.322	90.0	3.40
Ru6 + 2	1.478	90.0	3.40
Rh6 + 3	1.332	90.0	3.508
Pd4 + 2	1.338	90.0	3.21
Ag1 + 1	1.386	180.0	1.956
Cd3 + 2	1.403	109.47	1.65
In3 + 3	1.459	109.47	2.07
Sn3	1.398	109.47	2.961
<i>continued on next page</i>			

<i>continued from previous page</i>			
atom type	r_i (Å)	θ_0 (rad)	Z_i^*
Sb3 + 3	1.407	91.6	2.704
Te3 + 2	1.386	90.25	2.882
I ₋	1.382	180.0	2.65
Xe4 + 4	1.267	90.0	0.556
Cs	2.570	180.0	1.573
Ba6 + 2	2.277	90.0	2.727
La3 + 3	1.943	109.47	3.30
Ce6 + 3	1.841	90.0	3.30
Pr6 + 3	1.823	90.0	3.30
Nd6 + 3	1.816	90.0	3.30
Pm6 + 3	1.801	90.0	3.30
Sm6 + 3	1.780	90.0	3.30
Eu6 + 3	1.771	90.0	3.30
Gd6 + 3	1.735	90.0	3.30
Tb6 + 3	1.732	90.0	3.30
Dy6 + 3	1.710	90.0	3.30
Ho6 + 3	1.696	90.0	3.416
Er6 + 3	1.673	90.0	3.30
Tm6 + 3	1.660	90.0	3.30
Yb6 + 3	1.637	90.0	2.618
Lu6 + 3	1.671	90.0	3.271
Hf3 + 4	1.611	109.47	3.921
Ta3 + 5	1.511	109.47	4.075
<i>continued on next page</i>			

<i>continued from previous page</i>			
atom type	r_i (Å)	θ_0 (rad)	Z_i^*
W_6 + 6	1.392	90.0	3.70
W_3 + 4	1.526	109.47	3.70
W_3 + 6	1.380	109.47	3.70
Re6 + 5	1.372	90.0	3.70
Re3 + 7	1.314	109.47	3.70
Os6 + 6	1.372	90.0	3.70
Ir6 + 3	1.371	90.0	3.731
Pt4 + 2	1.364	90.0	3.382
Au4 + 3	1.262	90.0	2.625
Hg1 + 2	1.340	180.0	1.75
Tl3 + 3	1.518	120.0	2.068
Pb3	1.459	109.47	2.846
Bi3 + 3	1.512	90.0	2.470
Po3 + 2	1.50	90.0	2.33
At	1.545	180.0	2.24
Rn4 + 4	1.420	90.0	0.583
Fr	2.880	180.0	1.847
Ra6 + 2	2.512	90.0	2.92
Ac6 + 3	1.983	90.0	3.90
Th6 + 4	1.721	90.0	4.202
Pa6 + 4	1.711	90.0	3.90
U_6 + 4	1.684	90.0	3.90
Np6 + 4	1.666	90.0	3.90
<i>continued on next page</i>			

<i>continued from previous page</i>			
atom type	r_i (Å)	θ_0 (rad)	Z_i^*
Pu6 + 4	1.657	90.0	3.90
Am6 + 4	1.660	90.0	3.90
Cm6 + 3	1.801	90.0	3.90
Bk6 + 3	1.761	90.0	3.90
Cf6 + 3	1.750	90.0	3.90
Es6 + 3	1.724	90.0	3.90
Fm6 + 3	1.712	90.0	3.90
Md6 + 3	1.689	90.0	3.90
No6 + 3	1.679	90.0	3.90
Lw6 + 3	1.698	90.0	3.90

For more details on these parameters see the original paper [66].

VITA

Anna Poiarkova was born in 1972 in Kiev, Ukraine. After graduating in 1989 from Kiev High School #145 with advanced study of physics and mathematics, she entered undergraduate program in Physics at Kiev State University (KSU). Anna graduated with honors from KSU in 1994 and in the same year started her graduate study at the Department of Physics, University of Washington where she received a MS in Physics in 1996. This dissertation completes the requirements for her Ph.D. in Physics.